N° d'ordre :

REPUBLIQUE ALGERIENNE DEMOCRATIQUE & POPULAIRE

MINISTERE DE L'ENSEIGNEMENT SUPERIEUR & DE LA RECHERCHE SCIENTIFIQUE

UNIVERSITE DJILLALI LIABES
FACULTE DES SCIENCES EXACTES
SIDI BEL ABBES

Thèse de Doctorat de 3ème cycle

Présentée par

Mr BOUROUROU Yahia

Spécialité: Physique

Option: Modélisation et Simulation Numérique

Intitulé

Étude *ab-initio* de la structure électronique et magnétique des composés à base d'azote

Soutenu le 10/11/2016
Devant le jury composé de :

Président :	*AMERI Mohammed*	*Professeur, U. SBA*
Examinateurs:	*BENTATA Samir*	*Professeur, U. Mostaganem*
	FERHAT Mohammed	*Professeur, USTO*
	SEBANE Mokhtar	*Professeur, U. SBA*
	ABBAR Boucif	*Professeur, U. SBA*
Encadreur :	*BOUHAFS Bachir*	*Professeur, U. SBA*

Année universitaire 2016-2017

Ab-initio study of electronic and magnetic structure of nitrogen-based compounds

ACKNOWLEDGEMENTS

First of all, I would like to express my gratitude to Allah for providing me the blessings to complete this work. This thesis would not have been created without help and support of several people, to whom I am very grateful. A big thanks to my supervisor and the head of our laboratory Prof. Bachir BOUHAFS for accepting me into his group, for his supervision and constant support, for giving me intellectual freedom in my work, supporting my attendance at various conferences and demanding a high quality of work in all my endeavors.

I would like also to thank the members of my doctoral examination committee: Prof. Mohammed AMERI (University of Sidi Bel-Abbes) as president, to Prof. Samir BENTATA (University of Mostaganem), Prof. Mohammed FERHAT (University of USTO), Prof. Mokhtar SEBANE (University of Sidi Bel-Abbes), and Prof. Boucif ABBAR (University of Sidi Bel-Abbes) as examinations, who agreed to answer the call even of their obligations and whose valuable comments will help improve this thesis.

I would like to acknowledge all memebers of laboratory of modelling and simulation in materials science who helped me and gave me encouraging words. A special thanks goes to H. BENAISSA, R. Zine El-Kelma, A. LAKEHAL, M. AZZOUZ, M. DJERMOUNI, R. MEBSOUT, S. AMARI, L. SEDDIK, K. DINE, A. DJEFAL, S. BELHACHI, I. D. YAHIAOUI, Y. ZIDI, and also my frind H. MAIZ from laboratory of materials physics and fluids (Univ. USTO), and others which I have learned so much from all of them, espichally how to handle the complicated and confusing world of computational physics. I extend my thanks to all members of laboratory of materials science (Univ. of Laghouat), who always believed in me and never hesitate to provide relentless support and motivation at all times.

Finaly my deepest gratitude goes to my parents for their absolute support in life and studies, my brother and sisters, my beloved wife, my family members, and also to my friends who supported me during my research project. To those who indirectly contributed in this research, your kindness means a lot to me. Thank you very much.

ABSTRACT

In the framework of density functional theory (DFT), spin-polarization and pressure effects on the structural, magnetic and electronic properties of the 3*d* transition-metal mono- and semi-borides TM-B and TM_2B (TM=Mn, Fe, Co), respectively, have been studied using the full-potential Linearized augmented plane-wave method (FP-LAPW) with both local density approximation (LDA) and generalized gradient approximation (GGA). We have studied also the structural, magnetic and electronic properties of the transition metal mono-nitrides TMN (TM=Mn, Fe, and Co). We have showed the effects of electron correlation on the structural, magnetic and electronic properties for both RS-FeN and ZB-FeN phases using GGA +*U*. The calculated lattice constants, bulk modulus, pressure derivative and magnetic moment for all the compounds studied were found to be in very good agreement with other works. It has been found that the spin polarization and pressure have a significant impact on the cell volume, bulk modulus and magnetic moment for MnB, FeB, Fe_2B and Co_2B ferromagnetic compounds. Finally, we remarked that the electron correlation plays crucially important role in determining the structural and magnetic stability and different properties for FeN compound.

Key-words: The density functional theory; Magnetic moment; Electronic structure; Ferromagnetism; Local density approximation (LDA); Generalized gradient approximation (GGA).

RESUME

Dans le cadre de la théorie de la fonctionnelle de la densité (DFT), les effets de la polarisation magnétique et de la pression sur les propriétés structurales, magnétiques et électroniques des mono- et semi-borures à base des métaux de transitions, TM-B et TM_2B (TM = Mn, Fe, Co), respectivement, ont été étudiés en utilisant la méthode des ondes planes augmentées linéarisées (FP-LAPW) avec l'approximation de la densité locale (LDA) et l'approximation du gradient généralisé (GGA). Nous avons aussi étudié les propriétés structurales, magnétiques et électroniques des mono-nitrures à base des métaux de transitions TM-N (TM = Mn, Fe et Co). Nous avons analysé les effets de corrélation électronique sur les propriétés structurales, magnétiques et électroniques pour les deux phases NaCl et zinc-blende du FeN en utilisant GGA+U. Les paramètres du réseau, le module de compressibilité, sa dérivée, et le moment magnétique pour tous les composés étudiés ont été trouvés en très bon accord avec d'autres travaux. Nous avons constaté que la polarisation magnétique et la pression ont un effet significatif sur le volume de la cellule, le module de compressibilité et le moment magnétique pour les composés ferromagnétiques MnB, FeB, Fe_2B et Co_2B. Enfin, nous avons aussi remarqué que la corrélation électronique joue un rôle important dans la stabilité structurale et magnétique et dans les différentes propriétés du composé FeN.

Mots-clés : La théorie de la fonctionnelle de la densité; Moment magnétique; Structure électronique; Ferromagnétisme; l'approximation de la densité locale (LDA); l'approximation du gradient généraliser (GGA).

ملخص

بالاعتماد على نظرية الكثافة الدالية (DFT)، قمنا بدراسة تأثير العزم المغناطيسي والضغط على الخصائص البنيوية، المغناطسية والإلكترونية على بعض المعادن الانتقالية (TM = Mn, Fe, Co) TM-B, TM_2B وهذا باستعمال طريقة الأمواج المستوية المتزايدة خطيا (FP-LAPW) مع كل من تقريب الكثافة الموضعية (LDA) وتقريب التدرج المعمم (GGA). قمنا أيضا بدراسة الخصائص البنيوية، المغناطسية والإلكترونية للمعادن التالية (TM=Mn, Fe, Co) TM-N باستعمال GGA +*U* وقمنا بعرض تأثير ارتباط الالكترون على الخصائص البنيوية، المغناطيسية والالكترونية في كل من البنيتينكلوريد الصديوم (NaCl) وكبريتيد الزنك (zinc-blende). قيم كل من ثابت الشبكة، ومعامل الانضغاط، والمشتقة الأولى لمعامل الانضغاط والعزم المغناطيسي لكل المركبات المدروسة تتوافق جيدا مع الأعمال الأخرى. من خلال هذه الدراسة تبين أن العزم المغناطيسي والضغط لهما تأثير كبير على حجم الخلية ومعامل الانضغاط والعزم المغناطسي في كل المركبات الفيرومغناطيسية MnB, FeB, Fe_2B Co_2B. وأخيرا لاحظنا أن ارتباط الالكترون يلعب دور مهما في تحديد الاستقرار البنيوي والمغناطيسي ومختلف الخصائص الإلكترونية بالنسبة لمركب FeN.

الكلمات المفتاحية: نظرية الكثافة الدالية، العزم المغناطيسي، البنية الإلكترونية، فيرومغناطيسية، تقريب الكثافة الموضعية (LDA)، تقريب التدرج المعمم (GGA).

TABLE OF CONTENTS

LIST OF FIGURES

LIST OF TABLES

Chapter I

1. Introduction

1.1 General context and objective

Materials are so important in the development of civilization and human life on the earth. Many experimental techniques have been developed to measure and discover news properties of materials such as X-rays [1], infrared spectroscopy [2] and inelastic neutron scattering [3]. On the other hand, understanding of how materials behave like they do, and why they differ in properties was only possible with the electronic states understanding allowed by quantum mechanics. Electronic states of materials is fundamental to understand their macroscopic properties, such as thermal, electrical conductivity, structure etc. People use a variety of quantum methods to predict these electronic states and hence material properties at the most fundamental level.

Quantum methods allow us to study transition states and unusual structures and conformations which are difficult, if not impossible, to study experimentally. Ab initio methods are based entirely on quantum mechanics and basic physical constants. Other methods are called empirical or semi-empirical because they employ additional empirical parameters. Density functional theory (DFT) is among the most popular and versatile Ab initio methods available in condensed-matter physics. DFT was put on a firm theoretical footing by the two Hohenberg–Kohn theorems [4]. The full potential linearized augmented plane wave (FPLAPW) method [5] is among the most accurate methods for performing electronic structure calculations for crystals. It is based on the DFT for the treatment of exchange and correlation energy and uses both the local spin density approximation (LSDA) [6] and the generalized gradient approximation (GGA) [7, 8].

Transition metal borides and nitrides have a large outstanding physical properties. The combination of metals with light covalent-bond forming atoms like B and N often leads to materials which not only have a high melting point, but also have a very low compressibility and high hardness compared with the pure metal [9]. In addition, transition metal borides and nitrides possess other properties, such as good electrical-thermal conductivity, catalytic activity, and magnetic properties [10-14]. They are widely used for cutting tools and hard coatings [15, 16].

In recent decades, interest in borides increased and many useful applications have been found in nanomaterial science. Nanosize cobalt boride particles were prepared by a liquid chemical reaction, reduction of the cobalt (2-ethyl-hexyl) sulfosuccinate by sodium borohyride either in reverse micelles or in a diphase system [17]. Manganese mono-boride is important due to potential spintronic applications [18]. The reported experimental magnetic moments give values of 1.83μ_B for MnB, 1.12 μ_B for FeB, and 0 μ_B for CoB [19].

It is usually believed that the half-metallicity can only exist in more complex structures. Theoretical calculations showed that VN, CrN, MnN, FeN and CoN mono-nitrides become half-metallic under lattice expansion in the zinc-blend structure [20]. Transition metal mono-nitrides (MNs) of the 3*d* states have not been studied so extensively [21-26]. This can, However, be easily traced back to the much more challenging techniques required to prepare nitride phases [27]. Thin films of MnN have been synthesized in the face centered tetragonal NaCl-type structure with anti-ferromagnetic behavior [28]. These results have been confirmed later by neutronic diffraction [29]. Thin films of FeN have been synthesized and two possible crystal structures were reported [30-33]. One is the rocksalt (RS) structure with a lattice constant of a=4.57 Å, and by performing 57Fe Mössbauer spectroscopy measurements, the authors suggested rocksalt FeN to be an antiferromagnet [30, 31]. The other structure is of a zinc-blend (ZB)-type with a lattice constant of a=4.33 Å and a micromagnetic character [32]. Some discussions in the earlier literature about the

crystal structure of CoN, both ZB and RS structures have been reported depending on the synthesis method. Schmidt-Dumont and Kron [34] obtained rocksalt CoN with a lattice constant of 4.27 Å by decomposition of $Co(NH_2)_3$, while Taylor et al. [35] obtained zinc-blende CoN with a lattice constant of 4.28 Å by decomposing $[Co(NH_3)_6](N_3)_3$.

The spin polarization and pressure effects on the structural, magnetic and electronic properties of the transition metal mono- and semi-borides TMB and TM_2B (TM= Mn, Fe and Co) have been studied using both LSDA and GGA. Although, we have calculated the structural, magnetic and electronic properties of the transition metal mono-nitrides TMN (TM=Mn, Fe, and Co) using LSDA and GGA. Finally, we have shown the effects of electron correlation on structural, magnetic and electronic properties for both RS-FeN and ZB-FeN phases.

In order to show the effects of spin-polarization and pressure on the structural, electronic, and magnetic properties we have investigated the structural, electronic, and magnetic properties in the non-spin-polarization, spin-polarization and under pressure within LSDA and GGA for the transition metal mono- and semi-borides (TM- and TM_2-B which TM= Mn, Fe, Co). For FeN compound, the effects of electron correlation have been shown using GGA +*U* calculations. All calculations were performed using the full- potential linearized augmented plane wave (FP-LAPW) method which is implemented in the Wien2K calculations code [36]. The results are compared with experimental and other theoretical results.

1.2 Organization of this Thesis

This thesis is divided into five Chapters. Following this introductory part (chapter I) is Chapter II, which is dedicated to present the basic concepts of density functional theory (DFT) and introduce one of the most accurate methods, (L)APW+lo. Chapter III shows the different magnetic behaviors and the two basic theories of magnetism in materials, localized moments theory and itinerant electron theory. Chapters IV discusses and shows the results of our calculations for

monoborides, semiborides and mononitrides, respectively. Chapter V is summary of our thesis, including conclusions that we have drawn from our research.

Chapter II

2. Density functional theory and (L)APW + lo method

2.1 Ab initio methods

The term ab initio means from first principles. It does not mean that we are solving the Schrödinger equation exactly. It means that we are selecting a method that in principle with no inclusion of experimental data can lead to a reasonable approximation to the solution of the Schrödinger equation and then selecting a basis set that will implement that method in a reasonable way [37]. Ab initio electronic structure methods have the advantage that they can be made to converge to the exact solution, when all approximations are sufficiently small in magnitude and when the finite set of basis functions tends toward the limit of a complete set. In this case, using density functional theory within Born–Oppenheimer approximation to find the non-relativistic solution of the electronic Schrödinger equation (Eq. 2.1).

$$\hat{\mathrm{H}}\psi = E\psi \qquad (2.1)$$

Where ψ is an N-body wavefunction, E denotes the energy of either the ground or an excited state of the system. H is the Hamiltonian, the total energy operator for a system, and is written as the sum of the kinetic energy of all the components of the system and the internal potential energy. Thus for the kinetic and potential energy in a system of M nuclei and N electrons (atomic unit):

$$\hat{T}_N = -\sum_{\mathrm{A}}^{\mathrm{M}} \frac{1}{2\mathrm{M}_{\mathrm{A}}} \nabla_{\mathrm{A}}^2 \qquad (2.2)$$

$$\hat{\mathrm{T}}_{\mathrm{e}} = -\sum_{i}^{N} \frac{1}{2} \nabla_i^2 \qquad (2.3)$$

$$\hat{\mathrm{V}}_{\mathrm{NN}} = \sum_{A>B}^{M} \frac{Z_A Z_B}{r_{AB}} \qquad (2.4)$$

$$\hat{V}_{ee} = \sum_{i>j}^{N} \frac{1}{r_{ij}} \qquad (2.5)$$

$$\hat{V}_{eN} = -\sum_{A}^{M}\sum_{i}^{N} \frac{Z_A}{r_{iA}} \qquad (2.6)$$

Since, $\hat{H} = \hat{T} + \hat{V}$

$$\hat{H} = -\sum_{i}^{N} \frac{1}{2}\nabla_i^2 - \sum_{A}^{M}\sum_{i}^{N} \frac{Z_A}{r_{iA}} + \sum_{i>j}^{N} \frac{1}{r_{ij}} - \sum_{A}^{M} \frac{1}{2M_A}\nabla_A^2 + \sum_{A>B}^{M} \frac{Z_A Z_B}{r_{AB}} \qquad (2.7)$$

A common and very reasonable approximation used in the solution of Eq. 2.1 is the Born-Oppenheimer Approximation (BOA), Since the nuclei are much heavier than electrons (the mass of a proton is about 1836 times the mass of an electron), the nuclei move much slower (about two order of magnitude slower) than the electrons. Therefore we can separate the movement of nuclei and electrons. The last two terms can be removed from the total Hamiltonian to give the electronic Hamiltonian, $\hat{H}_e$, since $\hat{V}_{NN} = K$, and $\nabla_A^2 = 0$.

$$\hat{H}_e = -\sum_{i}^{N} \frac{1}{2}\nabla_i^2 - \sum_{A}^{M}\sum_{i}^{N} \frac{Z_A}{r_{iA}} + \sum_{i>j}^{N} \frac{1}{r_{ij}} \qquad (2.8)$$

The success of the BO approximation is due to the high ratio between nuclear and electronic masses, which we can separate the movement of electrons and nuclei. Now we can consider that the electrons are moving in a static external potential $V_{ext}(\mathbf{r})$ formed by the nuclei. The approximation is an important tool of quantum chemistry, even in the cases where the BO approximation breaks down, it is used as a point of departure for the computations for a wide range of ab initio methods, such as Hartree-Fock (HF), post-HF approaches and Density-functional theory (DFT), but we will restrict ourselves to the Density-functional theory, which our calculation based on.

2.2 Density Functional Theory

Density functional theory (DFT) is a poweful, formally exact theory [38, 39]. Widely used method in condensed-matter physics, computational physics and quantum chemistry to describe properties of condensed matter systems, which include not only standard bulk materials but also complex materials such as molecules, proteins, interfaces and nanoparticles. The principal feature of density functional method is that the many problem is solved directly for the charge density, $n(\mathbf{r})$ rather than for the many-electron wavefunction ψ. This is a massive simplification, as we only need consider a function of three variables x, y and z rather than the 3N variable problem above. Its basis is the well-known Hohenberg-Kohn (HK) theorem[4], which claims that all properties of a system can be considered to be unique functionals of its ground state density.

2.3 The Hohenberg-Kohn (HK) Theorems

Prior to the work of Hohenberg and Kohn in 1964 the use of the electron density as a fundamental variable was thought of as a somewhat ad hoc approach. However, Hohenberg and Kohn showed that this method may in principle enable the calculation of the exact ground-state energy. The Hohenberg and Kohn first theorem states that for any system of interacting particles in an external potential $V_{ext}(\mathbf{r})$, the density is uniquely determined (in other words, the external potential is a unique functional of the density). Thus the ground state particle density determines the full Hamiltonian. In principle, all the states including ground and excited states of the many-body wavefunctions can be calculated. This means that the ground state particle density uniquely determines all properties of the system completely.

Proof of theorem I: assume that we have two different external potentials $V_{ext}(\mathbf{r})$ and $V'_{ext}(\mathbf{r})$ which differ by more than a constant and lead to the same ground state density $n_0(\mathbf{r})$. The two external potentials would give two different Hamiltonians, $\hat{H}$ and $\hat{H}'$, which have the same ground state

density $n_0(\mathbf{r})$ but would have different ground state wavefunctions, ψ and ψ', with $\hat{H}\,\psi = E_0\psi$ and $\hat{H}'\,\psi' = E'_0\,\psi'$.

$$\begin{aligned} E_0 &< \langle \psi' \,|\, \hat{H} \,|\, \psi' \rangle \\ &< \langle \psi' \,|\, \hat{H}' \,|\, \psi' \rangle + \langle \psi' \,|\, \hat{H} - \hat{H}' \,|\, \psi' \rangle \\ &< E'_0 + \int n_0(\mathbf{r})[V_{ext}(\mathbf{r}) - V'_{ext}(\mathbf{r})]d\mathbf{r} \end{aligned} \qquad (2.9)$$

Similarly

$$\begin{aligned} E'_0 &< \langle \psi \,|\, \hat{H}' \,|\, \psi \rangle \\ &< \langle \psi \,|\, \hat{H} \,|\, \psi \rangle + \langle \psi \,|\, \hat{H}' - \hat{H} \,|\, \psi \rangle \\ &< E_0 + \int n_0(\mathbf{r})[V'_{ext}(\mathbf{r}) - V_{ext}(\mathbf{r})]d\mathbf{r} \end{aligned} \qquad (2.10)$$

Adding Eq. (2.9) and (2.10) lead to the contradiction

$$E_0 + E'_0 < E_0 + E'_0 \qquad (2.11)$$

Which is clearly a contradiction. Hence, no two different external potentials $V_{ext}(\mathbf{r})$ can give rise to the same ground state density $n_0(r)$, i.e., the ground state density determines the external potential $V_{ext}(\mathbf{r})$. Thus, the theorem has been proven by reductio ad absurdum.

The second theorem of HK states that there exists a universal functional $F[n(\mathbf{r})]$ of the density, independent of the external potential $V_{ext}(\mathbf{r})$, such that the global minimum value of the energy functional $E[n(r)] \equiv \int n(\mathbf{r})V_{ext}(\mathbf{r})dr + F[n(\mathbf{r})]$ is the exact ground state energy of the system and the exact ground state density $n_0(\mathbf{r})$ minimizes this functional. Thus the exact ground state energy and density are fully determined by the functional $E[n(\mathbf{r})]$.

The universal functional F[n(**r**)] written as

$$F[n(\mathbf{r})] \equiv T[n(\mathbf{r})] + E_{\text{int}}[n(\mathbf{r})] \qquad (2.12)$$

Where T[n(**r**)] is the kinetic energy and E_{int}[n(**r**)] is the interaction energy of the particles. According to variational principle, for any wavefunction ψ′, the energy functional E[ψ′]:

$$E[\psi'] < \langle \psi' | \hat{T} + \hat{V}_{\text{int}} + \hat{V}_{\text{ext}} | \psi' \rangle \qquad (2.13)$$

According to the theorem I, ψ′ correspond to a ground state with particle density n′(**r**) and external potential V'_{ext}(**r**), then E[ψ′] is a functional of n′(**r**). According to variational principle:

$$\begin{aligned} E[\psi'] &\equiv \langle \psi' | \hat{T} + \hat{V}_{\text{int}} + \hat{V}_{\text{ext}} | \psi' \rangle \\ &= E[n'(\mathbf{r})] \\ &= \int n'(\mathbf{r}) V_{ext}'(\mathbf{r}) dr + F[n'(\mathbf{r})] \\ &> E[\psi_0] \\ &= \int n_0(\mathbf{r}) V_{ext}'(\mathbf{r}) dr + F[n_0(\mathbf{r})] \\ &= E[n_0(\mathbf{r})] \end{aligned} \qquad (2.14)$$

By minimizing the total energy functional $E[n(r)] \equiv \int n(\mathbf{r}) V_{ext}(\mathbf{r}) dr + F[n(\mathbf{r})]$ we can obtain the ground state energy $E[n_0(\mathbf{r})]$ of the system with respect to variations in the density n(**r**). The HK theorems put particle density $n(\mathbf{r})$ as the basic variable, it is still impossible to calculate any property of a system because the universal functional $F[n(\mathbf{r})]$ is unknown. This difficulty was overcome by Kohn and Sham [40] in 1965.

2.4 The Kohn-Sham equations

The Hohenberg-Kohn theorem offers no practical guide to the explicit construction of the $F[n(\mathbf{r})]$ universal functional. For this purpose one still has to face the full intricacies of the many-body problem. The KS equation is to replace the original many-body system by an auxiliary

independent-particle system and assume that the two systems have exactly the same ground state density. Kohn and Sham (KS) addressed this problem in 1966, by introducing an auxilliary system containing N non interacting electrons in a background potential $V_{eff}(\mathbf{r})$, chosen such that the charge density in this auxilliary system is exactly the same as that in the full interacting system:

$$n(\mathbf{r}) = \sum_{i=1}^{N} |\psi_i(\mathbf{r})|^2 \qquad (2.15)$$

It is simple to calculate the kinetic energy of the *non-interacting* system of electrons where the electrons are in these states using

$$T_s[n(\mathbf{r})] = -\frac{1}{2}\sum_{i=1}^{N} \psi_i^*(\mathbf{r})\nabla^2\psi_i(\mathbf{r})d\mathbf{r} \qquad (2.16)$$

The true kinetic energy of the interacting system will of course differ from this, and the difference between this term and the exact result is treated separately. The total energy is given by

$$E[n(\mathbf{r})] \equiv \int n(\mathbf{r})V_{ext}(\mathbf{r})d\mathbf{r} + F[n(\mathbf{r})] \qquad (2.17)$$

Then the universal functional $F[n(\mathbf{r})]$ was rewritten as

$$F[n(\mathbf{r})] = T_s[n(\mathbf{r})] + E_H[n(\mathbf{r})] + E_{XC}[n(\mathbf{r})] \qquad (2.18)$$

Where T_s is the Kohn–Sham kinetic energy for non-interacting system. $E_H[n(\mathbf{r})]$ is the classic electrostatic (Hartree) energy of the electrons

$$E_H[n(\mathbf{r})] = \frac{1}{2}\int\int \frac{n(\mathbf{r})n(\mathbf{r}')}{|\mathbf{r}-\mathbf{r}'|}d\mathbf{r}d\mathbf{r}' \qquad (2.19)$$

$E_{XC}[n(\mathbf{r})]$ contains the exchange and correlation energies and the correction to the kinetic energy. In order to obtain the ground state energy we minimize the energy of eq. 2.17 (theorem 2), subject to the constraint the number of electrons N is conserved

$$\delta[E[n(\mathbf{r})] - (\mu\int n(\mathbf{r})d\mathbf{r} - N)] = 0 \qquad (2.20)$$

And the resulting equation is

$$\mu = \frac{\delta F[n(\mathbf{r})]}{\delta n(\mathbf{r})} + V_{ext}[n(\mathbf{r})] \qquad (2.21)$$

$$\mu = \frac{\delta T_s[n(\mathbf{r})]}{\delta n(\mathbf{r})} + V_{KS}[n(\mathbf{r})] \qquad (2.22)$$

Where μis the chemical potential,

$$V_{KS}(\mathbf{r}) = V_{ext}(\mathbf{r}) + V_H(\mathbf{r}) + V_{XC}(\mathbf{r}) \qquad (2.23)$$

$$V_{KS}(\mathbf{r}) = V_{ext}(\mathbf{r}) + \frac{\delta E_H[n(\mathbf{r})]}{\delta n(\mathbf{r})} + \frac{\delta E_{XC}[n(\mathbf{r})]}{\delta n(\mathbf{r})} \qquad (2.24)$$

To find the ground-state density $n_0(\mathbf{r})$ for this non-interacting system we simply solve the one-electron Schrödinger equations;

$$(\frac{1}{2}\nabla^2 + V_{KS})\psi_i(\mathbf{r}) = \varepsilon_i\psi_i(\mathbf{r}) \qquad (2.25)$$

Equations (2.15), (2.24), (2.25) together are the well-known KS equations, which must be solved self-consistently because $V_{KS}(\mathbf{r})$ depends on the density through the XC potential.

2.5 Approximations

Both the Hohenberg-Kohn formulation as well as the approach by Kohn-Sham are formally exact and therefore allow in principle an exact solution provided that the functional $E_{xc}[n(\mathbf{r})]$ is exactly known. In practice this is never the case, which reveals the crucial point in density functional theory. Every calculatory approach in DFT stands and falls with the quality of the approximation for the unknown functionals $E_{xc}[n(\mathbf{r})]$. We will now review some of the common approximations made for E_{xc}.

2.5.1 Local Density Approximation (LDA).

Local-density approximations (LDA) are a class of approximations to the exchange–correlation (XC) energy functional that depend solely upon the value of the electronic density at each point in space (and not, for example, derivatives of the density or the Kohn–Sham orbitals). Many approaches can yield local approximations to the XC energy. However, overwhelmingly successful local approximations are those that have been derived from the homogeneous electron gas (HEG) model. The total exchange-correlation functional $E_{XC}[n(\mathbf{r})]$ can be written as,

$$\begin{aligned} E_{XC}^{LDA}[n(\mathbf{r})] &= \int n(\mathbf{r})\varepsilon_{XC}^{hom}(n(\mathbf{r}))d\mathbf{r} \\ &= \int n(\mathbf{r})[\varepsilon_{X}^{hom}(n(\mathbf{r})) + \varepsilon_{C}^{hom}(n(\mathbf{r}))]d\mathbf{r} \\ &= E_{X}^{LDA}[n(\mathbf{r})] + E_{C}^{LDA}[n(\mathbf{r})] \end{aligned} \qquad (2.26)$$

The local spin density approximation (LSDA) [41] has two quantities, the spin-up and spin down charge densities, and it is a straightforward generalization of the LDA to include electron spin.

$$E_{XC}^{LDA}[n_{\uparrow}(\mathbf{r}), n_{\downarrow}(\mathbf{r})] = \int n(\mathbf{r})\varepsilon_{XC}^{hom}(n_{\uparrow}(\mathbf{r}), n_{\downarrow}(\mathbf{r}))d\mathbf{r} \qquad (2.27)$$

2.5.2 Generalized-Gradient Approximation (GGA)

As the LDA approximates the energy of the true density by the energy of a local constant density, it neglects the inhomogeneities of the real charge density which could be very different from the HEG (homogenous electronic gas). The XC energy of inhomogeneous charge density can be significantly different from the HEG results. An improvement to this can be made by considering the gradient of the electron density, the so-called Generalized Gradient Approximation (GGA). Symbolically this can be written as

$$E_{XC}^{GGA} = E_{XC}^{GGA}[n(\mathbf{r}), \nabla n(\mathbf{r})] \qquad (2.28)$$

GGA also reproduces the binding energies, atomic energies, bond lengths better than LSDA, Nevertheless there still exist some system which cannot be described properly by GGA because of its semi-local nature. What is worst that no systematic way has been developed to improve the functional for exchange and correlation. The problems are most severe in materials in which the electrons tend to be localized and strongly interacting, such as transition metal nitrides and rare earth elements and compounds [42].

2.6 The (L)APW + lo method

2.6.1 The augmented plane-wave method (APW)

The APW method was developed by Slater in 1937 [43]. The space is partitioned into two regions: near the nuclei and away from them (Fig. 3.1). When electrons are far away from the nuclei, they show the behavior of free electrons, and are then suitably described by plane waves. While close to the nuclei, electrons bind strongly to their nuclei, their behavior is quite as in a free atom and they could be described more efficiently by atomic like functions.

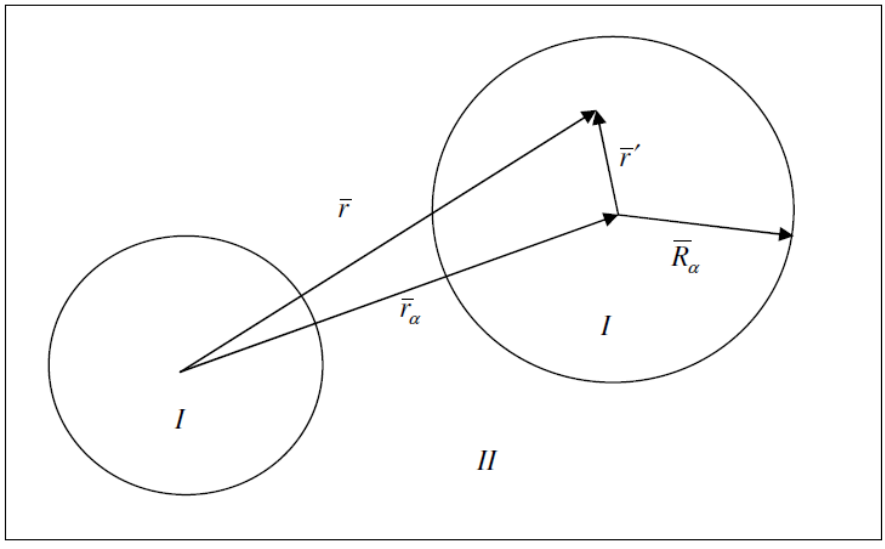

Figure 2.1 Schematic division of space into muffin-tin spheres and interstitial region.

Inside the muffin-tins the potential is approximated by a spherically symmetric shape, and in many implementations the interstitial potential is set to a constant. Correspondingly, the potential in the whole space can be defined as

$$V(\vec{r}) = \begin{cases} V(\vec{r}) & r \in I \\ constant & r \in II \end{cases} \tag{2.29}$$

Two types of basis sets are used in the two different regions

$$\phi_{\vec{K}}^{\vec{k}}(\vec{r}, E) = \begin{cases} \frac{1}{\sqrt{\Omega}} e^{i(\vec{k}+\vec{K})\vec{r}} & (\vec{r} \in II) \\ \sum_{lm} A_{lm}^{\alpha,\vec{k}+\vec{K}} u_l^{\alpha}(r', E) Y_m^l(\hat{r}') & (\vec{r} \in I) \end{cases} \tag{2.30}$$

Where $\vec{k}$ is the Bloch vector, Ω is the cell volume, $\vec{K}$ is a reciprocal lattice vector, l and m are the quantum numbers, Y_m^l is spherical harmonics and $u_l^{\alpha}(r', E)$ is the regular solution of the radial Schrödinger equation.

$$\left\{ -\frac{d^2}{dr^2} + \frac{l(l+1)}{r^2} + V(r) - E_0 \right\} r u_l^{\alpha}(r, E) = 0 \tag{2.31}$$

For a given energy parameter E_0, V(r) is the spherical component of the potential. The coefficients A_{lm} is determined by requiring that the wave functions in the MT and the interstitial regions match each other at the MT boundary [44]. Thus, each plane wave is augmented by an atomic-like function in every atomic sphere and constitutes thus the basis set used to expand the wave function. In the alternative notation,

$$\vec{K} + \vec{k} = \vec{k}_n, \ \phi_{\vec{K}}^{\vec{k}} = \phi_{\vec{k}_n}$$

n defines the band index. Then, the basis set used to expand the wave function is

$$\psi_{\vec{k}} = \sum_n C_n \phi_{\vec{k}_n}(\vec{r}) \tag{2.32}$$

The biggest disadvantage in the APW method is that it cannot get the eigenvalues from a single diagonalization due to the unknown parameter *E* in Eq. (2.30). The exact *E* value, which is what we want to know, is needed to describe the eigenstate $\psi_{\vec{k}n}(r)$ accurately. Since this energy depends on the function $u_l^{\alpha}(r', E)$, the resulting eigenvalue problem is non-linear in energy. To overcome this problem linearized variations of the APW method have been developed, where the energy *E* is set to a fixed value E_0 and the basis functions are modified to gain extra flexibility to cover a larger energy region around their linearization energy. The linearized APW method (LAPW) and the APW + local orbitals (APW + lo) will be discussed in more detail in the next sections.

2.6.2 The linearized augmented plane wave method (LAPW)

In order to overcome the non-linearity problem in the APW method, Anderson developed the linearized augmented plane wave method (LAPW) [5, 45]. In this approach the basis functions are expended in the same way as in Eq. (2.30) in the interstitial, but inside the muffin-tin the basis functions do not only depend on the function u_l, but also on its derivative $\dot{u}_l \equiv \partial u_l / \partial E$. The radial function u_l can be expanded into a Taylor-series around E_0.

$$u_l^{\alpha}(r', \varepsilon_{\vec{k}}^n) = u_l^{\alpha}(r', E_0) + (E_0 - \varepsilon_{\vec{k}}^n)\dot{u}_l^{\alpha}(r', E_0) + O(E_0 - \varepsilon_{\vec{k}}^n)^2 \tag{2.33}$$

Here $\dot{u}_l$ denotes the energy derivative of u_l, and $O(E_0 - \varepsilon_{\vec{k}}^n)^2$ denotes errors that are quadratic in the energy difference. The radial function error is second order, and the energy error is of fourth order [46]. When E_0 is set near $\varepsilon_{\vec{k}}^n$, the radial function and energy errors are negligible. Substituting Eq. 2.33 into Eq. 2.30, we get the formulation of the LAPW basis set,

$$\phi_{\vec{K}}^{\vec{k}}(\vec{r}) = \begin{cases} \frac{1}{\sqrt{\Omega}} e^{i(\vec{k}+\vec{K})\vec{r}} & r \in II \\ \sum_{lm} (A_{lm}^{\alpha,\vec{k}+\vec{K}} u_l^{\alpha}(r', E_0) + B_{lm}^{\alpha,\vec{k}+\vec{K}} \dot{u}_l^{\alpha}(r', E_0)) Y_m^l(\hat{r}') & r \in I \end{cases} \quad (2.34)$$

In order to have basis sets which describe for every atom including s-, p-, d-, and f states, the final definition of the basis sets for LAPW is:

$$\phi_{\vec{K}}^{\vec{k}}(\vec{r}) = \begin{cases} \frac{1}{\sqrt{\Omega}} e^{i(\vec{k}+\vec{K})\vec{r}} & r \in II \\ \sum_{lm} (A_{lm}^{\alpha,\vec{k}+\vec{K}} u_l^{\alpha}(r', E_{1,l}^{\alpha}) + B_{lm}^{\alpha,\vec{k}+\vec{K}} \dot{u}_l^{\alpha}(r', E_{1,l}^{\alpha})) Y_m^l(\hat{r}') & r \in I \end{cases} \quad (2.35)$$

The two parameters, A and B are to be determined through two boundary conditions. These two conditions are such that the function inside the sphere matches the plane waves both in value and in slope at the sphere boundary. u_l and $\dot{u}_l$ are orthogonal. $\dot{u}_l$ is calculated from a Schrodinger-like equation, derived by taking the energy derivative of (3.31) with respect to *E*:

$$\left\{ -\frac{d^2}{dr^2} + \frac{l(l+1)}{r^2} + V(r) - E_0 \right\} r\dot{u}_l(r, E) = r u_l(r, E) \quad (2.36)$$

It is very clear that the LAPW method is thus more flexible than the APW in the MT spheres. By linearizing the APWs the problem of having energy dependent basis function is resolved.

2.6.3 The linearized augmented plane wave with local orbitals (LAPW+LO)

The electrons can be divided into two types. One type of electrons called core states, which do not participate directly in chemical bonding with other atoms and must be confined within the muffin-tin sphere. The other type of electrons called valence states, who are leaking out of the MT sphere and bond with other atoms. However, for many elements, the electrons cannot be clearly distinguished like that. Some states are neither constrained in the core states, nor lie in the valence

states and are correspondingly termed semi-core states. They have the same angular quantum number *l* as the valence states but with lower principal quantum number *n*. When applying LAPW on these states, it is thus hard to use one $E_{1,l}$ to determine the two same *l* in Eq. 2.35. The problem is solved by introducing local orbitals (LO), which are defined as

$$\phi_{\alpha,LO}^{lm}(\vec{r}) = \begin{cases} 0 & r \in II \\ \sum_{lm} (A_{lm}^{\alpha,LO} u_l^{\alpha}(r', E_{1,l}^{\alpha}) + B_{lm}^{\alpha,LO} \dot{u}_l^{\alpha}(r', E_{1,l}^{\alpha}) + C_{lm}^{\alpha,LO} u_l^{\alpha}(r', E_{2,l}^{\alpha})) Y_m^l(\hat{r}') & r \in I \end{cases} \quad (2.37)$$

where $E_{1,l}^{\alpha}$ is an energy value suitable for the highest in energy state and $E_{2,l}^{\alpha}$ is an energy value at which the lower valence state is peaked. Since LO's are not connected to plane waves in the interstitial, they have no $\vec{k}$ or $\vec{K}$ dependence. The coefficients *A*, *B* and *C* are determined by requiring that the local orbitals are normalized, and have zero value and zero slope at the muffin tin boundary.

2.6.4 The augmented plane wave plus local orbitals (APW+lo)

An alternative method to linearize the APW method is the APW + local orbitals method [47-49]. The basis set of the introduced APW+lo method is also energy independent and still has the same size as the original APW method. In order to achieve that a new local orbital (lo) is added (these local orbitals have nothing to do with the local orbitals "LO" introduced in the previous method *LAPW+LO* in order to solve the problem of valence states with equal *l* and different *n*) to gain enough variational flexibility in the radial basis functions. The APW+lo method combines the good features of the APW and the LAPW+LO methods. The basis set of APW+lo contains two kinds of functions, which are defined as

The first kind is the APW basis set with a fixed energy $E_{1,l}^{\alpha}$

$$\phi_{\vec{K}}^{\vec{k}}(\vec{r},E)=\begin{cases}\dfrac{1}{\sqrt{\Omega}}e^{i(\vec{k}+\vec{K})\vec{r}} & r\in II\\ \sum_{lm}A_{lm}^{\alpha,\vec{k}+\vec{K}}u_l^{\alpha}(r',E_{1,l}^{\alpha})Y_m^l(\hat{r}') & r\in I\end{cases} \tag{2.38}$$

The second kind is:

$$\phi_{\alpha,lo}^{lm}(\vec{r})=\begin{cases}0 & r\in II\\ \sum_{lm}(A_{lm}^{\alpha,lo}u_l^{\alpha}(r',E_{1,l}^{\alpha})+B_{lm}^{\alpha,lo}\dot{u}_l^{\alpha}(r',E_{1,l}^{\alpha}))Y_m^l(\hat{r}') & r\in I\end{cases} \tag{2.39}$$

where the two coefficients *A* and *B* are determined by normalization, and by requiring that the local orbital has zero value at the Muffin-tin boundary. The advantage of the APW+lo method is that it has the same small basis set size as the APW method, and has the same accuracy compared to the LAPW method. Also the APW +lo method is faster than LAPW method if we deal with a system that has a large number of atoms in the unit cell, because there are more functions.

2.6.5 The full potential (L)APW+lo method

A mixed augmentation ((L)APW+lo) has been proposed by Madsen et al [49], where the physically important *l* quantum numbers are treated by APW+lo method, and the higher *l* quantum numbers with LAPW. All the data presented in our work are using this hybrid basis set (L)APW+lo. The accuracy of (L)APW+lo method can be further improved by considering the full potential (FP), and expand it similar to the wave functions,

$$V(\vec{r})=\begin{cases}\sum_{\vec{K}}V_{\vec{K}}e^{i\vec{K}\vec{r}} & r\in I\,I\\ \sum_{lm}V_{lm}(r')Y_{lm}(\hat{r}') & r\in I\end{cases} \tag{2.40}$$

This is also called non-muffin-tin correction. In this case, the radial function u_l in Eq. 2.31 is not the exact solution inside the MT sphere. It should be evaluated for the true MT potential.

Chapter III

3. General issues of magnetism

3.1 Introduction

Magnetism, the phenomenon by which materials assert an attractive or repulsive force or influence on other materials, has been known for thousands of years. However, the underlying principles and mechanisms that explain the magnetic phenomenon are complex and subtle, and their understanding has eluded scientists until relatively recent times [50]. Magnetism plays a crucial role in the development of memories for mass storage, and in sensors to name a few. Spintronics is an integration of the magnetic material with semiconductor technology, to realize nanosized devices with better features like non-volatility, scaling, etc.

We will discuss in this chapter the origin of magnetism and the various phenomena of diamagnetism, paramagnetism, ferromagnetism, anti-ferromagnetism and ferrimagnetism. We will present the two basic theories of magnetism-localized moment theory (Heisenberg model) and itinerant electron theory (Stoner model).

3.2 Origins of magnetism

The macroscopic magnetic properties of materials are a consequence of *magnetic moments* associated with individual electrons. Electrons in an atom have magnetic moments that originate from two types of motions (see Fig. 3.1), one is the motion of the electrons in an orbit around the nucleus, similar to the motion of the planets in our solar system around the sun, and the other is the spin of the electrons around its axis, analogous to the rotation of the Earth about its own axis. The orbital and the spin motion independently impart a magnetic moment on each electron causing each of them to behave as a tiny magnet.

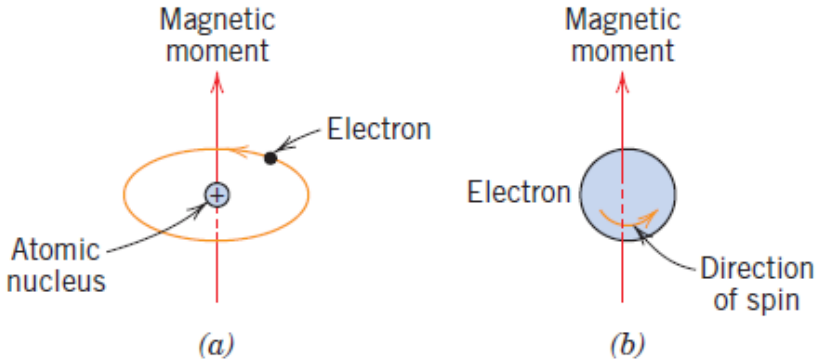

Figure 3.1 Demonstration of the magnetic moment associated with (*a*) an orbiting electron and (*b*) a spinning electron.

The unit of magnetic moment is called the "Bohr magneton" μ_B which is of magnitude 9.27×10^{-24} $J.T^{-1}$. For each electron in an atom the spin magnetic moment is $\pm\mu_B$ and the orbital magnetic moment contribution is equal to $m_l\mu_B$, m_l: being the magnetic quantum number of the electron. In a large fraction of the elements, the magnetic moment of the electrons cancel out because of the Pauli Exclusion Principle, which states that each electronic orbit can be occupied by only two electrons of opposite spin. However, a number of so-called transition metal atoms, such as iron, cobalt, and nickel, have magnetic moments that are not cancelled; these elements are, therefore, common examples of magnetic materials. In these transition metal elements the magnetic moment arises only from the spin of the electrons. In the rare earth elements (that begin with lanthanum in the sixth row of the Periodic Table of Elements), however, the effect of the orbital motion of the electrons is not cancelled, and hence both spin and orbital motion contribute to the magnetic moment. Examples of some magnetic rare earth elements are: cerium, neodymium, samarium, and europium [51].

3.3 Main classes of magnetic behavior

A material is magnetically characterized based on the way it can be magnetized, this depends on the material's magnetic susceptibility (its magnitude and sign). Types of magnetism

can be classified on the basis of the magnetic behavior of materials in response to magnetic fields at different temperatures. These types of magnetism are: ferromagnetism, ferrimagnetism, antiferromagnetism, paramagnetism, and diamagnetism.

3.3.1 Diamagnetism

Diamagnetic substances are composed of atoms which have no net magnetic moments (i.e., all the orbital shells are filled and there are no unpaired electrons). Is a very weak form of magnetism that is nonpermanent and persists only while an external field is being applied. The applied external field acts on atoms of a material, slightly unbalancing their orbiting electrons, and creates small magnetic dipoles within atoms which oppose the applied field (see Fig. 3.2). This action produces a negative magnetic effect known as diamagnetism. The magnitude of the induced magnetic moment is extremely small. From Fig. 3.3 we can see that the magnetization (M) direction is opposite to the direction of applied field (H), and the susceptibility is on the order of -10^{-5}. The other characteristic behavior of diamagnetic materials is that the susceptibility is temperature independent.

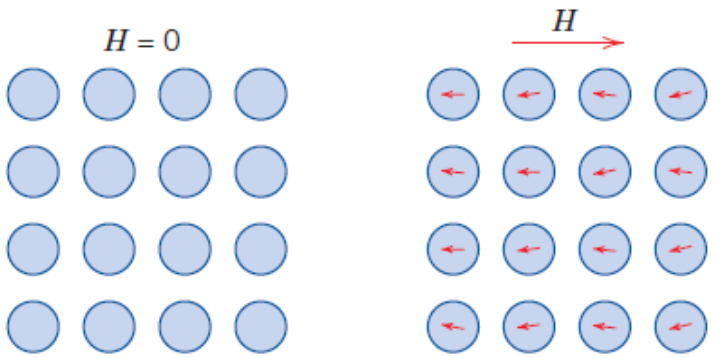

Figure 3.2 The atomic dipole configuration for a diamagnetic material with and without a magnetic field. In the absence of an external field, no dipoles exist; in the presence of a field, dipoles are induced that are aligned opposite to the field direction.

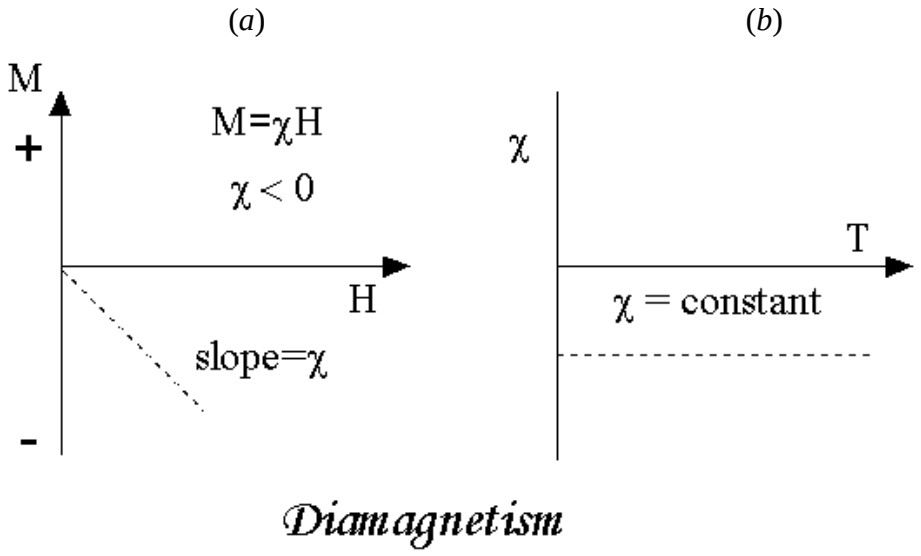

Figure 3.3 (*a*) the magnetization versus magnetic field curve, (*b*) temperature dependence of magnetic susceptibility.

3.3.2 Paramagnetism

Paramagnetic materials have a net magnetic moment due to the presence of unpaired electrons in the outermost orbitals. However, the individual magnetic moments do not interact magnetically, and like diamagnetism, the magnetization is zero when the field is removed. In the presence of a field, there is a partial alignment of the atomic magnetic moments in the direction of the field (Fig. 3.4), resulting in a net positive magnetization and positive susceptibility (Fig. 3.5*a*) lies in the range $+10^{-5}$ to $+10^{-2}$.

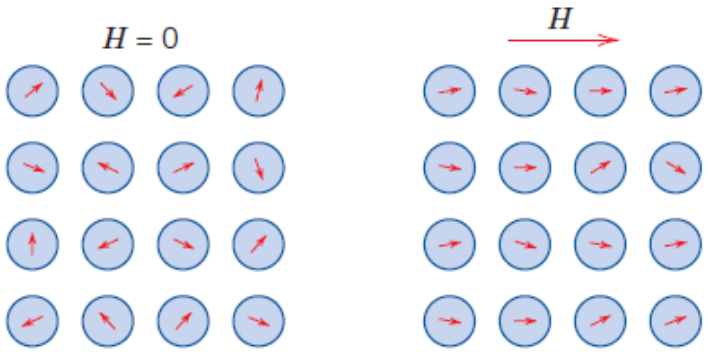

Figure 3.4 The alignment of atomic magnetic moments for a paramagnetic material with and without a magnetic field.

As the temperature increases, then the thermal agitation will increase and it will become harder to align the atomic magnetic moments and hence the susceptibility will decrease (Fig. 3.5*b*).

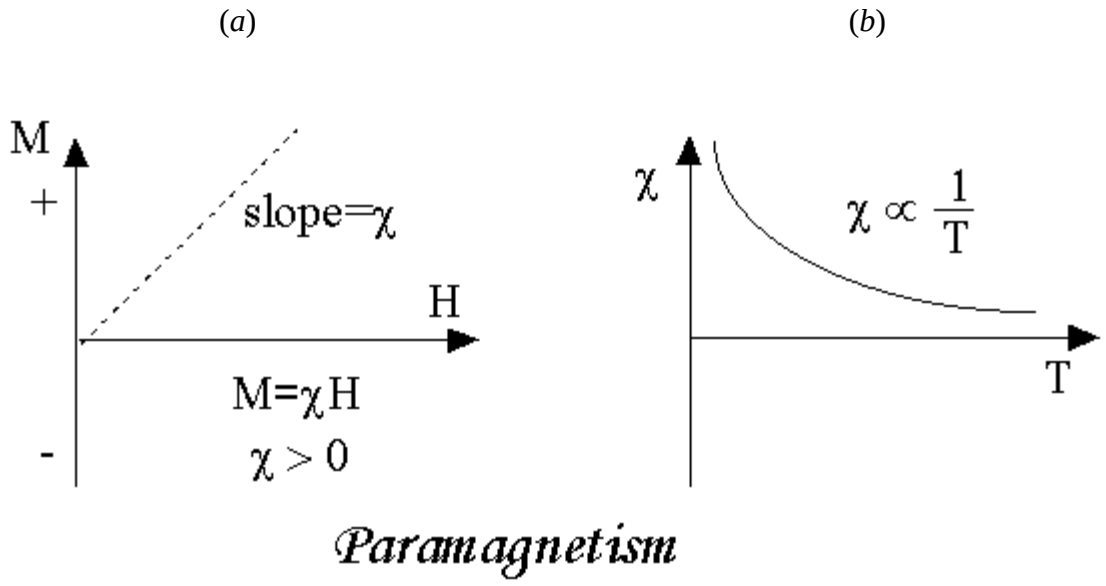

Figure 3.5 (*a*) the magnetization versus magnetic field curve, (*b*) temperature dependence of magnetic susceptibility.

3.3.3 Ferromagnetism

Ferromagnetic materials exhibit parallel alignment of moments as shown in Figure 3.6, which results in a large net magnetization at room temperature, even in the absence of a magnetic field. In quantum mechanics, the Heisenberg model of ferromagnetism describes the parallel alignment of magnetic moments in terms of an exchange interaction between neighbouring moments.

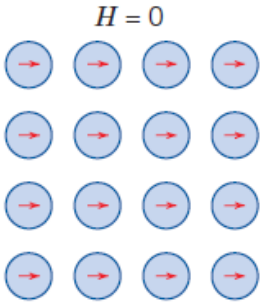

Figure 3.6 The alignment of atomic magnetic moments for a ferromagnetic material, which will exist even in the absence of an external magnetic field.

Weiss postulated the presence of magnetic domains within the material. A magnetic domain is a region within a magnetic material in which the magnetization is in a uniform direction. This means that the individual magnetic moments of the atoms are aligned with one another and they point in the same direction. The movement of these domains determines how the material responds to a magnetic field and as a consequence the susceptible is a function of applied magnetic field. Therefore, ferromagnetic materials are usually compared in terms of saturation magnetisation (magnetisation when all domains are aligned) rather than susceptibility. The transition metals iron (as BCC ferrite), cobalt, nickel, and some of the rare earth metals such as gadolinium (Gd) are typical examples of ferromagnetic (FM) materials.

Above the Curie temperature, ferromagnetic materials behave as paramagnetic materials and their susceptibility is given by the Curie-Weiss law, defined as

$$\chi_m = \frac{C}{T - T_c} \qquad (3.1)$$

where C : material constant, T : temperature, T_c : Curie temperature.

3.3.4 Antiferromagnetism

Antiferromagnetic materials are very similar to ferromagnetic materials but the exchange interaction between neighbouring atoms leads to the antiparallel alignment of the atomic magnetic moments. Therefore, the net moment is zero. This type of magnetic ordering is shown in Figure 3.7. The atomic magnetic moments exhibit very strong interactions, which are produced by electronic exchange forces that have quantum origins. This exchange interaction is responsible for parallel alignment of spins and is extremely sensitive to interatomic spacing and to the atomic positions. This sensitivity causes antiparallel alignment of spins. Like ferromagnetic materials these materials become paramagnetic above a transition temperature, known as the Néel temperature, T_N. (Cr: T_N=37ºC).

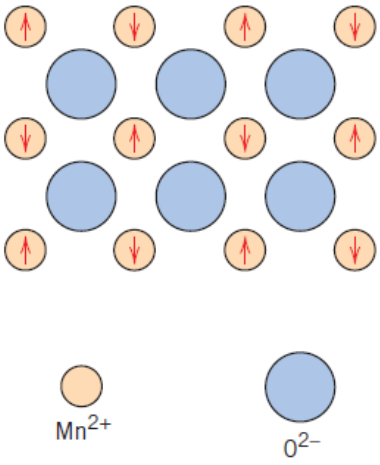

Figure 3.7 The alignment of atomic magnetic moments for antiferromagnetic manganese oxide, the moments are aligned oppositely and have the same magnitudes. This is in the absence of an applied magnetic field.

3.3.5 Ferrimagnetism

More complex forms of magnetic ordering as shown in Figure 3.8 can occur in ferrimagnets where, the magnetic moments of two nearby sub-lattices are opposite but unequal, unlike in AFM. When a magnetic field is absent the material has a spontaneous magnetism which is the result of ordered magnetic moments.

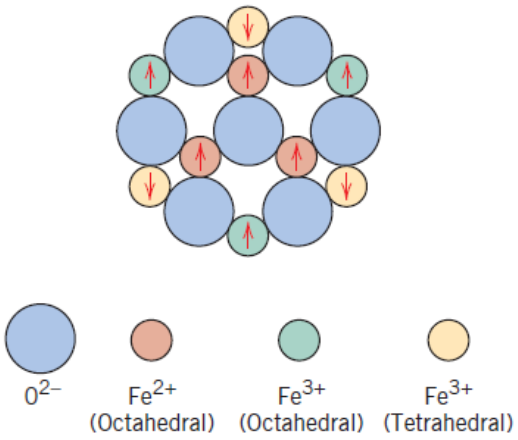

Figure 3.8 The alignment of atomic magnetic moments for ferrimagnetic Fe_3O_4. The moments are aligned oppositely and have different magnitudes due to being made up of two different ions. This is in the absence of an applied magnetic field.

Below the Curie temperature the atoms of each ion are aligned anti-parallel with different momentums causing a spontaneous magnetism; the material is ferrimagnetic. Above the Curie temperature the material is paramagnetic as the atoms lose their ordered magnetic moments as the material undergoes a phase transition.

3.4 Magnetism in materials

There are two basic theories of magnetism, localized moment theory and itinerant electron theory. In localized moment theory, the valence electrons are attached to the atoms and cannot move about the crystal. The valence electrons contribute a magnetic moment which is localized at the atom. In the itinerant electron magnetic theory, electrons responsible for magnetic effects are ionized from the atoms and are able to move through the crystal. There are materials for which one or the other model is a rather good approximation [52].

The non-integral values of magnetic moment per atom, the high values of specific electronic heat coefficient which are not compatible with localized model, impose the use of itinerant model in case of transition metals and their alloys. But, this model cannot explain the *Curie-Weiss* law observed for all ferromagnetic metals for $T > T_C$, and the calculated value of *Curie* temperature is too big comparing to the experimental one, problems that are easily resolved by localized model [53].

It is very clear that *d* electrons should be treated as localized electrons in magnetic insulator compounds and as correlated itinerant electrons in transition metals. However, they are still in the stage of development and in many cases they cannot be separated from each other. For a deep understanding of magnetism in condensed matter there has been a trend to combine both models to develop a unified theory [54] .

3.4.1 Localized moments in solids

The modern theory of magnetism has started with the concept of a local magnetic moment of a fixed size. Within this concept Langevin gave an explanation for the Curie law of magnetic susceptibility [55]. Subsequently Weiss introduced the notion of an interaction (molecular field) between the atomic magnetic moments to explain the spontaneous magnetic order in solids. Combining this new concept with the studies of Langevin, Weiss was able to explain the finite temperature properties of ferromagnetic 3*d* transition metals [56].

In 1928 Heisenberg attributed the origin of Weiss molecular field to the quantum mechanical exchange interaction between the magnetic moments and proposed a more general model [57]. The magnetic interaction between localized moments, the magnetic coupling, determines the behaviour of a compound when placed in a magnetic field and may favor magnetic ordering. The magnetic coupling is usually described using the *Heisenberg* Hamiltonian:

$$H = -\sum_{i,j} J_{ij} \vec{S}_i \vec{S}_j \qquad (3.2)$$

Where J is the exchange integral, positive values of the Heisenberg coupling constant J correspond to parallel spin orientation (ferromagnetic coupling), negative ones to antiparallel spin orientation (antiferromagnetic coupling). The i and j can be restricted to run over all nearest neighbour or next nearest neighbour pairs of magnetic moments on account of the fact that the magnetic interaction is weak and decreases exponentially with distance. A spin operator of this form was first deduced from the *Heitler-London* results by *Dirac* [58] and first extensively applied in the theory of magnetism by *Van Vleck* [59]. If the orbitals of two neighbour atoms present a sufficient space extension so that an overlap is possible, the correlation effects lead to a direct interaction between the atoms spins. This phenomenon is known as *direct exchange*. The direct exchange is characteristic for *3d* intermetallic compounds, and represents the stronger interatomic interaction, being responsible for the magnetic order up to high temperatures. When magnetic orbitals of two

neighboring atoms are too localized to overlap, as in the case for the *4f* series, the exchange process can occur through conduction electrons if the system is metallic. This leads to an *indirect exchange* of *RKKY* type (*Ruderman*, *Kittel*, *Kasuya*, *Yosida*) [60-62]. If there are no conduction electrons, as in ceramics where magnetic atoms are separated by non-magnetic atoms like oxygen, the external electrons of the latter participate in covalent binding and mediate the exchange interaction. This is the *superexchange interaction*, which was introduced by Kramers [63] in 1934 in an early attempt to explain the magnetic interaction in antiferromagnetic ionic solids. The three main exchange mechanisms between localized moments are presented in Fig. 3.9. The Heisenberg model is actually justified when well-defined local atomic moments exist, like in the case of magnetic insulators and in the majority of rare-earth metals.

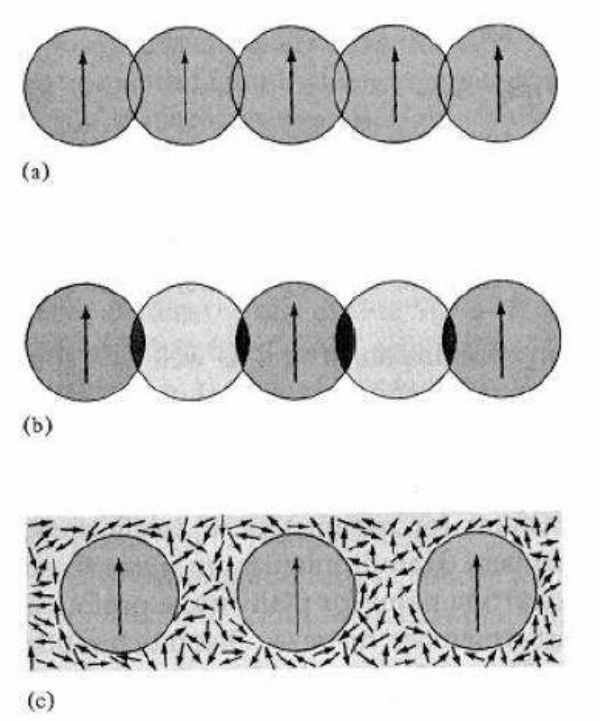

Figure 3.9 Schematic illustrations of possible coupling mechanisms between localized magnetic moments: (a) direct exchange between neighboring atoms, (b) superexchange mediated by non-magnetic ions, and (c) indirect exchange mediated by the conduction electrons.

3.4.2 Itinerant-electron magnetism

Opposite to the localized model is the itinerant (or band) model which considers that the magnetic carrier are the so called *Bloch* electrons which are itinerant through the solid. One of the main reasons for this is that the atomic moments in Fe, Co and Ni are not multiples of the Bohr magneton but rather odd fraction of it.

Bloch first discussed the possibility of ferromagnetism in an electron gas on the basis of Hartree-Fock approximation [64]. Later Wigner pointed out the importance of electron electron interactions on the suppression of the occurrence of ferromagnetism in electron gas [65]. Thus the occurrence of ferromagnetism in transition metals is considered to be connected with the atomic character of 3*d* electrons and mainly intra-atomic exchange interactions.

The Stoner model [66] is the simplest model of itinerant-electron magnetism, which has mainly been used to account for the existence of ferromagnetism in itinerant systems. If the relative gain in the exchange interaction (the interaction of electrons via Pauli's exclusionary principle) is larger than the loss in kinetic energy, the spin up and spin down electron bands will split spontaneously. The instability of non-magnetic state with respect to formation of ferromagnetic order is given by the Stoner criterion which is define by

$$IN(E_F) > 1 \qquad (3.3)$$

Where I is the intra-atomic exchange integral and $N(E_F)$ is the density of states at the Fermi level. The conditions favoring magnetic moments in metallic systems are obviously: a large value of the exchange energy, but also a large density of state at the Fermi level. The *d* transition elements show band ferromagnetism are presented in Fig. 3.10. However, the Stoner theory fails to explain the Curie-Weiss magnetic susceptibility observed in almost all ferromagnets and the measured T_C for *3d* metals are too high in comparison to the observed ones. Improvements to the Stoner model have been made that take into account the effect of spin fluctuations in a self-consistent

renormalized (SCR) way [54]. These studies built a bridge between two extreme limits of models (localized and itinerant) and unified them into one picture. In particular, these new theories have been very successful in describing several properties of weak itinerant ferromagnets [67].

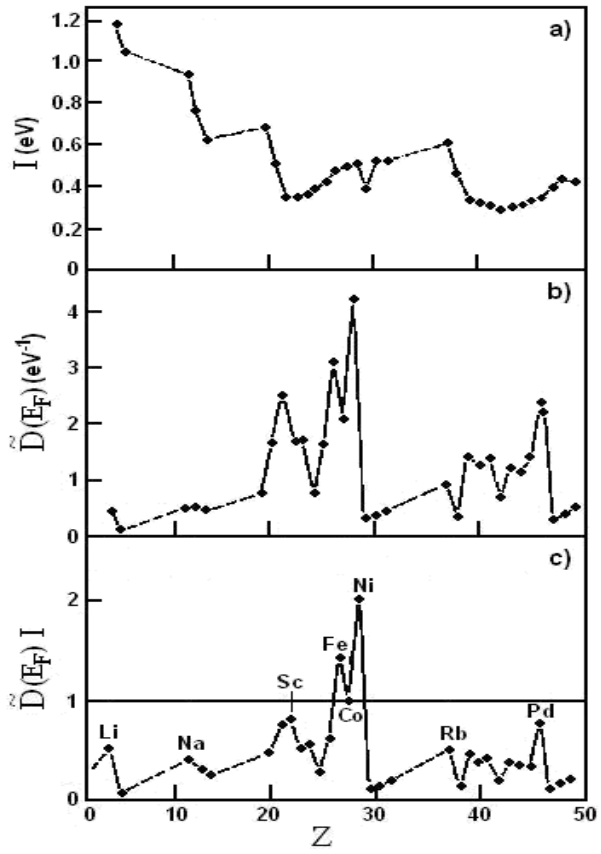

Figure 3.10 a) the Stoner parameter, b) the density of states at Fermi level, c) the Stoner criterion.

Chapter IV

4. Results and discussions

4.1 Structural, magnetic and electronic properties of the 3d transition metal mono-borides TM-B (TM= Mn, Fe, Co)

4.1.1 Introduction

In this chapter, we have selected MnB, FeB and CoB transition metal borides for a detail study of their structural, magnetic and electronic properties. The first investigations of iron, cobalt and nickel borides were made by Bjurström and Arnfeld (1929) [68] and Bjurström (1933) [69] who described the crystallographic structures of these borides. FeB belongs to the orthorhombic lattice (a = 10.408 au, b = 5.580 au and c =7.677 au) and the space group *Pnma* [68]. The boron atoms form zigzag chains between transition metal atoms. From the presence of boron chains, Kiessling [70, 71] postulated a covalent interaction between the boron atoms, which contributes to the stability of the monoborides [70]. With increasing boron content components of the boron spectrum indicate increasing covalent character and eventually become similar to those of the element itself. Later Kiessling's work was reviewed and extended by Aronson (1960) [72] who compared the structures of the borides and silicides with interstitial compounds of carbon and nitrogen. P. Mohn and D. G. Pettifor (1988) [11] reported that the transition-metal monoborides form a simple bonding mechanism of strong metalloid-metalloid (p-p) and transition metal-metalloid (d-p) interactions. So, the stability of the TM-B compounds is ruled by both a p-p and a p-d interaction. The B 2s and 2p states in FeB hybridise into 2s-p states and form rather strong covalent bonds, which cause one-dimensional zigzag chains of B atoms in FeB [73]. A study of the distribution of metals in two equilibrium phases of TM_1-TM_2-B ternary systems showed [74]

that the TM-B bond energy decreases with increasing atomic number. This is also indicated by a decrease in the melting point in the MnB-NiB series [75-78]. At the same time, the chemical stability of the monoborides increases as one moves toward the end of the period, a fact which is due to strengthening of B-B interaction [79].

The magnetic properties of the manganese, cobalt, and iron borides are summarized by Cadeville and Daniel (1966) [80] and by Fischer and Meyer (1967) [81]. It was observer that there is a regular decrease in the transition metal moment between the metal, the semiboride and the monoboride. The decrease of the magnetic moment with increasing boron content is due to the increasing number of electrons transferred from boron to the transition metal d band, which cause decreasing in the number of holes in one spin band. L. Guangwei and al. (1989) [73] studied the electronic structure of FeB and Fe_2B and they mentioned that there is no electron transfer occurs between Fe and B atoms in these two compounds. The bonding mechanism is found to be responsible for the fact that the magnetic moment of manganese in MnB is higher than that of iron in FeB. This means that the bonding mechanism is found to have a strong influence on the formation of the band splitting. In the case of a spin polarisation of the TM d band the B p states will not follow the band splitting. Any gain in exchange energy due to the splitting of the TM d bands is therefore compensated by a direct loss in bond energy of the TM d-B p bond for the minority band. The moment of FeB is smaller because of the loss in energy connected with this large band splitting [11].

Both Fe- and Co-based phases behave as strong ferromagnetic with a magnetic moment 2.217 μ_B [82], and 1.656 μ_B [83], respectively, while Mn-based phase is antiferromagnetic [83]. The magnetic states of our compounds are quite different: MnB and FeB are ferromagnetic[19]; CoB is not magnetic, but the diamagnetic behavior of the CoB phase was confirmed in Ref. [19]. The reported experimental magnetic moments give values ranging from 1.65 μ_B to 1.94 μ_B for

MnB, 1.12 μ_B for FeB, and 0 for CoB [80]. This chapter mainly investigates the structural, electronic, and magnetic properties of the 3*d* transition metal monoborides TM-B (TM=Mn, Fe, Co) in the non-spin-polarization and spin- polarization cases and under pressure within GGA and LSDA to show the effect of spin-polarization and pressure on the structural, electronic, and magnetic properties.

4.1.2 Calculations method

Our calculations are based on density functional theory DFT [4, 40, 84, 85] which is implemented in WIEN2K code [36]. Optimized crystal structures, calculated ground state parameters and all other properties were performed using FP-LAPW method [5]. In this method (see Chapter III), the unit cell of the crystal is divided into two regions. In the muffin-tin spheres the basis consists of atomic like functions, whereas in the interstitial region the basis functions are plane waves. Within this method, we have used the Perdew–Burke-Ernzerhof generalized gradient approximation (PBE-GGA) [7, 8] and the local spin density approximation (LSDA) of Perdew-Wang [6] for the exchange correlation energy. The muffin-tin sphere radii of TM and B atoms of all compounds studied are R_{MT} =1.8, 1.5 respectively. In order to show the dependence of the structural and electronic properties on spin-polarization, we kept the same convergence parameters between spin-polarization and non-spin-polarization calculations for all compounds studied. The value of the cut-off parameter is $R_{mt}\times K_{max}=8$ where R_{mt} is the muffin-tin sphere radii and K_{max} is the largest reciprocal lattice vector. The separation energy of valence and core states (cut-off energy) was chosen as -6 Ry. The energy convergence was chosen as 0.0001Ry during self-consistency cycles. The number of special *k*-points in the whole Brillouin zone (BZ) was selected as 1500.

4.1.3 Structural properties and magnetic stability

The TM-B compounds (MnB, FeB and CoB) crystallize in the orthorhombic FeB-type structure (see Fig. 4.1) with the space group *Pnma*, and four molecular units in the unit cell. The optimized atomic positions of our three compounds (SP GGA as an example) are listed in the Table 4.1.

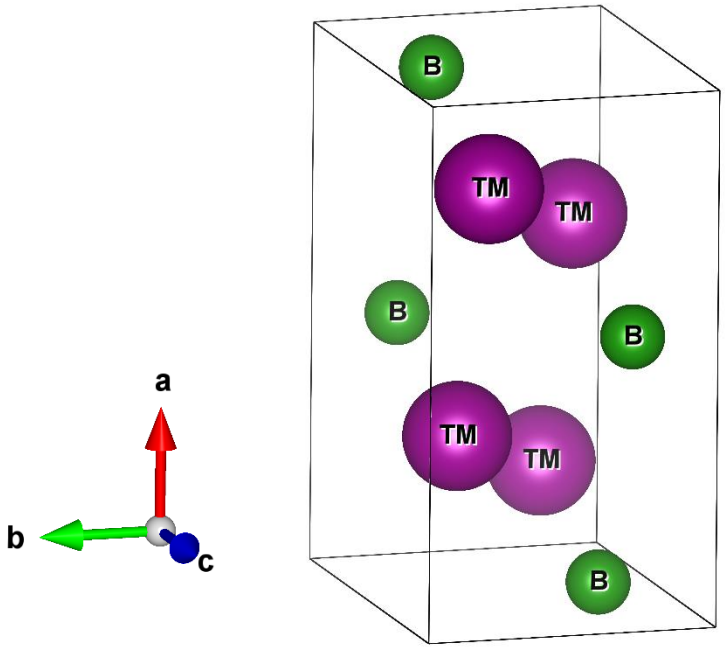

Figure 4.1 Crystal structure of TMB borides

Table 4.1 Optimized atomic positions of TMB compounds using SP GGA.

	MnB				**FeB**				**`CoB**		
Mn	0.1753	0.250	0.1222	**Fe**	0.6775	0.250	0.1205	**Co**	0.1772	0.250	0.1267
B	0.0338	0.250	0.6151	**B**	0.5347	0.250	0.6187	**B**	0.0313	0.250	0.6238

At the first step, we calculated the total energy versus volume for each compound with spin-polarization and without spin-polarization using LSDA and GGA. Fig. 4.2(*a*), Fig. 4.2(*b*) and Fig.

4.2(*c*) Show the total energy versus volume for MnB, FeB and CoB compounds with spin polarization and without spin polarization using GGA.

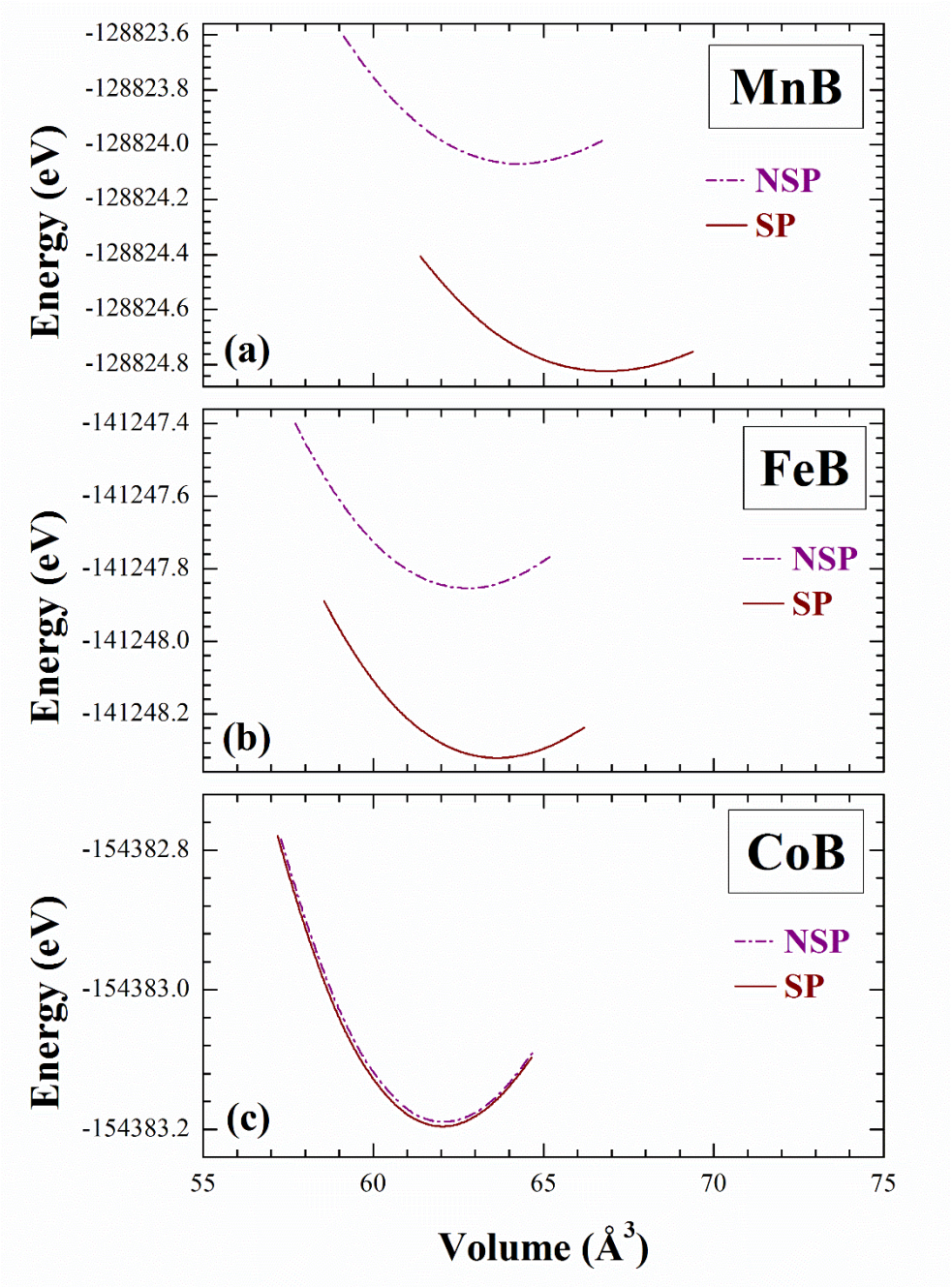

Figure 4.2 Spin polarization (SP) and non-spin polarization (NSP) total energy versus volume for (*a*) MnB, (*b*) FeB and (*c*) CoB compounds, using GGA.

The static equilibrium properties are obtained from these curves, which are fitted using the Murnaghan equation of state [86]. The calculated ground state energy and equilibrium lattice

constants for MnB, FeB and CoB are listed in Tables 4.2, 4.3 and 4.4 along with their bulk modulus, pressure derivative in comparison with experimental and other theoretical reports. From these tables, it is seen that the calculated results of the lattice constants are in the same order of magnitude as experimental results. However, we can see that the cell constants were underestimated even in GGA calculations when compared with experimental results. Previous calculations on many transition metal monoborides clearly indicated that cell constants were usually underestimated with standard DFT method, even when GGA is applied [83]. It is seen that the calculated bulk moduli are consistent with other theoretical investigations.

Table 4.2 Calculated spin-polarization (SP) and non-spin-polarization (NSP) values of total energy, lattice parameters, bulk modulus and its first pressure derivative obtained at equilibrium volume of MnB using both LSDA and GGA compared to experimental and other theoretical works.

	***a* (Å)**	***b* (Å)**	***c* (Å)**	***B* (GPa)**	***B'***	***E* (eV)**
LDA	5.344	2.813	4.064	354	4.058	-128570.533
LSDA	5.347	2.933	3.986	291	4.804	-128570.774
GGA (NSP)	5.480	2.854	4.111	312	3.924	-128824.071
GGA (SP)	5.456	2.981	4.108	260	4.097	-128824.826
PAW	5.5384[a]	2.8428[a]	4.0913[a]	307[a]	-	-
ASW (LDF)	-	-	-	260[b]	-	-
Exp.	5.560[c]	2.977[c]	4.145[c]	-	-	-
	5.5600[d]	2.9770[d]	4.1514[d]	-	-	-
	5.5604[e]	2.9759[e]	4.1465[e]	-	-	-

[a] Ref. [87].

[b] Ref. [11].

[c] Ref. [11] and reference therein.

[d] Ref. [7].

[e] Ref. [88].

Table 4.3 Calculated spin-polarization (SP) and non-spin-polarization (NSP) values of total energy, lattice parameters, bulk modulus and its first derivative obtained at equilibrium volume of FeB using both LSDA and GGA compared to experimental and other theoretical works.

	***a* (Å)**	***b* (Å)**	***c* (Å)**	***B* (GPa)**	***B'***	***E* (eV)**
LDA	5.170	3.024	3.809	359	4.120	-140982.868
LSDA	5.283	2.927	3.892	344	4.267	-140983.110
GGA (NSP)	5.214	3.101	3.880	318	3.833	-141247.856
GGA (SP)	5.383	2.953	4.004	291	4.403	-141248.324
ASW (LDF)	-	-	-	250[a]	-	-
Exp.	5.495[b]	2.946[b]	4.053[b]	-	-	-
	5.495[c]	2.946[c]	4.053[c]	-	-	-
	5.506[d]	2.952[d]	4.081[d]	-	-	-

[a] Ref. [11],[b] Ref. [89], [c] Ref. [69],[d] Ref. [11] and reference therein.

Table 4.4 Calculated spin-polarization (SP) and non-spin-polarization (NSP) values of total energy, lattice parameters, bulk modulus and its first derivative obtained at equilibrium volume of CoB using both LSDA and GGA compared to experimental and other theoretical works.

	***a* (Å)**	***b* (Å)**	***c* (Å)**	***B* (GPa)**	***B'***	***E* (eV)**
LDA	5.264	3.007	3.730	349	4.227	-154106.486
LSDA	5.202	3.012	3.762	350	4.266	-154106.549
GGA (NSP)	5.231	3.060	3.877	312	3.649	-154383.191
GGA (SP)	5.204	3.062	3.892	310	3.926	-154383.198
ASW (LDF)	-	-	-	340[a]	-	-
Exp.	5.254[b]	3.314[b]	3.956[b]	-	-	-
	5.253[c]	3.043[c]	3.956[c]	-	-	-

[a] Ref. [11],[b] Ref. [69],[c] Ref. [11] and reference therein**.**

The stability toward magnetism is given by comparing the non-magnetic (NM) and magnetic (M) total energy values calculated at theoretical equilibrium volume. The calculated total energy difference ($\Delta E = E_{NM} - E_M$) between the nonmagnetic and magnetic states in the GGA approximation are 0.76 eV, 0.47eV and 0.01eV for MnB, FeB and CoB respectively. It is seen from the calculated energy difference between the nonmagnetic and magnetic states that MnB and FeB are more stable in the ferromagnetic state. However, the energy difference is nearly zero for CoB compound, thus magnetism could not exist in this compound in agreement with the experimental findings showing that CoB is not magnetic. Generally, if the system is non-magnetic, the energy calculated with spin-polarization should be the same as for the non-spin-polarization case, and the resulting magnetic moment will be 0. The lowest energy for MnB and FeB compounds is obtained from spin polarization GGA calculations.

4.1.4 Magnetic moment and mean-field analysis of nonmagnetic configurations

The understanding of the magnetic properties of transition metals and their alloys is one of the chief aims of the theory of itinerant magnetism. The spin-polarization calculations directly gives the magnetic moment, which is the difference between the total numbers of spin-up and spin-down electrons and corresponds to the saturated magnetic moment, μ_{sat}, at T=0. The ground states of both Fe- and Co-based phases behave as strong ferromagnetic with a magnetic moment 2.217μ_B [82], 1.656μ_B [83] respectively, while Mn-based phase is antiferromagnetic [83]. FeB and MnB show the ferromagnetic behavior [19], while CoB shows the diamagnetic behavior [19]. Table 4.5 shows the calculated magnetic moment for the transition metal and boron atoms in MnB, FeB and CoB compounds. The calculated total magnetic moment (for MnB and FeB) or per atom (for Mn and Fe atoms) within local spin-density approximation (LSDA) and generalized gradient approximation (GGA) approaches give rather different values. We can see that LSDA predicts smaller magnetic moments than GGA. The calculated TM (TM=Mn, Fe, Co) magnetic moments

in MnB, FeB and CoB compounds obtained from GGA are 1.81 μ_B, 1.18 μ_B and 0 μ_B, respectively. The calculated values of magnetic moment per atom for Mn and Fe atoms obtained from GGA agree well with the experimental results obtained by R.M. Bozorth [90] which show that the manganese in MnB carries a higher magnetic moment ($1.83\mu_B$) than iron in FeB does ($1.12\mu_B$), which leads to a shift in the Slater-Pauling curve. However, the total magnetic moment of MnB obtained from LSDA calculations is much closer to experimental results obtained by H. Zhu and al [18]. This has small effect on magnetic energy but no significant difference in band structures for both LSDA and GGA.

Table 4.5 Calculated magnetic moments of the mono-borides TM-B (TM= Mn, Fe, Co) using both GGA and LSDA together with experimental and other theoretical results.

		MnB		**FeB**		**CoB**	
		μ_{Mn}	μ_{Total}	μ_{Fe}	μ_{Total}	μ_{Co}	μ_{Total}
Our calculations	LSDA	1.409	5.900	1.061	4.224	0	0
	GGA	1.814	7.467	1.184	4.615	0	0
Other works	ASW (LDF)	2.00[a]	-	1.25[a]	-	0[a]	-
	LSDA	1.857[b]	7.196[b]	-	-	-	-
	GGA	1.985[b]	7.644[b]	-	-	-	-
	Exp.	1.83[c]	-	1.12[c]	-	0[c]	-
		-	5.84[d]	-	-	-	-

[a] Ref. [11].

[b] Ref. [91], FP-LAPW method using experimental lattice parameters.

[c] Ref. [11], and reference therein.

[d] Ref. [18].

The ferromagnetic behavior is dominated by TM–TM bonds and any gain of the covalent TM–B energy is accomplished by the loss of exchange energy of TM–TM bonds. P. Mohn and al.

[11] reported that the bonding mechanism is responsible for the fact that the magnetic moment of manganese in MnB is higher than that of iron in FeB. The Co and B atoms in CoB compound have no magnetic moment in agreement with diamagnetic behavior of CoB observed experimentally by Cadeville et al.[19].

The instability of the nonmagnetic state of the 3*d* transition metal monoborides with respect to formation of a ferromagnetic structure can be studied within the Stoner theory of band ferromagnetism [92], which is a mean-field approach. According to the Stoner model, the magnetic phase appears when the gain in the exchange energy is larger than the loss in kinetic energy, and the condition of the existence of magnetism could be evaluate by the Stoner criterion:

$$N(E_F) \times I \rangle 1 \qquad (4.1)$$

Where $N(E_F)$ is the non-spin-polarized partial density of states of transition metal atom at Fermi energy and I is the exchange-correlation integral calculated by Janak [93]. Table 4.6 shows the stability of the TM-B mono-borides according to Stoner model. The stoner criterion is fulfilled for MnB and FeB compounds but not for CoB compound due to the low density of states at the Fermi level (~ 0.88 state/eV). The stoner criterion is not able to predict the stability of a phase. However, the Stoner criterion used here may give us some hints on the magnetic ground state of our compounds. The magnetic behavior of MnB and FeB compounds and a non-magnetic behavior of CoB compound are consistent with the Stoner criterion.

Table 4.6 The stability of the TM-B mono-borides according to Stoner model.

	$N(E_F)$ (eV)	I (eV)	$N(E_F) \times I$
Mn	8.51	0.41	3.49
Fe	5.85	0.46	2.71
Co	0.88	0.49	0.43

4.1.5 Spin polarization and pressure effects on the structural properties

We have calculated the relative change of volume and bulk modulus between the magnetic and nonmagnetic state (Eq. 4.2) using LSDA and GGA in order to show the dependence of the magnetic moment on the equilibrium volume and bulk modulus.

$$\frac{\Delta X}{X} = \frac{X_M - X_{NM}}{X_M}, X = V, B \tag{4.2}$$

Where X_M is the calculated volume and bulk modulus in the magnetic state, X_{NM} is the calculated volume and bulk modulus in the nonmagnetic state.

Figure 4.3 shows the calculated percent relative change of volume *V* between the NM and FM states using GGA and LSDA. The GGA equilibrium volume for MnB in the NM and FM states are 64.29 Å and 66.84 Å respectively, while the GGA equilibrium volume for FeB in the NM and FM states are 62.73 Å and 63.65 Å respectively. It can be seen that the relative change of volume (between NM and FM states) increases from CoB to MnB due to the increasing in the magnetic moment. The GGA equilibrium volume for CoB in the NM and FM states are 62.07 and 62.02, respectively, which shows a nearly zero volume expansion in the FM state due to its nonmagnetic behavior.

The calculated percentage expansions in volume were range from 0 to 2.5% for LSDA and from 0 to 4 % for GGA. The magnitude of the magnetic moment is strongly related to the volume. Thus the values of equilibrium volume obtained in the magnetic case are larger than NM case. A possible origin of this dependence is the magneto-volume effect [94]. Because the Pauli Exclusion Principle operates for parallel spins the electron kinetic energy of the spin-polarized state is higher, and volume expansion relaxes the kinetic energy. Consequently the magnetic (high-spin) state has a larger volume than the non-magnetic (low-spin) state [95].

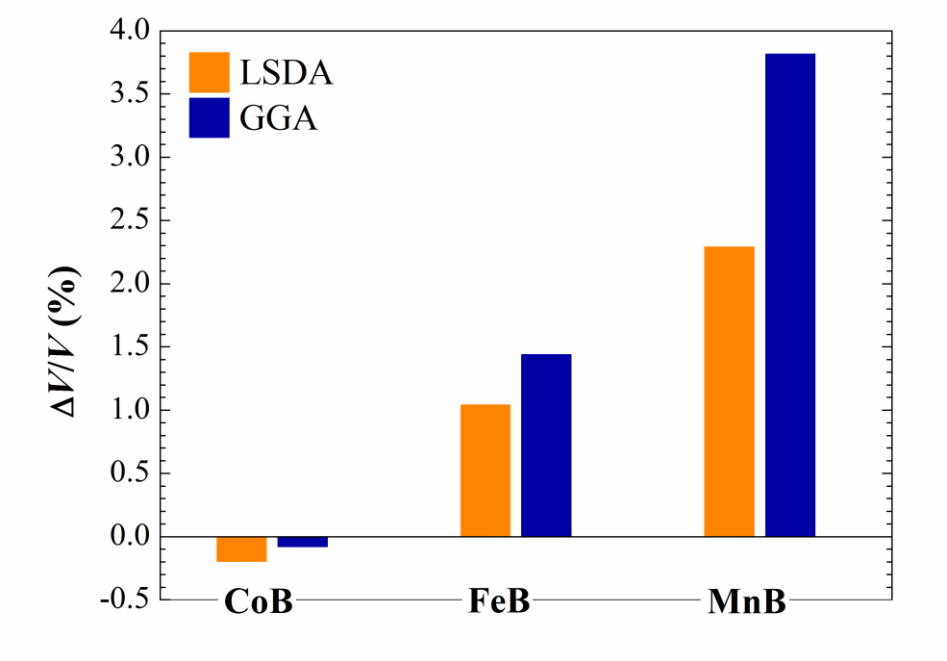

Figure 4.3 The calculated percent relative change of volume *V* using GGA and LSDA.

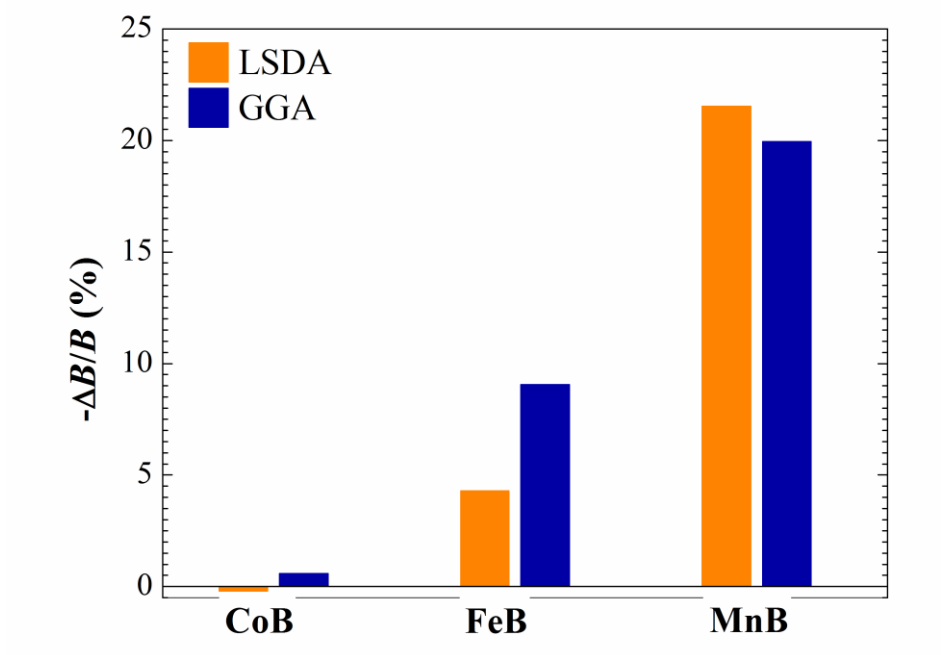

Figure 4.4 The calculated percent relative change of bulk modulus *B* using GGA and LSDA.

However, the bulk modulus decreases from CoB to MnB, also due to the increasing in the magnetic moment (see Fig. 4.4). The bulk modulus decreased from 0 to 22% for LSDA and from 0 to 20 % for GGA. In the NM state the bulk modulus B is systematically larger than magnetic

state. The low value of bulk modulus in magnetic case points to a larger compressibility. This means that the system is "softer" when it is magnetically ordered and "harder" when it is not. The spin-polarization calculations are important to obtain the correct ground state properties of MnB and FeB ferromagnetic compounds. The calculated cell volume V as a function of pressure using GGA is presented in Fig. 4.5. It is easy to observe that the cell volume V decreases with the pressure increasing. In this paper, all conversions between volume and pressure are based on the Murnaghan equation of state [86]:

$$P = \frac{B_0}{B'}\left[\left(\frac{V_0}{V}\right)^{B'} - 1\right] \tag{4.3}$$

Where V_0 and B_0 are the volume and the bulk modulus at zero pressure, B' is the bulk modulus pressure derivative. Fig. 4.6 shows the pressure dependence of the magnetic moment for TMB (TM=Mn, Fe, Co) compounds using GGA. It is easy to observe that the magnetic moment decreases with the pressure increasing for both MnB and FeB, and it becomes zero at a pressure around 450 and 700 GPa for MnB and FeB, respectively.

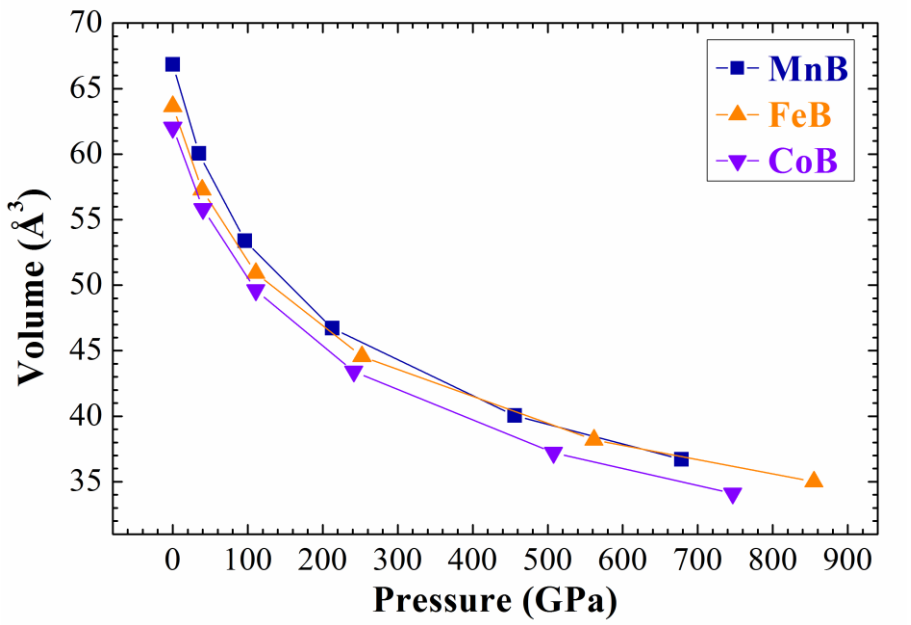

Figure 4.5 Cell volume V as a function of pressure for MnB, FeB, and CoB using spin-polarized GGA calculation.

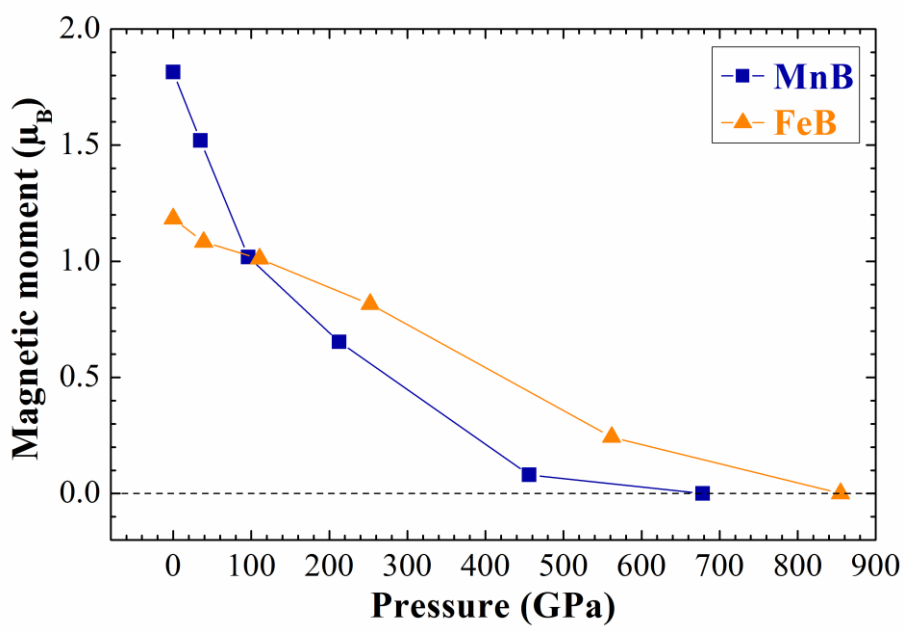

Figure 4.6 Magnetic moment versus pressure for MnB and FeB using spin-polarized GGA calculation.

4.1.6 Band structures and densities of states

Both NSP and SP band structures for MnB compound are shown in Fig. 4.7 using only GGA. We showed only this compound because all other TM-B iso-structures compounds show the same features. The calculated LSDA and GGA electronic band structures and densities of states look the same. From Fig. 4.7, we can see that MnB compound exhibit a metallic behavior and the valence band generated in the K_y direction (X-S, R-U) are broad, while those in the K_z (Z-Γ, Y-T) and K_x (Γ-X, S-Y, T-R, U-Z) directions are narrower. This indicates that the principal bonding interactions lie along the *y* direction in the crystal, those in other directions being more limited [96]. The *c* direction in reference [96] is the *b* direction in our work. We can obtain that by simply using the conversation relationship between *Pbnm* and *Pnma*. Both the continuous zigzag chains of B atoms and chains of metal atoms lie in the *b* direction of the crystal. Clearly indicate that the B-B bonding chains are very important in the chemical stability of TM-B compounds. The conduction bands are less well characterized than the valence bands but it is clear that they are also somewhat broad in the *y* direction and are in agreement with the known metallic nature of the compounds [97].

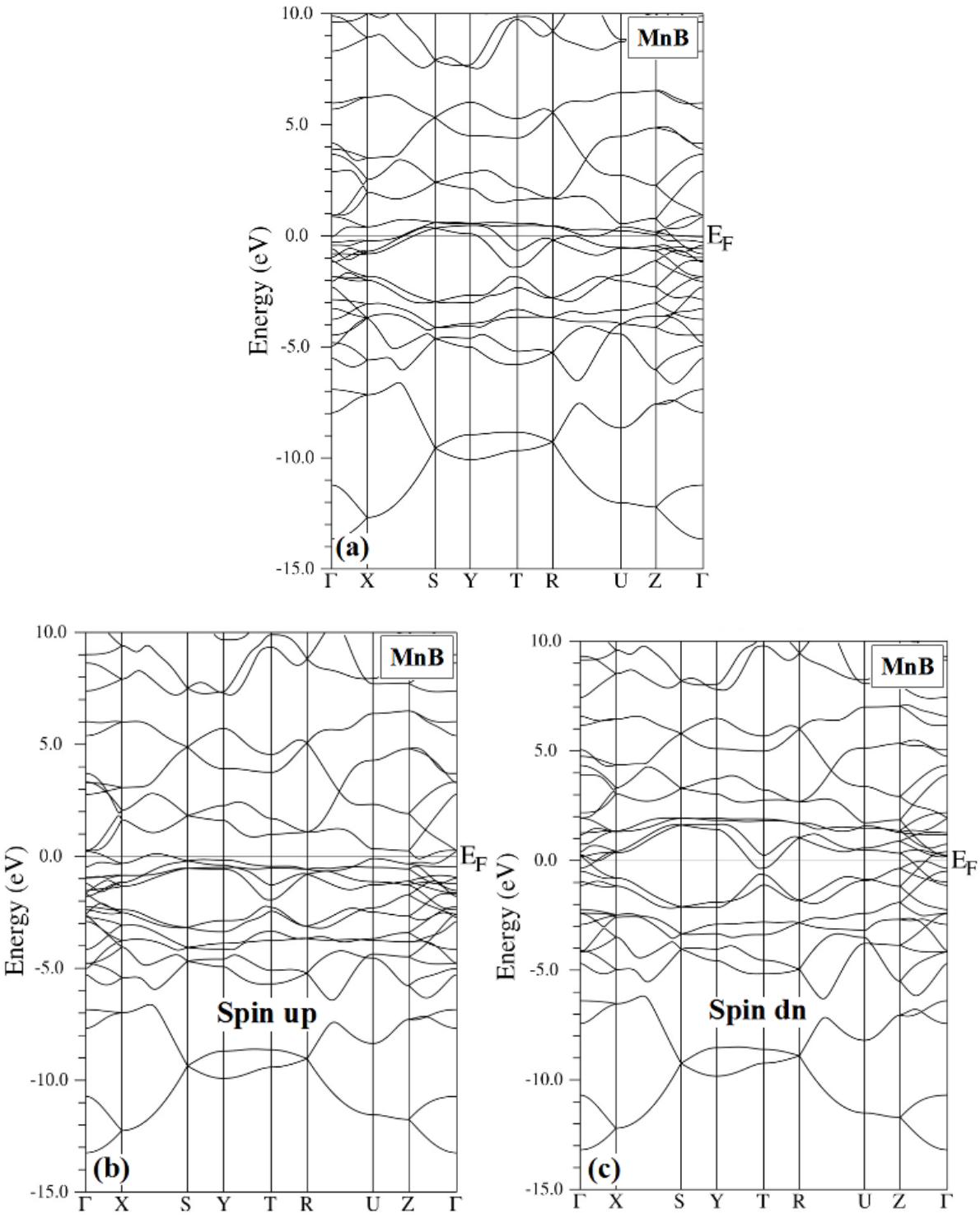

Figure 4.7 The calculated GGA band structures for MnB compound, with (*a*) Non-spin-polarization (NSP), and with Spin-polarization (SP), (*b*) for spin up and (*c*) for spin down.

The electronic structure is discussed by showing both NSP and SP electron densities of states (DOS) calculated using the equilibrium lattice parameters. Fig. 4.8 shows the calculated total

and partial DOS for MnB, FeB, and CoB using GGA. From this figure, it is clearly seen that the B-*s* and B-*p* states in all compounds are located well below the Fermi energy. B-*s* bonding peak is at about -11eV. The overlapping at about -3eV indicates the covalent bonds between B-*p* and TM-*d* states. However the predominant overlap is between B-*s* and B-*p* states at about -7 eV below the Fermi energy indicates the covalent bonds between B atoms.

The energy range from -13 eV to -6.4 eV, TM-*s*, TM-*p*, B-*s* and B-*p* bands dominates the TDOS. The energy band above -6.4 eV is mainly composed by *d* bands of TM atoms. At the Fermi level, the calculated TDOS is predominated by TM-*d* electrons due to the metallic character which is the most obvious feature of TM-B compounds. Both MnB and FeB compounds have a sharp peak at the Fermi level in NSP-DOS which is a sign of magnetic instability (*i.e*, the compounds will be more stable in magnetic state).

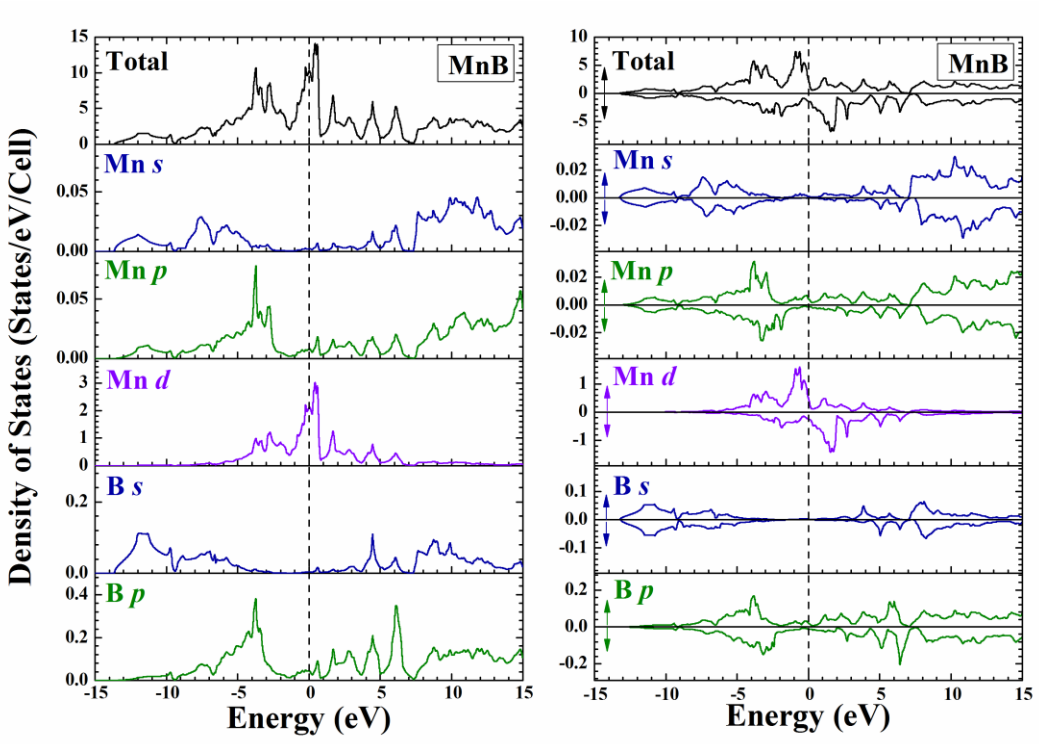

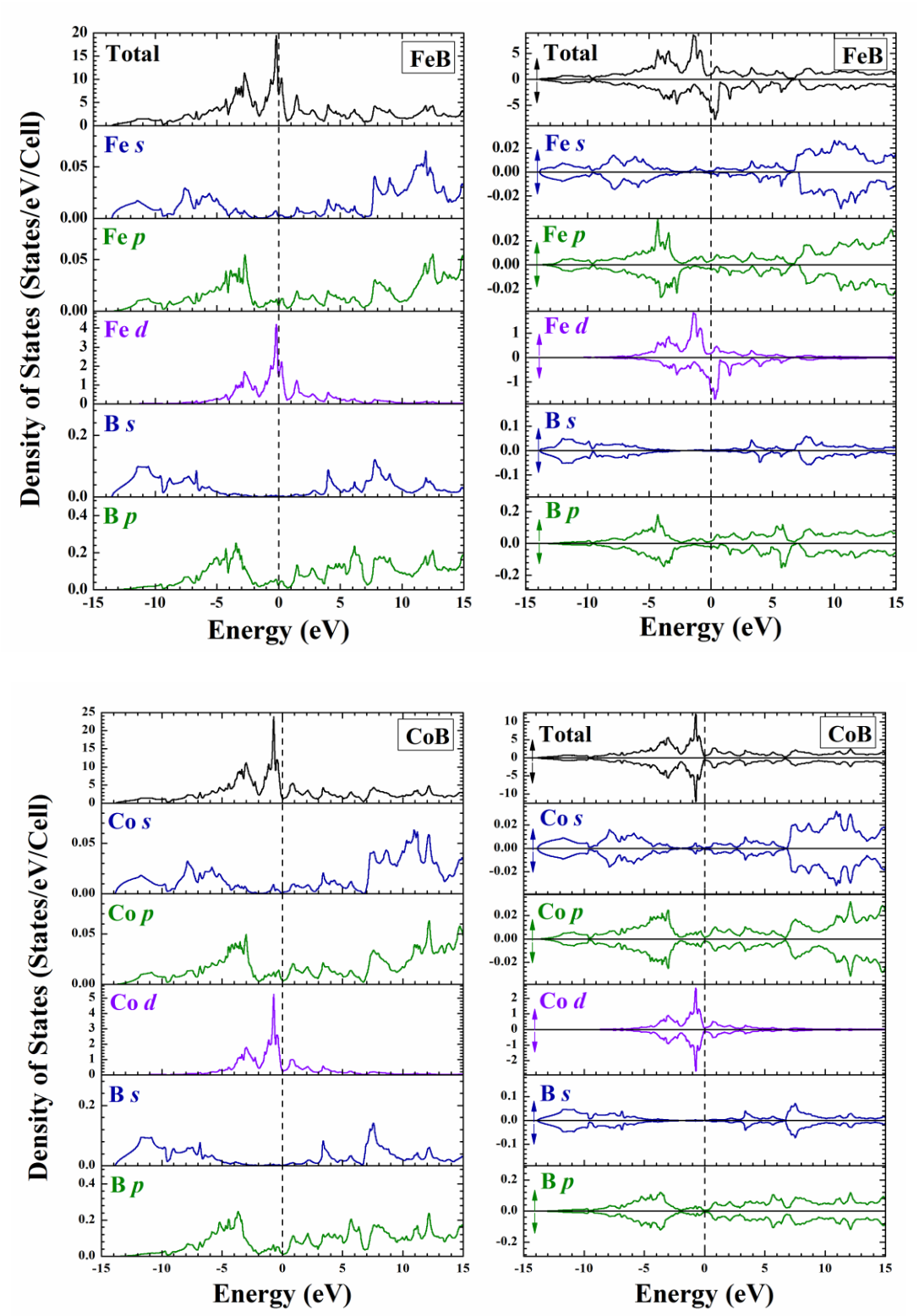

Figure 4.8 The calculated total and partial DOS for MnB, FeB and CoB, respectively, using GGA. (left panel) with Non-spin- polarization (NSP), and (right panel) with Spin-polarization. Dashed line represents the Fermi level.

Spin-polarization results from a nearly rigid band shift between the majority spins (↑) to lower energy and minority spin (↓) to higher energy due to the gain of energy from exchange [98]. From SP DOS (right panels of Fig. 4.8) it can be seen that the energy shift between spin ↑ and spin ↓ population is significant for Mn- and Fe-*d* states, which results in large magnetic moment values. In contrast, this shift is not observable for Co *d* states, and consequently a not significant magnetic moment is obtained.

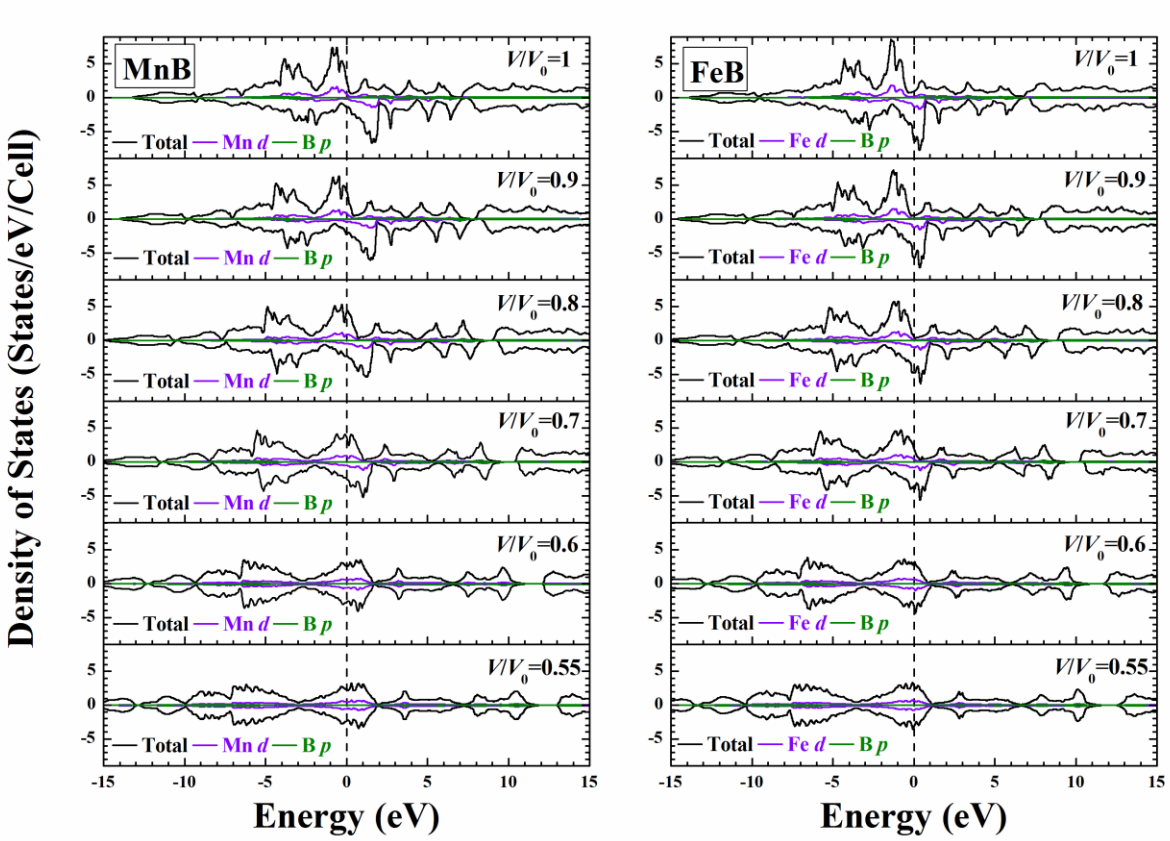

Figure 4.9 Total density of states of MnB and FeB at different pressures using spin-polarized GGA calculation. Dashed line represents the Fermi level.

The total and partial DOS for these compounds, at ambient and under compression, are shown in Fig. 4.9. From this figure, it can be stated that MnB and FeB total density of states at the Fermi level is predominantly due to the *d* electrons both at ambient and under high pressure. The main peak of *d* states for majority and minority spins are located below and above the Fermi level

respectively, and under compression, they start to move towards the Fermi level. However the lower energy part below -1.7 eV of the majority spins of *d* states starts to move reverse the trend. At approximately $V/V_0 = 0.6$, the TDOS in upper and lower half panels becomes like mirror due to the low magnetic moment under compression.

4.1.7 Conclusions

Spin polarization and pressure effects on the structural and electronic properties have been studied using both LSDA and GGA within the framework of density-functional theory (DFT). The calculated lattice constants, magnetic moment, bulk modulus and its pressure derivative were found to be in very good agreement with experimental and other theoretical results. Spin-polarization calculations show that MnB and FeB borides carry magnetic moment. The non-spin-polarization results show that the non-magnetic state is unstable for MnB and FeB compounds, but a stable non-magnetic phase for CoB compound, which is discussed in the framework of the well-known Stoner criterion. The important conclusions arrived from our calculations are:

- For both ferromagnetic compounds MnB and FeB, the magnetic states are more stable than the nonmagnetic states.
- Cell volume and magnetic moment decrease with pressure increasing.
- The change in volume between the magnetic and non-magnetic case follows an increasing variation for all compounds studied. However, the change in bulk modulus follows a decreasing variation for all compounds studied.
- Significant differences in volume and in bulk modulus were found between the magnetic and non-magnetic case reached 4%, 22% respectively.
- It is clearly seen that the density of states of MnB and FeB ferromagnetic compounds are significantly modified under high pressures. The exchange splitting decreases with

increasing pressure, at approximately $V/V_0 = 0.6$, the exchange disappears in ferromagnetic compounds causes mirror in upper and lower half panels.

- Spin polarization and pressure play crucially important role in the determining the electronic and structural properties.

4.2 Structural, magnetic and electronic properties of the 3*d* transition metal semi-borides TM_2B (TM= Mn, Fe, Co)

4.2.1 Introduction

The transition metal semiborides of the form TM_2B (TM=Mn, Fe and Co) form a class of essentially intermetallic compounds (Wyckoff 1963) [99]. All known transition metal semiborides crystallize in the tetragonal $A1_2Cu$ type structure with the space group 14/mcm (140). The unit cell contains four molecular units. The boron atoms find their next boron neighbours only in adjacent layers of the A type; they therefore form parallel strings, running through the crystal. Because of the large distance between the single boron atoms, any boron-boron interaction can be expected to be very small (P. Mohn 1988) [100].

Cadeville and Meyer (1962) [101] and Cadeville (1965) [19] describe the magnetic properties of the TM_2B compounds and their pseudo-binary alloys. Investigation into Fe_2B was done by Murphy and Hershkowitz (1973) [102] who confirm the earlier results. Only Fe_2B and Co_2B show a spontaneous magnetisation; Mn_2B compound is paramagnetic. For Mn_2B, Cadeville and Meyer (1962) [101] described a pronounced minimum in the temperature dependence of the susceptibility at 350 K. A more recent investigation into TM_2B was done by C.T. Zhou and al. (2009) [83] who showed that the spin polarized calculations results reveal that the ground state of Mn_2B is anti-ferromagnetic; Fe_2B and Co_2B are ferromagnetic. The calculated magnetic moment is 1.962 μ_B/Fe and 1.182 μ_B /Co for Fe_2B and Co_2B, respectively.

Both compounds Fe_2B and Co_2B behave as strong ferromagnets with a constant number of spin-up d electrons. Replacing iron by cobalt causes the additional *d* electron to occupy states in the spin-down band, thus reducing the magnetic moment on the transition-metal site by almost 1 μ_B from 1.84 μ_B for iron in Fe_2B to 0.88 μ_B for cobalt in Co_2B [100]. C.T. Zhou and al. [83] explained the complete annihilation of local magnetic moment of Ni in Ni_2B is mainly caused by the strong covalent TM–B bonds, and which reduce the exchange energy of TM–TM bonds greatly. The elongated electron density contours clearly reveal the strong covalent TM–B bonds and B–B bonds. In contrast to previous work [100], B-B interactions are very weak if not negligible because of the isolated positions of the boron atoms. On the other hand, even at the interstitial regions of TM_2B crystals, the calculated electron density values are still greater than 0.1 e/Å^3. It can be interpreted as the metallic bonds among TM metal atoms[83].

The thermodynamic parameters of TM_2B, including cohesive energy and formation enthalpy, are calculated and compared using first principal calculations [83]. Cohesive energy and formation enthalpy of these compounds all have negative values, which indicate that they are stable thermodynamic structures. Co_2B is less stable than the other compounds because it has the largest formation enthalpy value.

The mechanical properties, bond hardness and thermodynamic parameters of TM_2B compounds are calculated and discussed based on first principles calculations [103]. The results imply that the studied TM_2B compounds are mechanically stable. The hardness of TM–B and B–B bonds is calculated using a semi-empirical hardness theory. The hardness of B–B bonds for most TM_2B compounds is greatly larger than TM–B bonds.

The aim of this chapter is to investigate the structural and electronic properties for TM_2B (Mn, Fe and Co) compounds in both spin polarization and non-spin polarization calculations in order to show the effects of spin polarization on the structural and electronic properties.

4.2.2 Calculations method

Our calculations of structural and electronic properties of TM_2B compounds were carried out using the self-consistent full potential linearized augmented plane wave (FPLAPW) method [5] implemented in the Wien2k code [36] within the density functional theory (DFT). The Perdew–Burke–Ernzerhof generalized gradient approximation (GGA) [7, 8] and the local-spin-density approximation (LSDA) [6] were used for the exchange-correlation correction. The muffin-tin sphere radii were 2.1, 1.9 and 1.9 for Mn, Fe and Co respectively; 1.6 for B atom in MnB, FeB and CoB respectively. The convergence of the basis set was controlled by a cut off parameter $R_{mt} \times K_{max} = 8$ where R_{mt} is the smallest of the MT sphere radii and K_{max} is the largest reciprocal lattice vector used in the plane wave expansion. The cutoff energy, which defines the separation of valence and core states, was chosen as −6 Ry. The energy convergence was chosen as 0.0001Ry during self-consistency cycles. For the Brillouin zone (BZ) integration, 1500 k-points in the full BZ was used to construct the charge density in each self-consistency step.

4.2.3 Structural properties and magnetic stability

The transition metal semiborides TM_2B (TM=Mn, Fe and Co) crystallize in the tetragonal $A1_2Cu$ type structure with the space group 14/mcm (No. 140). The unit cell contains four molecular units (see Fig. 4.10). The position of atoms in TM_2B compounds were optimized and finally their positions were listed in the Table 4.7.

At the first step, we calculated the total energy versus volume for each compound with spin-polarization and without spin-polarization using LSDA. Figure 4.11 shows the SP and NSP total energy versus volume for (*a*) Mn_2B, (*b*) Fe_2B and (*c*) Co_2B compounds. It can be seen that the ferromagnetic state of Fe_2B and Co_2B is preferred at the calculated equilibrium volume to the nonmagnetic state.

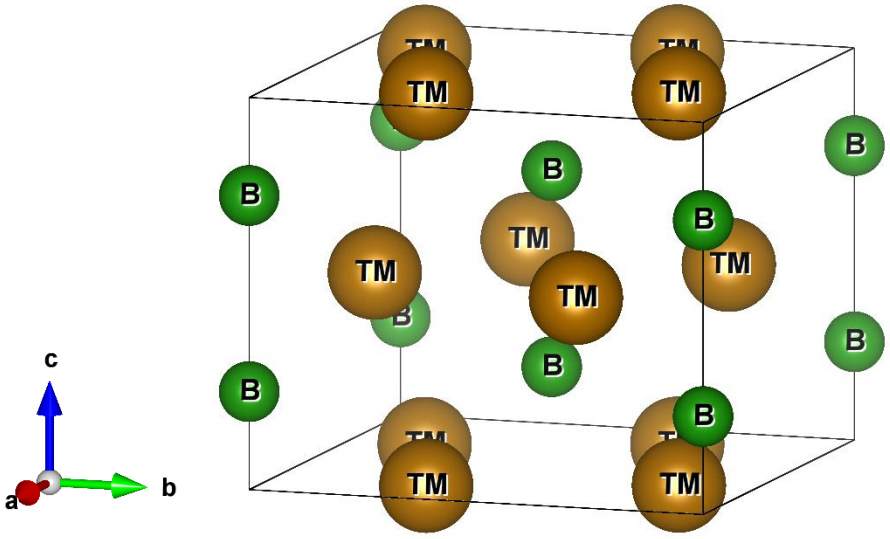

Figure 4.10 Crystal structure of TM_2B (TM= Mn, Fe and Co) borides

Table 4.7 Optimized atomic positions of TM_2B compounds using SP GGA approximation

Mn_2B				**Fe_2B**				**`Co_2B**			
Mn	0.159	0.659	0.000	**Fe**	0.166	0.666	0.000	**Co**	0.168	0.668	0.000
B	0.00	0.00	0.25	**B**	0.00	0.00	0.25	**B**	0.00	0.00	0.25

On the contrary, the energy difference between the ferromagnetic and nonmagnetic states in Mn_2B compound at equilibrium volume is zero, thus magnetism could not exist in this compound in agreement with experimental finding was done by Cadeville (1965) [19]. The calculated total energy difference ($\Delta E = E_{NM} - E_M$) between the nonmagnetic and magnetic states using LSDA are 0.00 eV, 0.26 eV and 0.16 eV for Mn_2B, Fe_2B and Co_2B respectively.

Tables 4.8-4.10 show the calculated SP and NSP values of total energy, lattice parameters, bulk modulus and its first pressure derivative obtained at equilibrium volume of TM_2B compounds using both LSDA and GGA compared to experimental and other theoretical works.

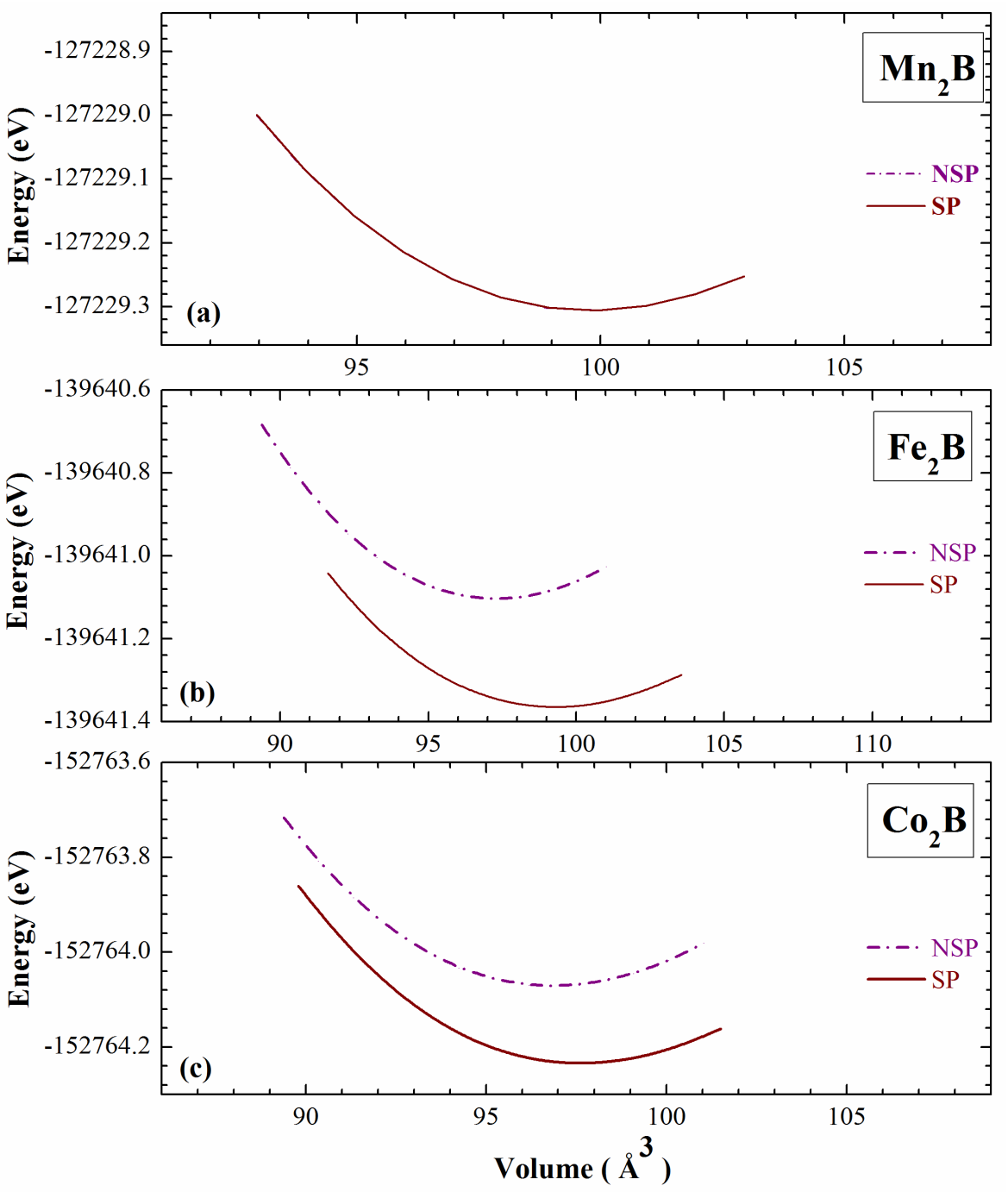

Figure 4.11 Spin polarization (SP) and non-spin polarization (NSP) total energy versus volume for (*a*) Mn_2B, (*b*) Fe_2B and (*c*) Co_2B compounds, using LSDA.

Table 4.8 Calculated spin-polarization (SP) and non-spin-polarization (NSP) values of total energy, lattice parameters, bulk modulus and its first pressure derivative obtained at equilibrium volume of Mn_2B using both LSDA and GGA compared to experimental and other theoretical works.

	***a* (Å)**	***c* (Å)**	***B* (GPa)**	***B'***	***E* (eV)**
LDA	4.961	4.055	366	4.310	-127228.353
LSDA	4.961	4.055	367	4.308	-127228.352
GGA (NSP)	5.059	4.111	322	3.932	-127469.763
GGA (SP)	5.068	4.109	324	4.276	-127469.571
PWE	5.0962[a]	4.1511[a]	301.44[a]	-	-
Exp.	5.149[b]	4.209[b]	-	-	-
	5.148[c]	4.208[c]	-	-	-

[a] Ref. [83],

[b] Ref. [104],

[c] Ref. [100] and reference therein.

Table 4.9 Calculated spin-polarization (SP) and non-spin-polarization (NSP) values of total energy, lattice parameters, bulk modulus and its first pressure derivative obtained at equilibrium volume of Fe_2B using both LSDA and GGA compared to experimental and other theoretical works.

	***a* (Å)**	***c* (Å)**	***B* (GPa)**	***B'***	***E* (eV)**
LDA	4.842	4.147	363	4.312	-139640.058
LSDA	4.924	4.094	301	4.753	-139640.320
GGA (NSP)	4.933	4.225	316	3.971	-139892.955
GGA (SP)	5.058	4.219	229	4.107	-139893.651
PWE	5.017[a]	4.217[a]	249.73[a]	-	-
Exp.	5.110[b]	4.240[b]	-	-	-
	5.109[c]	4.249[c]	-	-	-

[a] Ref. [83],

[b] Ref. [104],

[c] Ref. [100] and reference therein.

Table 4.10 Calculated spin-polarization (SP) and non-spin-polarization (NSP) values of total energy, lattice parameters, bulk modulus and its first pressure derivative obtained at equilibrium volume of Co_2B using both LSDA and GGA compared to experimental and other theoretical works.

	***a* (Å)**	***c* (Å)**	***B* (GPa)**	***B'***	***E* (eV)**
LDA	4.846	4.123	343	4.431	-152762.928
LSDA	4.849	4.151	328	4.671	-152763.091
GGA (NSP)	4.969	4.153	296	4.159	-153027.597
GGA (SP)	4.962	4.247	261	4.389	-153027.913
PWE	4.9858[a]	4.2822[a]	247.26[a]	-	-
Exp.	5.015[b]	4.22[b]	-	-	-
	5.016[c]	4.220[c]	-	-	-

[a] Ref. [83].

[b] Ref. [104].

[c] Ref. [100], and reference therein.

First of all, we may note that both LSDA and GGA results of the lattice constants and bulk modulus are in the same order of magnitude as theoretical and experimental results. However, we can see that the cell constants for all compounds were underestimated when compared with experimental results, except for Co_2B compound in the SP GGA calculations. The calculated bulk moduli of Fe_2B and Co_2B using SP GGA; Mn_2B using NSP GGA agree well with PWE calculations compared to other methods used.

4.2.4 Magnetic moment and mean-field analysis of nonmagnetic configurations

The ground states of both Fe- and Co-based phases behave as strong ferromagnetic with a magnetic moment $2.217\mu_B$ [82], $1.656\mu_B$ [83] respectively, while Mn-based phase is antiferromagnetic [83]. Fe_2B and Co_2B show the ferromagnetic behavior, while Mn_2B shows the paramagnetic behavior [102] or antiferromagnetic behavior [83]. As can be seen, the magnetic

behavior of Mn_2B and Co_2B semi-borides are totally different from MnB and CoB monoborides. One should recognize that at different atomic environments (crystalline structures), different values of the moment are obtained. Thus, the major effect which prevails in the value of the magnetic moment is the nature of the *d-p* hybridization in the TMB and TM_2B bond which is related to the atomic environment (the number of the nearest neighbors), the TM-B distance has also an average effect. To be specific, the magnetic moment for pure bcc Fe at the equilibrium volume is 2.18 μ_B, but zero in the fcc and hcp phases. Table 4.11 shows the calculated magnetic moment for transition metals in Mn_2B, Fe_2B and Co_2B compounds using both GGA and LSDA together with experimental and other theoretical results.

Table 4.11 Calculated magnetic moment of the semi-borides TM_2B (TM= Mn, Fe, Co) using both GGA and LSDA together with experimental and other theoretical results.

		Mn_2B		**Fe_2B**		**Co_2B**	
		μ_{Mn}	μ_{Total}	μ_{Fe}	μ_{Total}	μ_{Co}	μ_{Total}
Our calculations	LSDA	0.00	0.00	1.344	5.281	0.796	3.063
	GGA	0.00	0.00	1.916	7.378	1.100	4.195
Other works	ASW	-	-	1.84[a]	-	0.88[a]	-
	PWE	0.00[b]	-	1.962[b]	-	1.182[b]	-
	Exp.	-	-	1.91[c]	-	0.8[c]	-

[a] Ref. [100],[b] Ref. [83], [c] Ref. [101].

The GGA gives the closest agreement of the calculated moments for Fe atom in Fe_2B with experimental result, while LSDA gives the closest agreement of the calculated moments for Co atom in Co_2B with experimental result. The ferromagnetic state is dominated by TM–TM bonds and any gain of the covalent TM–B energy is accomplished by the loss of exchange energy of TM–TM bonds. The anti-ferromagnetic behavior of Mn_2B is highly dependent on the strong intra-band exchange interactions of metal's *d* orbits according to Hunt's rule [83].

The instability of the nonmagnetic state of the 3*d* transition metal semi-borides with respect to formation of a ferromagnetic structure can be studied within the Stoner theory of band ferromagnetism [92]. The condition of the existence of magnetism could be evaluate by the Stoner criterion (Eq. 4.1). Table 4.12 shows the stability of the TM_2B semi-borides according to Stoner model. All the compounds fulfil the Stoner criterion, even for Mn_2B non-magnetic compound. These results indicate that Fe_2B and Co_2B have a non-stable non-magnetic phases in agreement with the ferromagnetic behavior of these two compounds. However experimental results show that Mn_2B has a stable non-magnetic phase in contrast with Stoner model, this indicates that the Stoner model is limited.

Table 4.12 The stability of the TM_2B semi-borides according to Stoner model.

	$N(E_F)$ (eV)	I (eV)	$N(E_F) \times I$
Mn	3.10	0.41	1.27
Fe	8.91	0.46	4.10
Co	14.18	0.49	6.95

4.2.5 Spin polarization and pressure effects on the structural properties

As we have done before with the transition metal mono-borides, we have calculated the relative change of volume and bulk modulus between the magnetic and nonmagnetic state (Eq. 4.2) for TM_2B compounds using LSDA and GGA in order to show the dependence of the magnetic moment on the equilibrium volume and bulk modulus. It can be seen from Figs. 4.12 and 4.13 that as much as the relative change in volume increases as much as the relative change in bulk modulus decreases. The calculated percent relative change of volume V between the NM and FM states were: 0 %, 2 % and 0.8 % for Mn_2B, Fe_2B and Co_2B, respectively, for LSDA; and 0.2 %, 4.7 % and 1.9 % for Mn_2B, Fe_2B and Co_2B, respectively, for GGA. For Fe_2B and Co_2B, the expansion of volume in the magnetic state strongly related to the magnitude of the magnetic moment. Mn_2B

shows a nearly zero volume expansion in the magnetic state due to its nonmagnetic behavior.

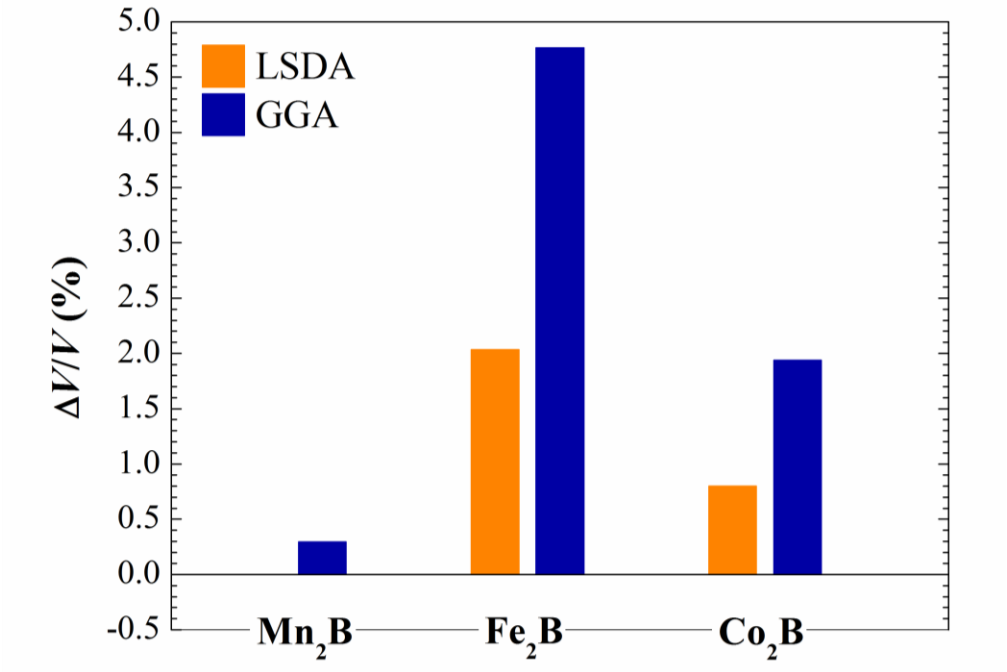

Figure 4.12 The calculated percent relative change of volume *V* using GGA and LSDA.

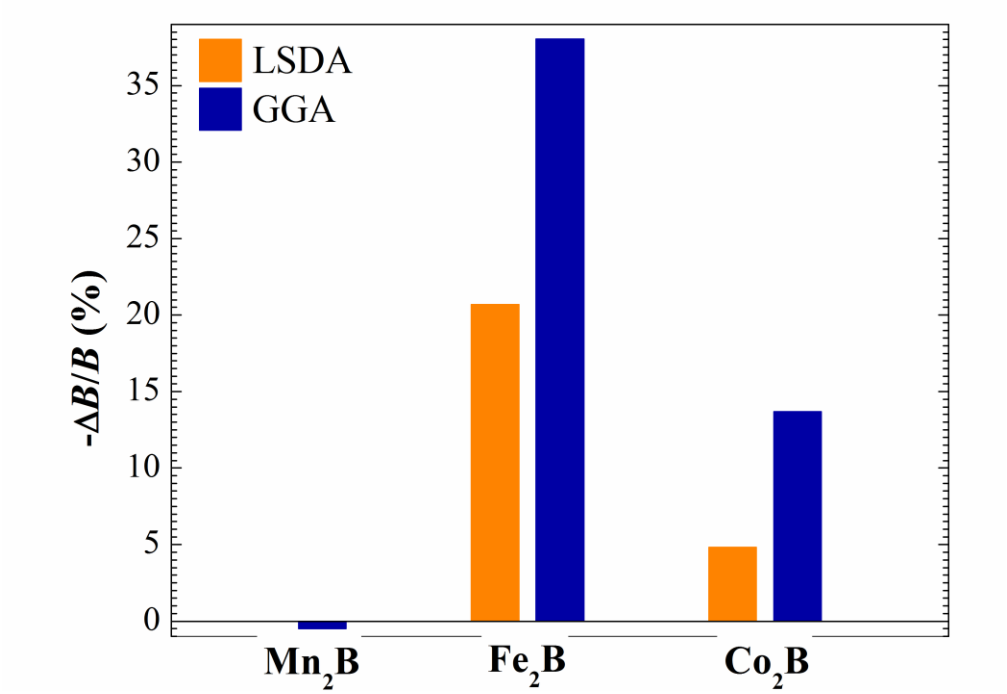

Figure 4.13 The calculated percent relative change of bulk modulus *B* using GGA and LSDA.

The calculated percent relative change of bulk modulus *B* between the NM and M states were: 0 %, 20 % and 4.8 % for Mn_2B, Fe_2B and Co_2B, respectively, for LSDA; and -0.4 %, 38 % and 13.7 % for Mn_2B, Fe_2B and Co_2B, respectively, for GGA. In the NM state the bulk modulus B is systematically larger than magnetic state. The high value of bulk modulus in non-magnetic state points to a lower compressibility. This means that the system is "softer" when it is magnetically ordered and "harder" when it is not. The spin-polarization calculations are important to obtain the correct ground state properties of Fe_2B and Co_2B ferromagnetic compounds. Figs. 4.14 and 4.15 show the calculated cell volume *V* and magnetic moment μ_B as a function of pressure using SP GGA. We can see from these figures, as the pressure increases, the volume and the magnetic moment decrease. The relationship between the pressure and the volume is based on the Murnaghan equation of state (Eq. 4.3). As can be seen in Fig. 4.14, the variation of the volumes as a function of pressure in TM_2B compounds are very similar to those of TMB compounds. However, for Fe_2B, a pressure of 600 GPa is sufficient to achieve a zero magnetic moment, while FeB needs a pressure of 854 GPa to achieve zero magnetic moment.

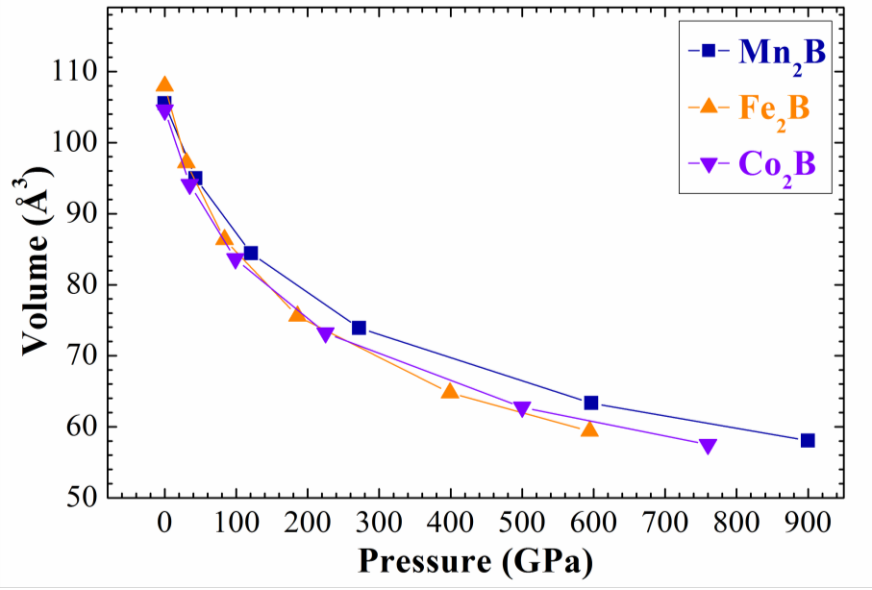

Figure 4.14 Cell volume *V* as a function of pressure for Mn_2B, Fe_2B, and Co_2B using spin-polarized GGA calculation.

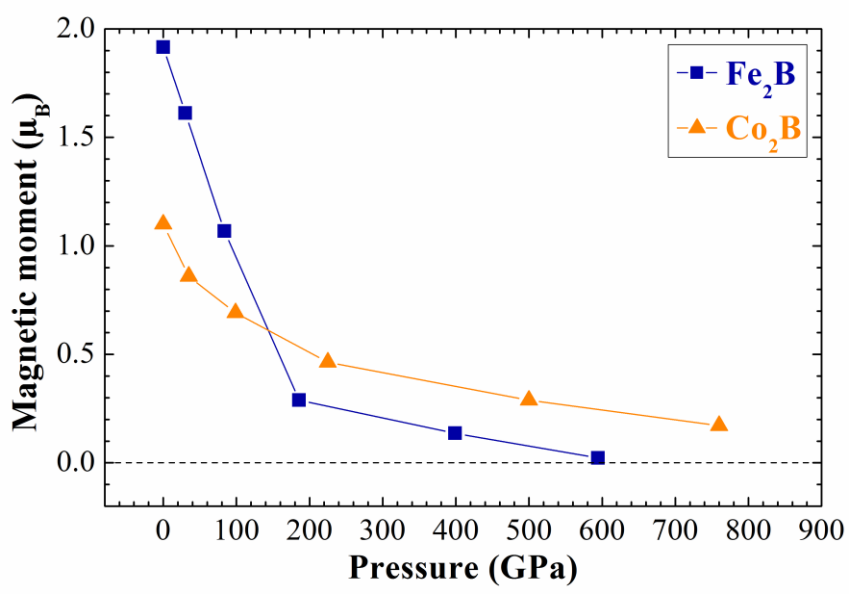

Figure 4.15 Magnetic moment versus pressure for Fe_2B, and Co_2B using spin-polarized GGA calculation.

4.2.6 Band structures and densities of states

Bans structure calculations of TM_2B compounds have been performed using both LSDA and GGA. Fig. 4.16 shows both SP and NSP band dispersion curves plotted at equilibrium volume for Co_2B compound using LSDA. The compound shows metallic nature and the *d* bands of Co dominate near the Fermi level as we will see in the density of states plots.

The total and partial density of states, calculated using LDA and LSDA are shown in Figs. 4.17-4.19 for Mn_2B, Fe_2B and Co_2B, respectively. In all figures, the most obvious feature of TM_2B compounds is the metallic character at Fermi level. In NSP-DOS and at the Fermi level, both Fe_2B and Co_2B compounds have a sharp peak of 8.9 and 14.2 states/eV/cell, which is a sign of magnetic instability (*i.e*, the compounds will be more stable in magnetic state). The largest DOS value at Fermi level corresponds to Co_2B, which indicates that Co_2B is less stable than the other phases.

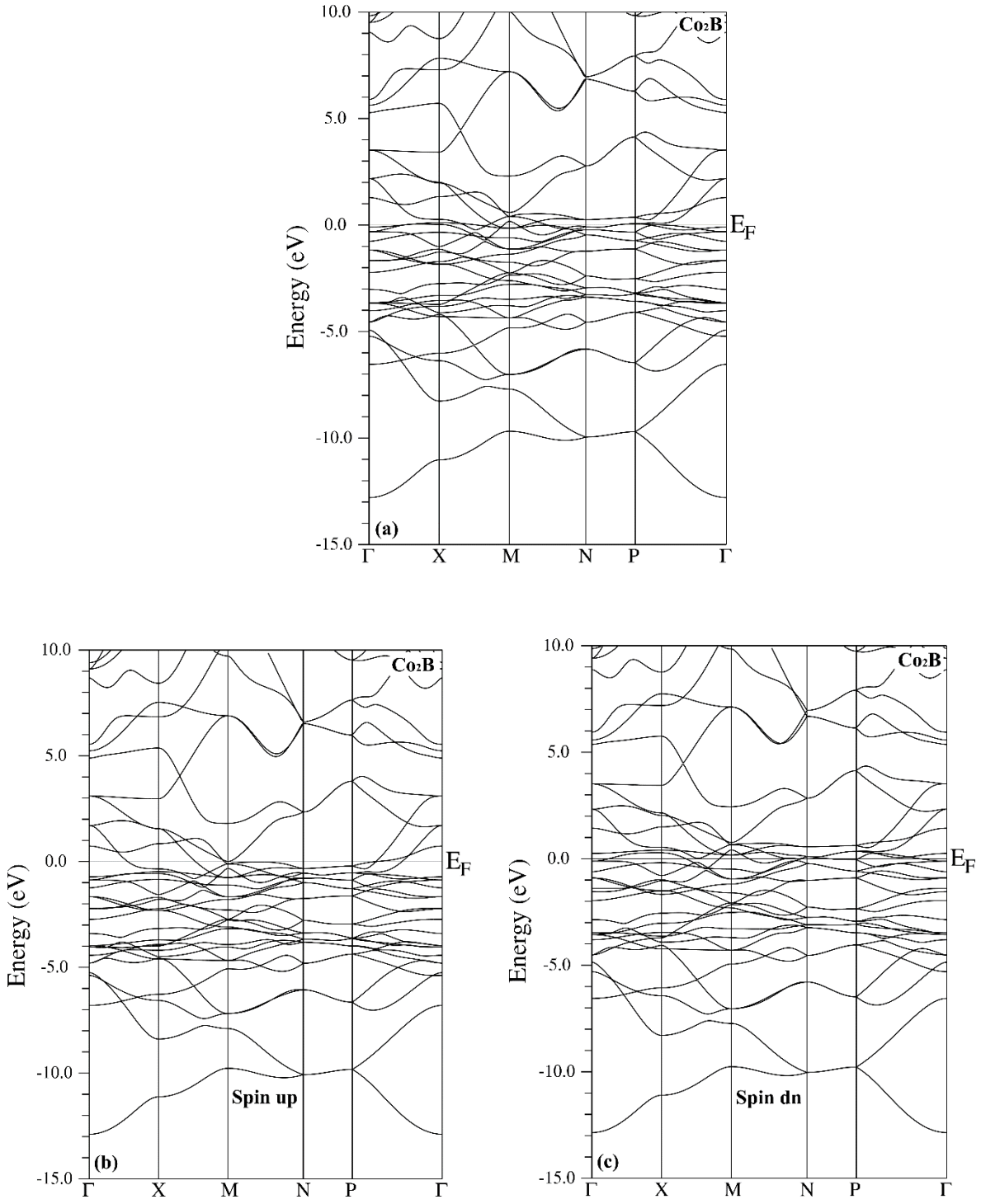

Figure 4.16 The calculated LSDA band structures for Co_2B compound, with (*a*) Non-spin-polarization (NSP), and with Spin-polarization (SP), (*b*) for spin up and (*c*) for spin down.

From Figs. 4.17-4.19 (left panel), it is clearly seen that the B-*s* and B-*p* states in all compounds are located well below the Fermi energy. B-*s* states lie from -12.7 to -1.6 eV with a

major peak at about -10 eV. B-*p* states extended from -12.2 to Fermi energy. Two main peaks are observed in the total density of states of TM_2B compounds P_1 and P_2. P_1 is located at -3.28 eV, -3.61eV and -3.57 eV for Mn_2B, Fe_2B and Co_2B, respectively, which is mainly caused by covalent bonding between B and the metal atom. P_2 is located above the Fermi level for Mn_2B and Fe_2B, and below the Fermi level for Co_2B. The peaks located at 0.53 eV, 0.30 eV and -0,038 eV for Mn_2B, Fe_2B and Co_2B, respectively, which is mainly caused by metallic bonding between TM atoms. The energy range from -12.7 eV to -8 eV, B-*s* bands dominates the TDOS. From -8.0 eV to -6.2 eV, it is mainly dominated by *p* bands of B atoms. The energy band above -6.2 eV is mainly composed by *d* bands of TM atoms.

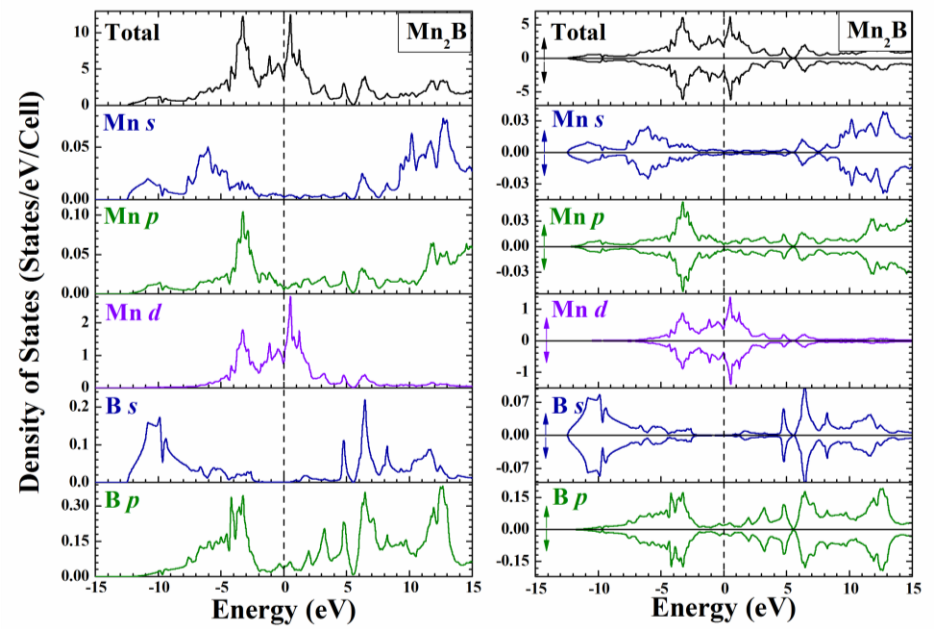

Figure 4.17 The calculated total and partial DOS for Mn_2B, using LSDA. (left panel) with Non-spin-polarization (NSP), and (right panel) with Spin-polarization. Dashed line represents the Fermi level.

From SP DOS (right panels of Figs. 4.17-4.19) it can be seen that the energy shift between spin ↑ and ↓ population is significant for Fe- and Co-*d* states, which results in large magnetic moment values. In contrast, this shift is not observable for Mn *d* states, and consequently a not significant magnetic moment is obtained.

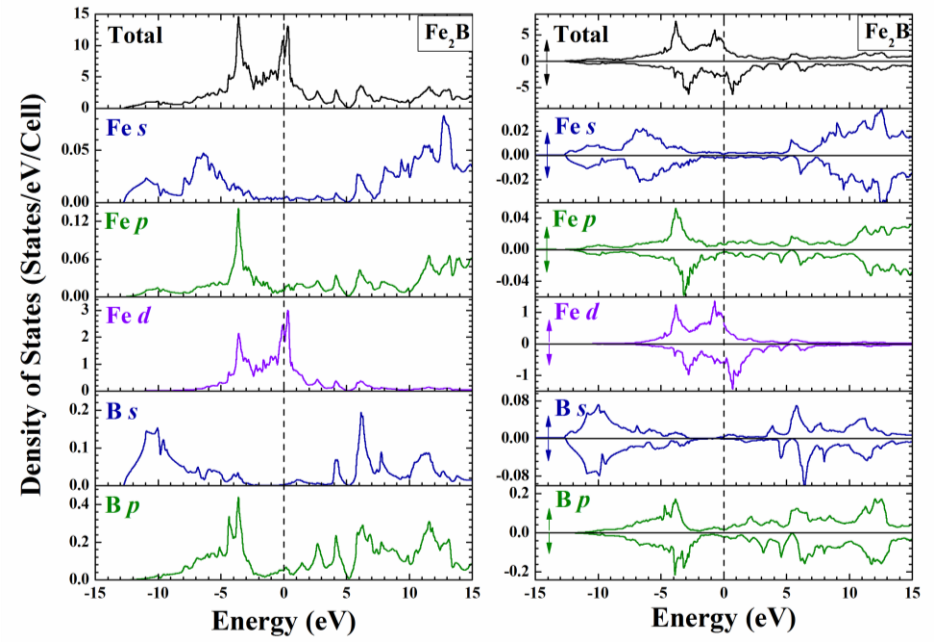

Figure 4.18 The calculated total and partial DOS for Fe_2B, using LSDA. (left panel) with Non-spin- polarization (NSP), and (right panel) with Spin-polarization. Dashed line represents the Fermi level.

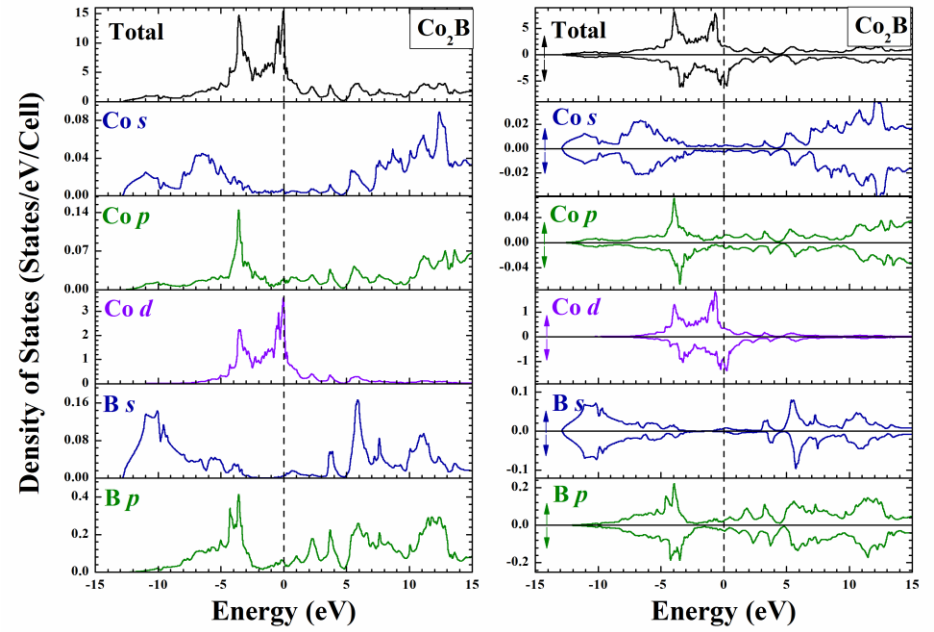

Figure 4.19 The calculated total and partial DOS for Co_2B, using LSDA. (left panel) with Non-spin- polarization (NSP), and (right panel) with Spin-polarization. Dashed line represents the Fermi level.

The density of states and its variation under pressure is computed for Fe_2B and Co_2B ferromagnetic compounds using GGA in order to look at possible changes occurring in the electronic structure under compression. From figure 4.20, it can be stated that Fe_2B and Co_2B total density of states around the Fermi level is predominantly due to the *d* electrons both at ambient and under high pressure. The two main peak P_1 and P_2 for majority spins are located below the Fermi level (P_1 has lower energy than P_2), and under compression, P_2 starts to move towards the Fermi level and P_1 moves in reverse. For minority spins, and under compression, the P_2 for Co_2B remains near the Fermi level not moving, while for Fe_2B moves towards the Fermi level, P_1 starts to move in reverse to the Fermi level for both Fe_2B and Co_2B compounds. At approximately $V/V_0 = 0.7$, the TDOS in upper and lower half panels becomes like mirror due to the low magnetic moment.

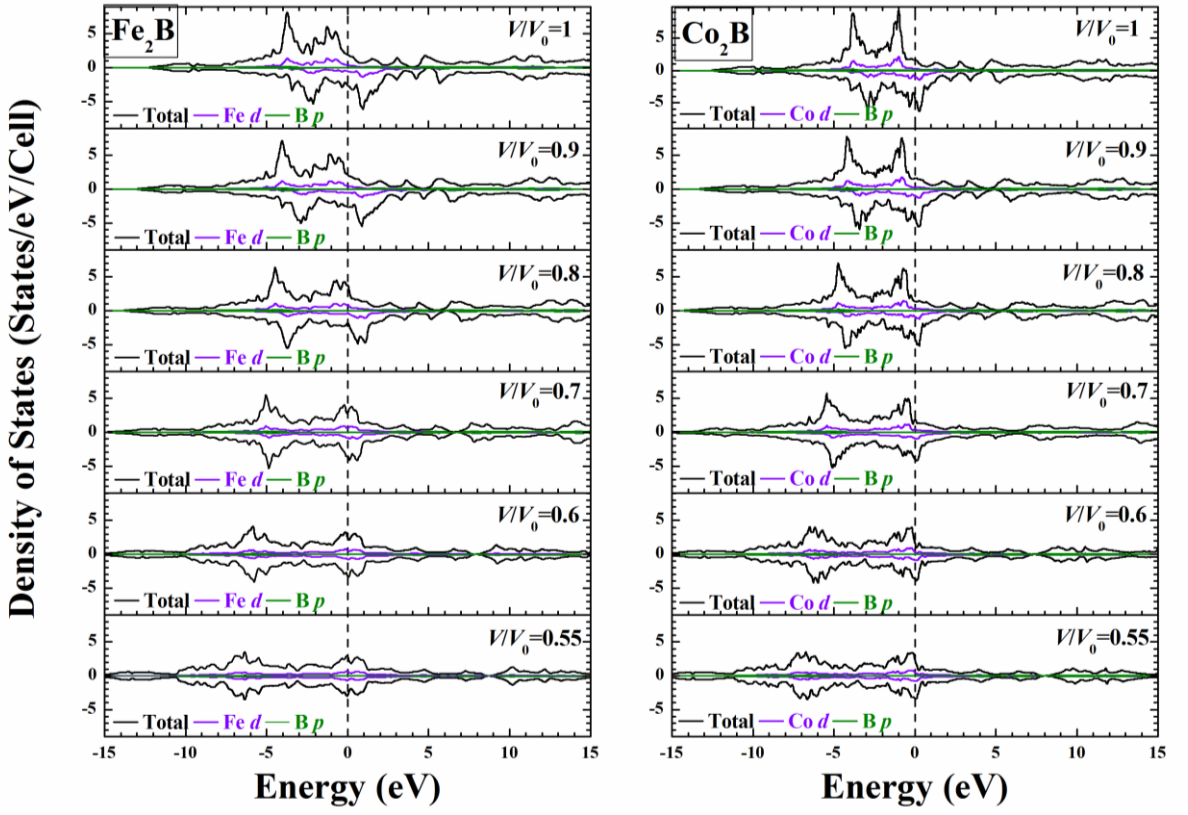

Figure 4.20 Total density of states of Fe_2B and Co_2B at different pressures using spin-polarized GGA calculation. Dashed line represents the Fermi level.

4.2.7 Conclusions

Spin polarization and pressure effects on the structural, magnetic and electronic properties of TM_2B (TM=Mn, Fe, Co) semi-borides have been studied using both LSDA and GGA. The calculated percent relative change of volume *V* between the NM and M states reaches 0.2 %, 4.7 % and 1.9 % for Mn_2B, Fe_2B and Co_2B, respectively, for GGA. The calculated percent relative change of bulk modulus *B* between the NM and M states reaches -0.4 %, 38 % and 13.7 % for Mn_2B, Fe_2B and Co_2B, respectively, for GGA. The magnetic behavior of TM_2B compounds was shown to be in agreement with the predictions of the Stoner theory for both Fe_2B and Co_2B ferromagnetic compounds. The cell volume and the magnetic moment decrease with pressure increasing. The two main peaks P_1 and P_2 for majority and minority spins of Fe_2B and Co_2B ferromagnetic compounds are significantly modified under high pressures. The exchange splitting decreases with increasing pressure, at approximately V/V_0 = 0.7, the exchange disappears in ferromagnetic compounds causes mirror in upper and lowers half panels. There is a significant change in volume and density of states under high pressure, and also when taking into account the spin polarization.

4.3 Structural, magnetic and electronic properties of the 3*d* transition metal mono-nitrides TM-N (TM= Mn, Fe, Co)

4.3.1 Introduction

Thin films of FeN have been synthesized and two possible crystal structures were reported [30-33]. One is the rocksalt (RS) structure with a lattice constant of a=4.57 Å, and by performing ^{57}Fe Mössbauer spectroscopy measurements, the authors suggested rocksalt FeN to be an antiferromagnet [30, 31]. The other structure is of a zinc-blend (ZB)-type with a lattice constant of a=4.33 Å and a micromagnetic character [32]. For CoN, there has been some discussion in the earlier literature about the crystal structure and both ZB and RS structures have been reported

depending on the synthesis method. Schmidt-Dumont and Kron [34] obtained rocksalt CoN with a lattice constant of 4.27 Å by decomposition of $Co(NH_2)_3$, while Taylor *et al.* [35] obtained zinc-blende CoN with a lattice constant of 4.28 Å by decomposing $[Co(NH_3)_6](N_3)_3$. The manganese mononitride MnN has been found in (fct-RS) -type structure i.e., a tetragonally distorted rocksalt structure [105].

From the available literature, a clear controversy exists between the studies carried out in the framework of density-functional theory. First-principles calculations in different structural phases of transition metal nitrides have indicated that FeN is more stable in a ferromagnetic FM rocksalt structure than nonmagnetic zinc-blende nitride [98, 106]. The same results were reported later on the stability of the FeN RS-type structure, but without complete agreement for the magnetic ordering [107, 108]. However, Lukashev and Lambrecht [109] have joined some others [27] in predicting a stable nonmagnetic ZB structure for FeN. The energy minimum for MnN and CoN is found to correspond to the ZB structure [27, 110, 111]. The results of first-principles calculations of electronic, structural and magnetic properties for the 3*d* mononitrides CoN, NiN and CuN, in different structures have indicated that CoN has no stable magnetic states, and the nonmagnetic ZB-type state is the ground state [112], which is consistent with experimental results [35, 113].

In this chapter, we will investigate the structural, magnetic and electronic properties of the 3*d* transition metals mono-nitrides TMN (TM=Mn, Fe, Co) with the NaCl-type structure in two cases non-spin-polarized (NSP) and spin-polarized (SP) calculations within GGA and LSDA. We will also study the energy difference between the ZB and RS structures for FeN using GGA + *U*. The parameter *U* has been varied for many values in order to understand the effects of electron correlations on the structural, magnetic and electronic properties.

4.3.2 Calculations method

Our first-principle calculations are performed in the framework of the density functional theory DFT [4, 40, 84, 85] which is implemented in the Wien2k code [36]. The self-consistent calculations were carried out using the full potential linearized augmented plane wave (FP-LAPW) method [5] . We have used the generalized gradient approximation (GGA) [7, 8] of Perdew–Burke–Ernzerh (PBE) and the local spin density approximation (LSDA) [6] for the exchange correlation energy. The plane wave cutoff is determined by $R_{mt}K_{max}$= 8.0 (where R_{mt} is the muffin-tin radius, and K_{max} is the maximum modulus for the reciprocal lattice vector). The choice of the muffin-tin (MT) sphere radii for TM atoms show small deference. We have adopted the values of 2.0. 2.0. 1.9 for Mn, Fe, and Co atoms respectively in the LSDA and the values of 2.1. 2.0. 1.9 in the GGA. We kept the same muffin-tin (MT) radii for N atom for all compounds studied in deferent approximations as 1.6. The separation energy of valence and core states (cut-off energy) was chosen as −8 Ry. The energy convergence was chosen as 0.0001Ry during self-consistency cycles. The special k-points in the full BZ were selected as 3000. We kept the same convergence parameters between spin-polarized and non-spin-polarized calculations for all compounds studied in order to show the dependence of the structural and electronic properties on spin-polarization.

4.3.3 Structural and magnetic properties

The NSP and SP calculations were performed in the rock-salt structure for all TMN (TM=Mn, Fe and Co) compounds. The space group of our compounds is $Fm\bar{3}m$. The unit cell contains four molecular units (see Fig. 4.21). The metal atom is located at the origin of the unit cell and the N atom is placed at (0.5, 0.5, 0.5).

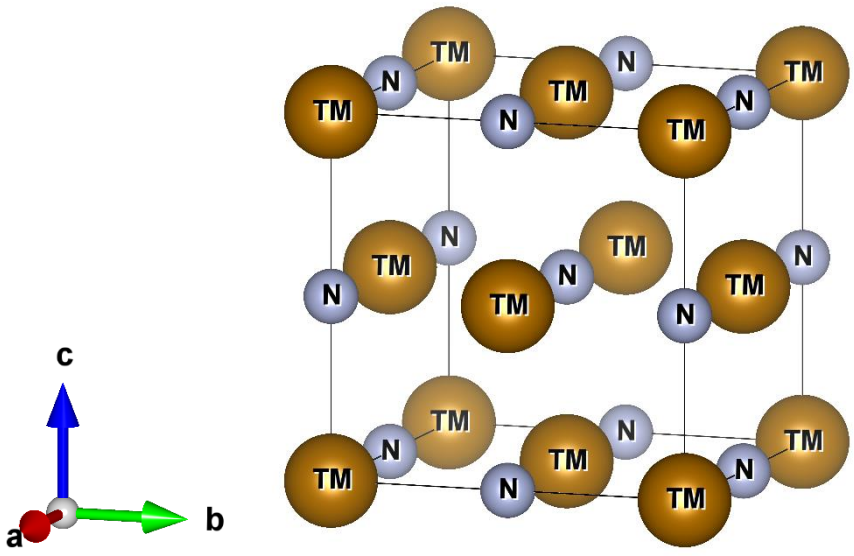

Figure 4.21 Crystal structure of TMN (TM= Mn, Fe and Co) nitrides

At the first step, we calculated the total energy versus volume for each TM-N compound with spin-polarization and without spin-polarization. Figure 5.22 shows the SP and NSP total energy versus volume for (*a*) MnN, (*b*) FeN and (*c*) CoN compounds, using GGA. It can be seen that the ferromagnetic state of MnN and FeN is preferred at the calculated equilibrium volume to the nonmagnetic state. However, the energy difference between the ferromagnetic and nonmagnetic states for CoN compound at equilibrium volume is zero due to the absent of the magnetic moment.

The calculated total energy, lattice parameter, bulk modulus and its first derivative for TMN compounds obtained at equilibrium volume are given in Tables 4.13-4.15 together with experimental and other theoretical investigations. The Murnaghan equation of state (Eq. 4.3) is used to obtain equilibrium lattice parameters, bulk modulus B, and its first derivative B'. The lattice constant is usually underestimated with respect to the experimental lattice constant by up to a few percent by the LDA while the GGA sometimes overestimates it. From Tables 4.13-4.15, we can see that even the GGA seems to underestimate the lattice constant. However, we should note that

the experimental lattice constant corresponds to that of a thin film, which may be influenced by the substrate and is not a true bulk value.

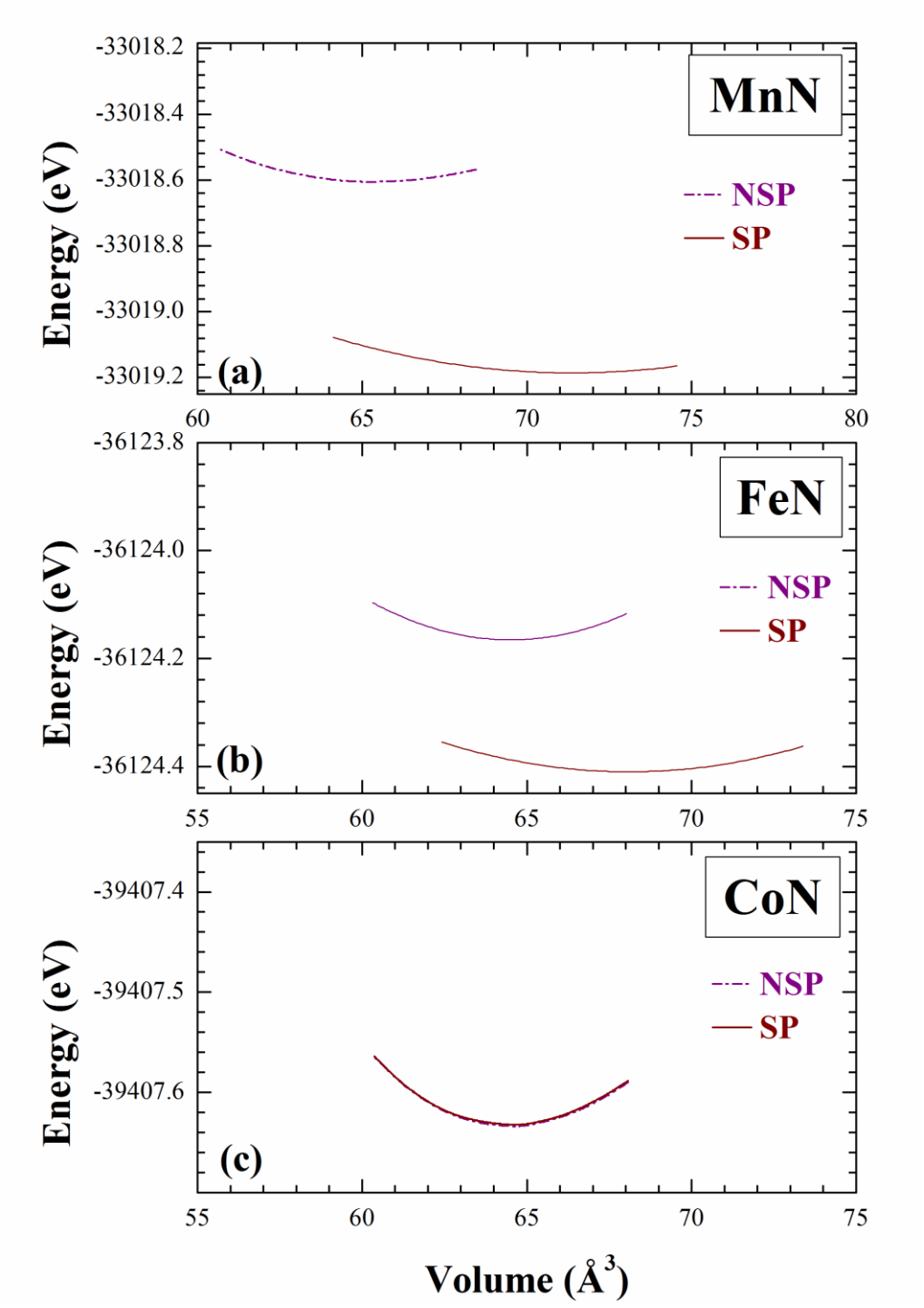

Figure 4.22 Spin polarization (SP) and non-spin polarization (NSP) total energy versus volume for (*a*) MnN, (*b*) FeN and (*c*) CoN compounds, using GGA.

Table 4.13 Calculated spin-polarized (SP) and non-spin-polarized (NSP) values of total energy, lattice parameter, bulk modulus and its first derivative obtained at equilibrium volume of MnN using both LSDA and GGA approximations compared to experimental and other theoretical works.

	***a* (Å)**	***B* (GPa)**	***B'***	***E* (eV)**
LDA	3.943	399.260	4.477	-32951.857
LSDA	4.005	315.751	5.940	-32952.132
GGA (NSP)	4.027	337.380	4.666	-33018.852
GGA (SP)	4.141	168.652	5.400	-33019.433
LMTO (FM)	4.02[a]	-	-	-
LMTO (AFM)	4.02[a]	-	-	-
PWP (LDA)`	3.95[b]	373[b]	-	-
Exp.	4.256[c]	-	-	-

[a] Ref. [111].

[b] Ref. [114].

[c] Ref. [28] lattice parameters data for the face centered tetragonal structure of the MnN compounds, c/a=0.984 ~ 1.

Table 4.14 Calculated spin-polarized (SP) and non-spin-polarized (NSP) values of total energy, lattice parameter, bulk modulus and its first derivative obtained at equilibrium volume of FeN using both LSDA and GGA approximations compared to experimental and other theoretical works.

	***a* (Å)**	***B* (GPa)**	***B'***	***E* (eV)**
LDA	3.926	390.638	4.632	-36054.461
LSDA	3.944	358.499	5.252	-36054.607
GGA (NSP)	4.007	310.963	5.851	-36124.435
GGA (SP)	4.076	159.297	5.073	-36124.683
ASA-GGA	3.967[a]	369[a]	4.6[a]	-
ASW (NSP)	4.027[b]	-	-	-
ASW (SP)	4.112[b]	-	-	-
TB-LMTO-ASA	4.196[c]	-	-	-
Exp.	4.572[d]	-	-	-

[a] Ref.[109]

[b] Ref. [115].

[c] Ref. [108].

[d] Ref. [30].

Table 4.15 Calculated spin-polarized (SP) and non-spin-polarized (NSP) values of total energy, lattice parameter, bulk modulus and its first derivative obtained at equilibrium volume of CoN using both LSDA and GGA approximations compared to experimental and other theoretical works.

	***a* (Å)**	***B* (GPa)**	***B'***	***E* (eV)**
LDA	3.924	361.814	5.128	-39334.950
LSDA	3.923	360.956	5.687	-39334.950
GGA (NSP)	4.009	303.239	5.235	-39407.929
GGA (SP)	4.009	302.749	4.906	-39407.927
ASA-GGA	3.9639[a]	352[a]	4.6[a]	-
ASW (NSP)	4.027[b]	-	-	-
ASW (SP)	4.112[b]	-	-	-
Exp.	4.2969[c]	-	-	-

[a] Ref. [109]

[b] Ref. [115].

[c] Ref.[113].

Turning now our attention to the bulk modulus, we can see from Tables 4.13-4.15 that the bulk modulus for all compounds are in the range of other calculated value. The spin polarized GGA is seen to decrease the bulk modulus compared to the other approximations. The softening is consistent with a weaker bonding. The decrease in bulk modulus between SP GGA and NSP GGA is of order 50% and 48% for MnN and FeN compounds respectively, whereas in the CoN compound is only of order 0.16%.

At equilibrium, the transition metal atom in CoN has zero magnetic moment, while those in the MnN and FeN possess a high magnetic moment. The calculated magnetic moments for transition metal atoms in MnN, FeN compounds using LSDA and GGA are presented in Table 4.16. It is easy to see that the calculated magnetic moments are in good agreement with previously reported magnetic moment values.

Table 4.16 Calculated magnetic moment of the mono-nitrides TM-N (TM= Mn, Fe, Co) using both GGA and LSDA together with other theoretical results.

	μ_{Mn}	μ_{Fe}
LSDA	2.27	1.25
GGA	2.80	2.23
Calc. (ASW)	3.32[a]	2.51[a]
Calc. (LMTO)	3.03[b]	2.15[b]

[a][115] , [b] Ref. [116].

Also we have investigated the possibility of occurrence of magnetic ordered states for each TM-N compounds according to the stoner condition of ferromagnetism (Eq. 4.1). Table 4.17 shows the stability of the TM-N mono-nitrides according to Stoner model. The stoner criterion is fulfilled for all the compounds studied even for CoN non-magnetic compound. Previous study on magetovolume effect of CoN proved that its theoretical equilibrium volume is the limit of apparition of magnetic polarization [115].

Table 4.17 The stability of the TM-N mono-nitrides according to Stoner model

Transition metal atoms	$N(E_F)$ **(eV)**	I **(eV)**	$N(E_F) \times I$
Mn	2.497	0.41	1.024
Fe	4.778	0.46	2.198
Co	2.058	0.49	1.008

4.3.4 Band structures and densities of states

The NSP and SP calculated band structure of FeN in certain symmetry directions is shown in Fig. 4.23 as an example. Using only GGA we plotted the band structures of FeN and the total density of states (DOS) curves of all the compounds studied in SP and NSP states, which are presented in Figs. 4.24-4.26 together with *s*, *p*, and *d* partial density of states.

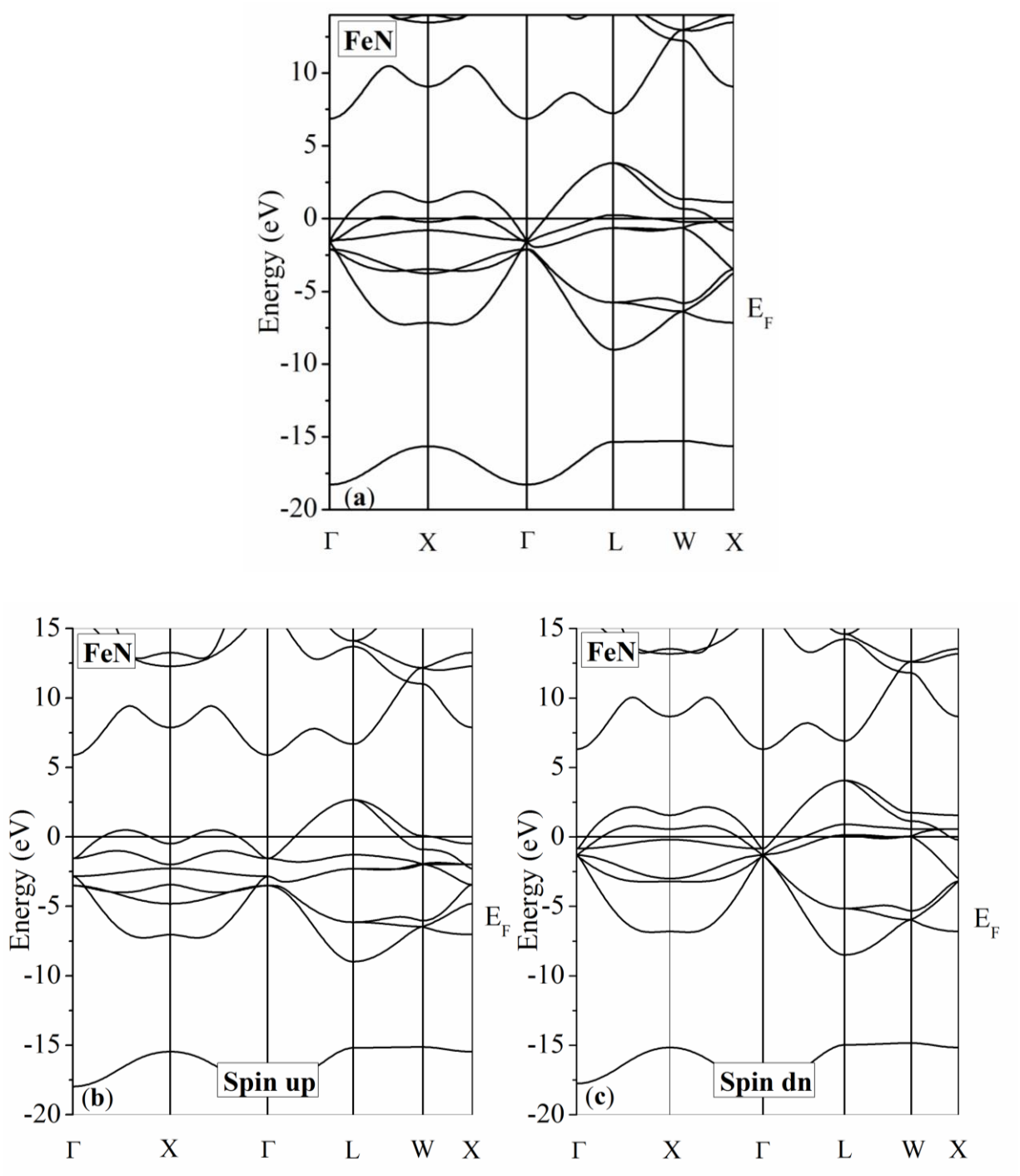

Figure 4.23 The calculated GGA band structures for FeN compound, with (*a*) Non-spin-polarization (NSP), and with Spin-polarization (SP), (*b*) for spin up and (*c*) for spin down.

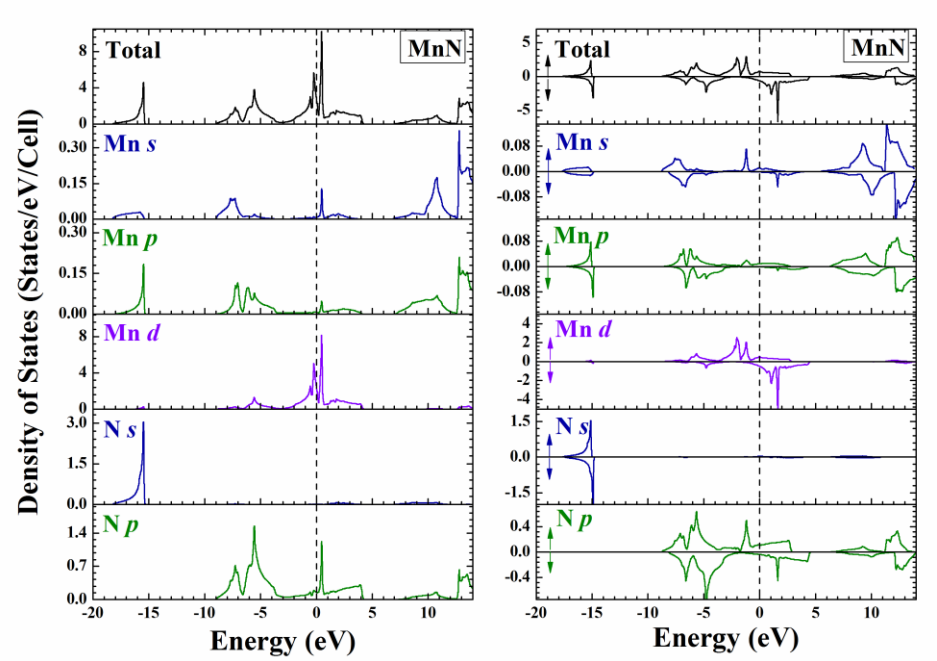

Figure 4.24 The calculated total and partial DOS for MnN, using GGA. (left panel) with Non-spin- polarization (NSP), and (right panel) with Spin-polarization. Dashed line represents the Fermi level.

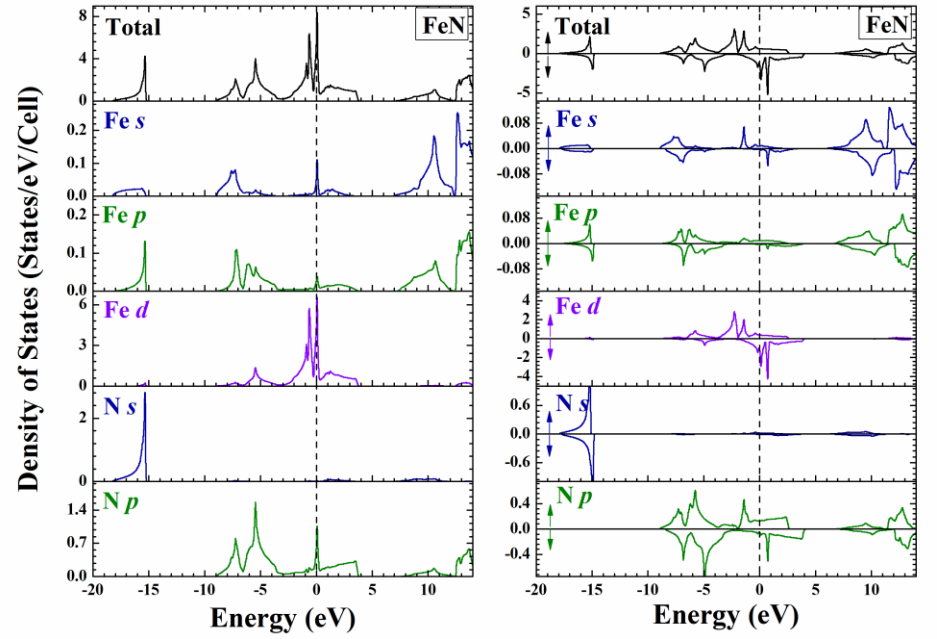

Figure 4.25 The calculated total and partial DOS for FeN, using GGA. (left panel) with Non-spin- polarization (NSP), and (right panel) with Spin-polarization. Dashed line represents the Fermi level.

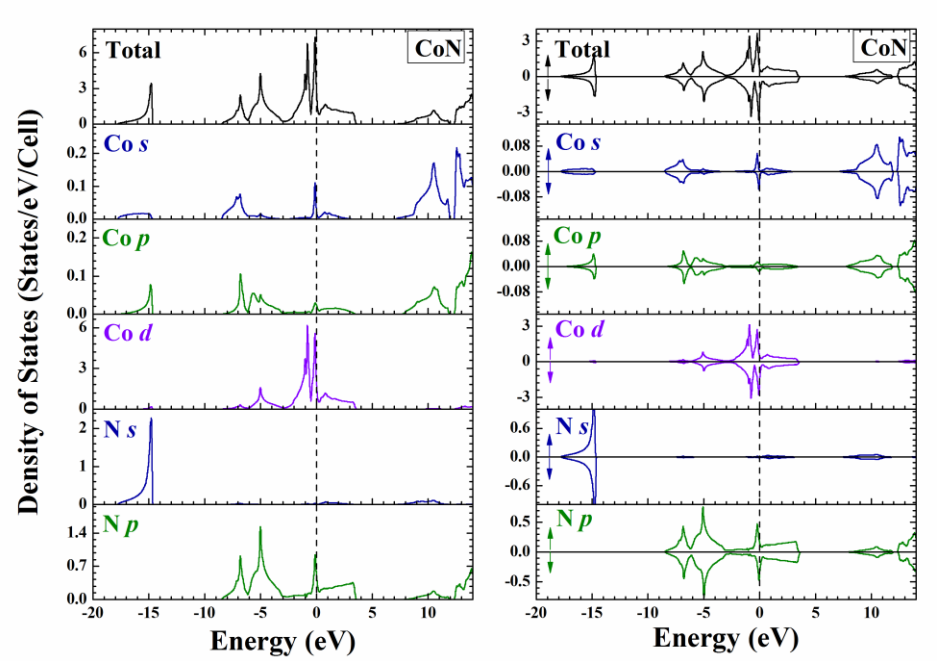

Figure 4.26 The calculated total and partial DOS for CoN, using GGA. (left panel) with Non-spin- polarization (NSP), and (right panel) with Spin-polarization. Dashed line represents the Fermi level.

As seen from these Figs. 4.24-4.26, the peak in the DOS near −15 eV is due to N 2*s* states. The region just above, which is separated by a significant gap from the lowest-lying energy N 2s states of the conduction band, from -8 eV to -3 eV, contains mostly hybridized *p* state of N atom. The energy range from -3 eV to Fermi level is dominated by the TM-*d* bands, which are responsible of the magnetic moment in the MnN and FeN compounds. At the Fermi level, the calculated TDOS is predominated by TM-*d* electrons due to the metallic character which is the most obvious feature of TMN compounds.

4.3.5 Effects of Hubbard U on the structural, magnetic and electronic properties for FeN compound.

We have varied the parameter U (U=U_{eff}) for many values in order to understand the effects of electron correlations on the structural, magnetic and electronic properties. First, we have studied the crystal structure preference for zinc-blende or rocksalt structures for FeN using GGA + U.

Table 4.18 Calculated FM and AFM values of lattice parameter, total energy, magnetic moment, bulk modulus and its first derivative obtained at equilibrium volume for FeN in RS structure within GGA+*U* for different values for *U*.

***U*(Ry)**	***a* (Å)**	***E* (eV)**	μ_{total}	μ_{Fe}	***B*(GPa)**	***B'***
0.0	4.0937	-36124.4024	2.49	2.33	134	3.39
0.0 (AFM-I)	4.0928	-36124.4168	0.00	2.22	195	4.60
0.1	4.186	-36123.277	3.48	3.24	199	4.06
0.2	4.2403	-36122.3787	4.02	3.64	193	5.38
0.2 (AFM-I)	4.2695	-36122.3301	0.00	3.66	183	4.22
0.3	4.293	-36121.712	4.44	3.96	187	4.97
0.4	4.329	-36121.170	4.77	4.17	201	3.81
0.5	4.347	-36120.707	4.89	4.27	208	4.08
0.6	4.354	-36120.264	4.99	4.37	212	4.64
0.7	4.361	-36119.876	4.99	4.42	218	3.83
0.8	4.365	-36119.539	5.00	4.48	218	4.84
0.9	4.371	-36119.217	4.99	4.53	219	3.47

Table 4.19 Calculated FM and AFM values of lattice parameter, total energy, magnetic moment, bulk modulus and its first derivative obtained at equilibrium volume for FeN in ZB structure within GGA+*U* for different values for *U*.

***U*(Ry)**	***a* (Å)**	***E*(eV)**	μ_{total}	μ_{Fe}	***B***	***B'***
0.0	4.2343	-36125.2202	0.00	0.00	282	4.85
0.0 (AFM-I)	4.2353	-36125.2216	0.00	0.00	283	3.61
0.1	4.242	-36123.658	0.00	0.00	271	4.86
0.2	4.5493	-36122.2111	4.00	3.36	142	4.26
0.2 (AFM-I)	4.5174	-36122.7753	0.00	3.47	158	3.48
0.3	4.599	-36121.471	4.34	3.76	142	4.06
0.4	4.632	-36120.778	4.56	3.95	147	3.14
0.5	4.656	-36120.157	4.76	4.09	145	4.72
0.6	4.694	-36119.906	4.91	4.33	150	4.52
0.7	4.709	-36119.469	4.99	4.42	151	4.80
0.8	4.719	-36119.118	4.99	4.49	165	3.73
0.9	4.726	-36118.716	4.99	4.53	167	3.24

Tables 4.18-4.19 show the equilibrium properties of FeN compound in rocksalt and zinc-blende structures in the ferromagnetic state (for different values of *U*) and antiferromagnetic state (for *U*=0.2 Ry) within GGA + *U*. The AFM calculations have been performed in order to check for possible instability toward magnetic configuration. Among possible spin arrangements, Z. Zhao et al.[117] showed that the AFM-I aligned along the [001] direction is the most stable between different magnetic orderings For RS-FeN at 0 GPa.

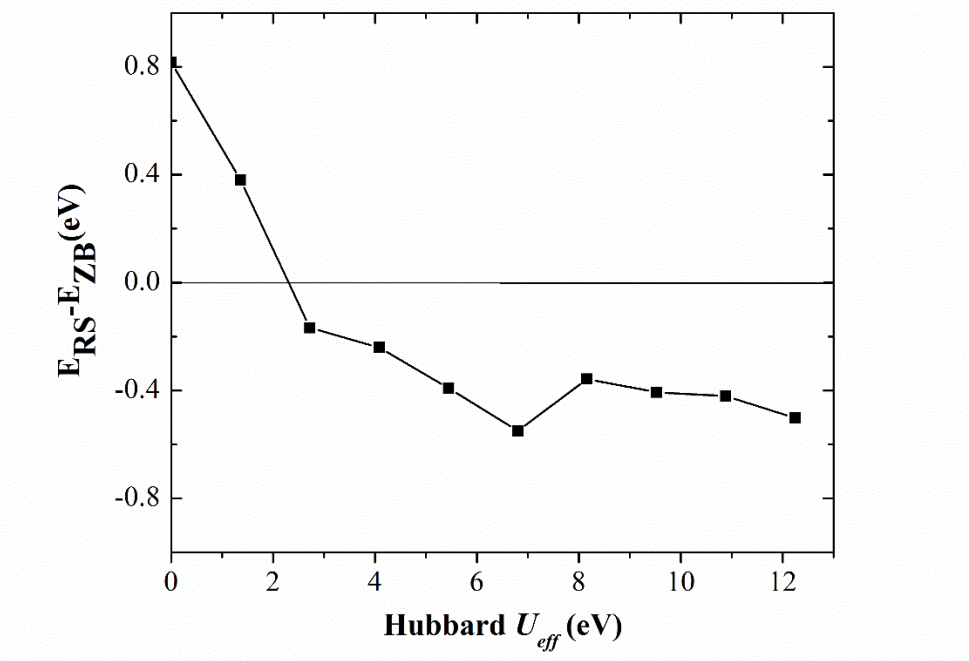

Figure 4.27 Spin polarization (SP) energy difference between RS and ZB structures as a function of Hubbard *U*.

we examined for this purpose the [001] alignment in which the spins are parallel within a layer but alternating direction between adjacent layers in the [001] direction. Fig. 4.27 shows the spin polarization energy difference between RS and ZB structures for different values for *U*. for $0 \leq U \leq 1.36eV$ the ZB is the ground state for FeN compound. By increasing *U* from 1.36 to 2.72 eV, the energy difference between RS and ZB structures dropped dramatically from 0.81 to -0.16 eV. Significantly, the RS structure ground state can be predicted for FeN when *U* values are more or equal to 2.72 eV. The transition of the ground state from ZB to RS within LDA+*U* is confirmed

by Z. Zhao et al. [117] for a values of *U* between 3 and 4 eV, although is further confirmed by HSE calculation in [117].

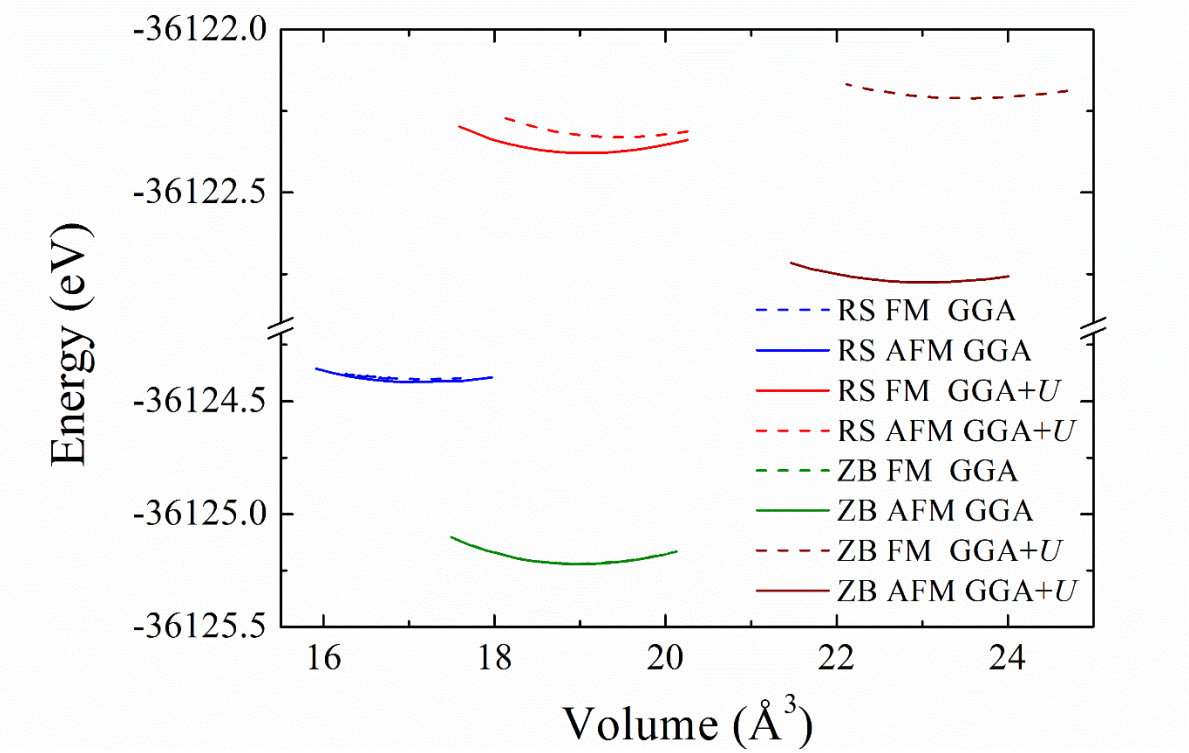

Figure 4.28 Ferromagnetic (FM) and (AFM) total energy versus volume for both RS-FeN and ZB-FeN phases using GGA and GGA+*U* (*U* = 2.72 eV).

In order to see the effects of electron correlations on magnetic stability of FeN, we have performed both FM and AFM-I ([001] alignment) calculations using GGA and GGA+*U* (*U* = 2.72 eV) with k-points of 6000 and 4000 in the full BZ for RS and ZB phases, respectively, which is sufficient to ensure the convergence of total energies to 10^{-4} Ry. From Fig. 4.28, GGA results show that the lower energy minimum occurs for both ZB and RS phases in AFM state. For both RS and ZB phases, the energy differences between AFM and FM states are too small to make clear conclusion on the nature of magnetic orderings. Using GGA + *U* calculations it is easy to see that RS and ZB phases are more stable in the FM and AFM states, respectively. We note also that GGA+*U* calculations gives more energy difference between FM and AFM states of both RS and ZB phases reach 0.048 and 0.564 eV for RS-FeN and ZB-FeN, respectively, which allows as to

make a clear conclusion on the nature of magnetic ordering of RS and ZB phases. From Fig. 4.29 we can see that the calculated cell parameters for both ZB and RS phases in the FM state increase with increasing *U*, a sudden increase of cell parameter for ZB phase to a value as high as 4.54 for *U* = 2.72 eV. The cell parameter of ZB phase corresponds to *U*= 1.36 eV shows the closest agreement with the experiment, while the cell parameter of RS phase is still far away from experimental lattice constant even at high Hubbard values.

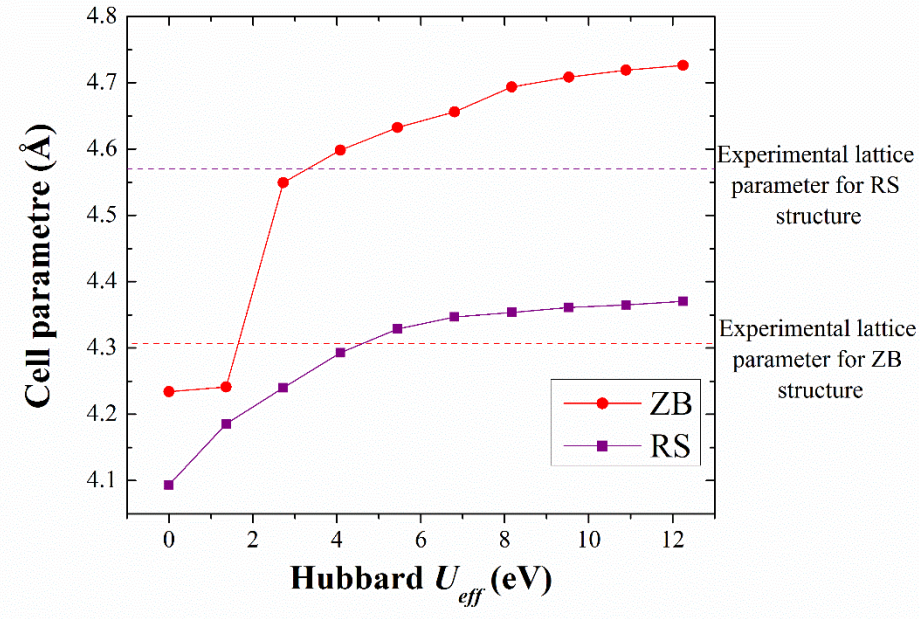

Figure 4.29 Cell parameter versus Hubbard *U* for both ZB and RS phases.

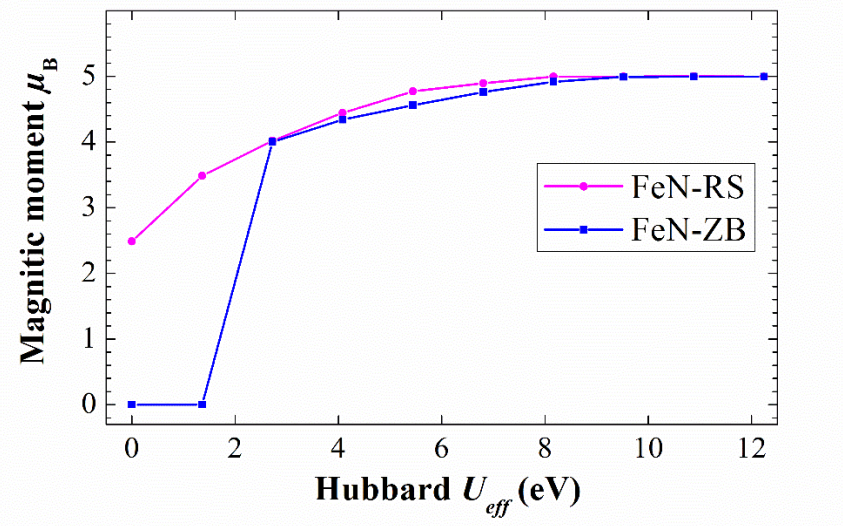

Figure 4.30 The calculated total magnetic moments for both RS and ZB phases as a function of Hubbard *U*.

Fig. 4.30 shows the calculated total magnetic moments for both RS and ZB phases as a function of Hubbard *U*. The on-site Coulomb Energy *U* further localizes the 3*d* orbital and keeps more spin densities in this orbital. The magnetic moments of FeN compound in both ZB- and RS-type structures increases with increasing Hubbard, consequently with increasing lattice parameter. Sudden increase in the magnetic moment of ZB phase from 0 to 3.36 μ_B/Fe at Hubbard U = 2.72 eV. For the value of U = 12.2 eV, the total magnetic moments of both ZB and RS raised by an amount of 4.99 and 2.5 μ_B/cell, respectively.

Density of states (DOS) plots are provided for both FeN-RS and FeN-ZB in the FM state for different values of Hubbard *U* (see Fig. 4.31). For $0 \leq U \leq 8.16$ eV, both RS and ZB phases are metallic with a primary contribution of Fe 3*d* electrons to the Fermi level. However, Applying *U* more than 9.52 eV, the band gaps appear at the spin-up and spin-dn channels for both RS and ZB phases.

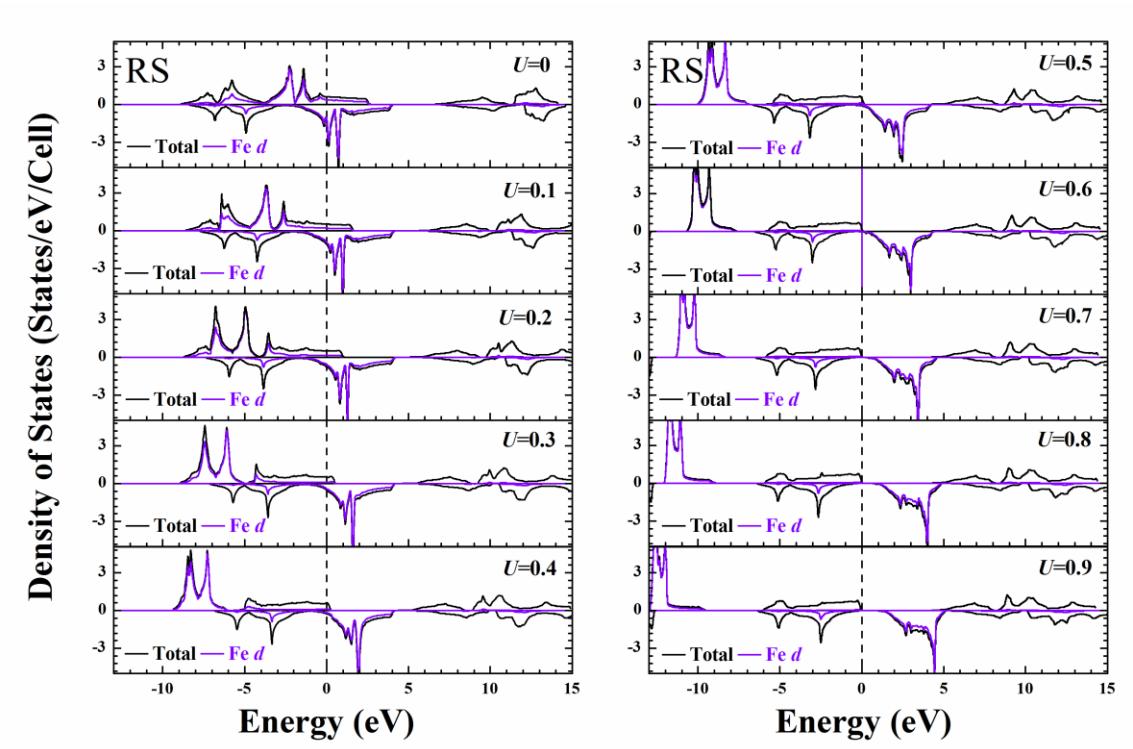

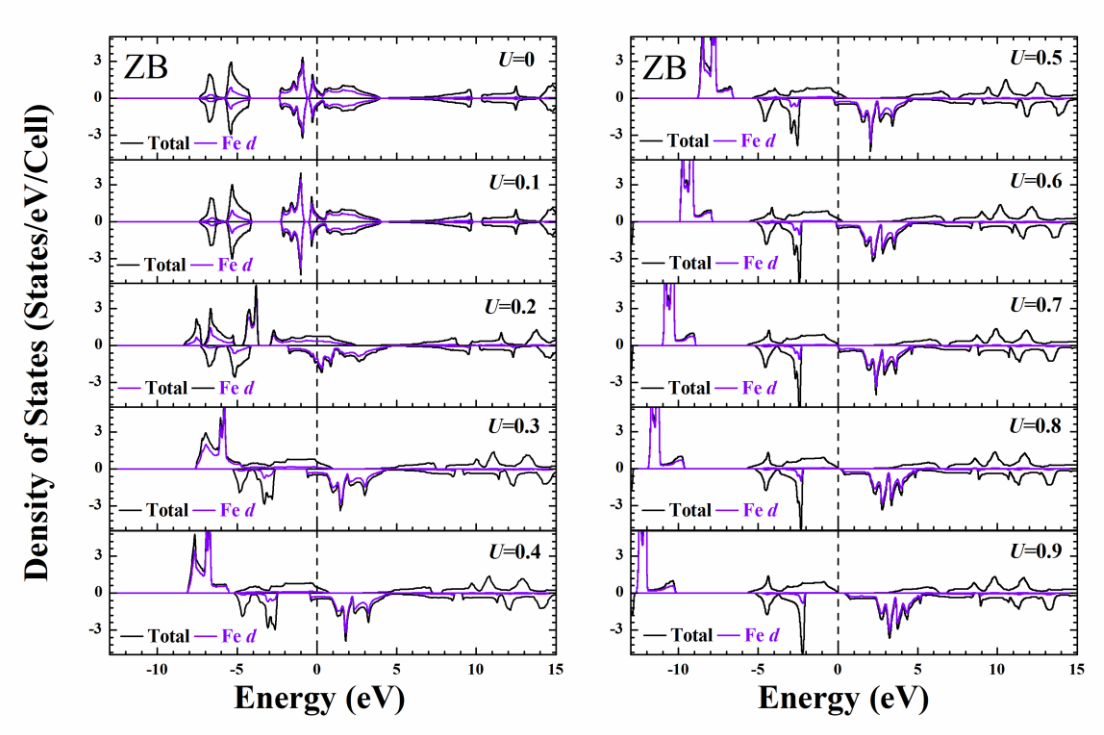

Figure 4.31 Density of states (DOS) plots for both FeN-RS and FeN-ZB phases in the FM state for different values of Hubbard *U*(Ry).

By increasing *U* from 9.52 to 12.24 eV, the RS band gaps in the spin-up and spin-dn channels increase from 3.20 to 3.26 eV, from 0.15 to 0.88 eV, respectively. However, the ZB band gap in the spin-up channel decreases from 1.27 to 1.22 eV, while the band gap in the spin-dn channel increases from 2.32 to 2.57 eV. Table 4.20 shows the values of the energy gap of FeN in RS and ZB structure from GGA+*U* calculations with different values for *U*.

Table 4.20 Values of the energy gap of FeN in RS and ZB structures from GGA+*U* calculations with different values for *U*.

	RS		ZB	
U (Ry)	$E_g\uparrow$ (eV)	$E_g\downarrow$ (eV)	$E_g\uparrow$ (eV)	$E_g\downarrow$ (eV)
0.7	3.20	0.15	1.27	2.32
0.8	3.23	0.56	1.23	2.41
0.9	3.26	0.88	1.22	2.57

4.3.6 Conclusions

First-principles density-functional theory calculations, using the full-potential linearized augmented plane wave FP-LAPW method within the local-spin-density approximation LSDA and generalized gradient approximation GGA, we have investigated the structural, magnetic and electronic properties of a number of binary 3*d* transition metal TMN (TM=Mn, Fe, Co) in SP and NSP states for RS-type structure. The stability of the non-magnetic state for MnN, FeN and CoN compounds are discussed in the framework of the well-known Stoner criterion. GGA + *U* calculations were performed to show the effects of electron correlations on the structural, magnetic and electronic properties for FeN compound in the RS and ZB-type structure. For $0 \leq U \leq 1.36eV$ the ZB is the ground state for FeN compound. By increasing *U* from 1.36 to 2.72 eV, the energy difference between RS and ZB structures dropped dramatically from 0.81 to -0.16 eV. Significantly, the RS structure ground state can be predicted for FeN when *U* values are more or equal to 2.72 eV. The stability toward magnetism in each phase using GGA calculations show that both RS-FeN and ZB-FeN phases stabilize in an antiferromagnetic state, while those of GGA+*U* calculations show that the RS-FeN and ZB-FeN phases are more stable in the ferromagnetic and antiferromagnetic states, respectively. GGA + *U* predicts a band gaps around the Fermi level for FeN compound in both RS and ZB phases for *U* values more or equal to 9.52 eV.

Chapter V

5. Overall summary and avenues for future work

5.1 Summary of conclusions

In this chapter a summary of the conclusions of the previous chapter (chapter 4) is presented. In this thesis we have studied the spin polarization and pressure effects on the structural, magnetic and electronic properties of the transition metal mono- and semi-borides TM-B and TM_2B (TM= Mn, Fe and Co) using both LSDA and GGA. Although, we have calculated the structural, magnetic and electronic properties of the transition metal mono-nitrides TM-N (TM=Mn, Fe, and Co) using LSDA and GGA. Finally, we have shown the effects of electron correlation on structural, magnetic and electronic properties for both RS-FeN and ZB-FeN phases.

For the transition metal mono- and semi-borides, the calculated lattice constants, bulk modulus, pressure derivative and magnetic moment were found to be in very good agreement with experimental and other theoretical results. The spin polarization has a significant impact on the cell volume and bulk modulus for both TM-B and TM_2B borides. The differences in volume between the magnetic and non-magnetic cases reach 4% for MnB and 4.7 % for Fe_2B. The calculated percent relative change of bulk modulus *B* between the NM and M states reaches 22% for MnB and 38 % for Fe_2B. The densities of states of MnB, FeB, Fe_2B and Co_2B ferromagnetic compounds are significantly modified under high pressures. The exchange splitting decreases with increasing pressure, at approximately, V/V_0 = 0.6 for MnB and FeB, V/V_0 = 0.7 for Fe_2B and Co_2B, the exchange disappears causes mirror in upper and lower half panels.

For the transition metal mono-nitrides, the calculated lattice constant, bulk modulus, pressure derivative and magnetic moment were found to be in very good agreement with other

theoretical results, and usually underestimated comparing to the experimental results. GGA + U calculations were performed to show the effects of electron correlations on the structural and electronic properties for FeN compound. For $0 \leq U \leq 1.36eV$ the ZB is the ground state for FeN compound. By increasing U from 1.36 to 2.72 eV, the energy difference between RS and ZB structures dropped dramatically from 0.81 to -0.16 eV. Significantly, the RS structure ground state can be predicted for FeN when U values are more than 2.72 eV. The stability toward magnetism in each phase using GGA calculations show that both RS-FeN and ZB-FeN phases stabilize in an AFM state, while those of GGA+U calculations show that the RS-FeN and ZB-FeN phases are more stable in the FM and AFM states, respectively. Applying U more than 9.52 eV, the band gaps appear at the spin-up and spin-dn channels for both RS and ZB phases. The stability of the non-magnetic phase was studied within the Stoner model, the results are consistent with the experimental findings for all the compounds studied except for CoN and Mn_2B compounds.

5.2 Future work

We have successfully calculated the structural, magnetic, and electronic properties for TM-B and TM_2B borides with spin polarization, without spin polarization and under pressure. Very much of the interesting physical properties of the transition metal borides and nitrides under pressure are still unexplored. Also, this thesis shows the effects of electron correlation on structural, magnetic and electronic properties for iron mono-nitrides. More work is needed for other transition metal nitrides such as cobalt nitride and manganese nitride. Recent research for spintronic materials has focused on thin films and nanosize particles grown on semiconductor substrates and on high concentration doping in suitable semiconductors in which the transition metal nitride clusters may form by precipitation. One common distinct feature of these systems is that the transition metal compound volume can be very different from its bulk equilibrium value. This is the result of the large strain imposed by the substrate or the host [111]. Therefore, the studies of the volume

dependence of the structure, the electronic and the magnetic properties of transition metal nitrides is important for understanding the properties of these compounds in film or small clusters form.

BIBLIOGRAPHY

[1] E. Lifshin, X-ray Characterization of Materials, Wiley, 2008.
[2] B.H. Stuart, Infrared Spectroscopy: Fundamentals and Applications, Wiley, 2004.
[3] T. Chatterji, Neutron Scattering from Magnetic Materials, Elsevier Science, 2005.
[4] P. Hohenberg and W. Kohn, Physical Review, 136 (1964) B864.
[5] D.J. Singh and L. Nordstrom, Planewaves, Pseudopotentials, and the LAPW Method, Springer, 2005.
[6] J.P. Perdew and Y. Wang, Physical Review B, 45 (1992) 13244.
[7] J.P. Perdew, K. Burke and M. Ernzerhof, Physical Review Letters, 77 (1996) 3865.
[8] J.P. Perdew, K. Burke and Y. Wang, Physical Review B, 54 (1996) 16533.
[9] A. Friedrich, B. Winkler, E.A. Juarez-Arellano and L. Bayarjargal, Materials, 4 (2011) 1648.
[10] P.H. Lee, Z.R. Xiao, K.L. Chen, Y. Chen, S.W. Kao and T.S. Chin, Physica B: Condensed Matter, 404 (2009) 1989.
[11] P. Mohn and D.G. Pettifor, Journal of Physics C: Solid State Physics, 21 (1988) 2829.
[12] S.T. Oyama, The Chemistry of Transition Metal Carbides and Nitrides, Springer, 1996.
[13] O. Ozdemir, M. Usta, C. Bindal and A.H. Ucisik, Vacuum, 80 (2006) 1391.
[14] L.E. Toth, Transition Metal Carbides and Nitrides, Acadimic Press, New York, 1971.
[15] J. Yang, J.H.Wang, H.G.Fu and D.Z.Ren, FoundryTechnol., 27 (2006) 1079.
[16] C.B. Li, M.K. Li, F.Q. Liu and X.J. Fan, Modern Physics Letters B, 18 (2004) 281.
[17] C. Petit and M.P. Pileni, Journal of Magnetism and Magnetic Materials, 166 (1997) 82.
[18] H. Zhu, C. Ni, F. Zhang, Y. Du and J.Q. Xiao, Journal of Applied Physics, 97 (2005).
[19] C. Cadeville, PhD thesis, Strasbourg, 1965.
[20] M. Ribeiro, M. Marques, L.M.R. Scolfaro, L.K. Teles and L.G. Ferreira, AIP Conference Proceedings, 893 (2007) 1227.
[21] L.M. Corliss, N. Elliott and J.M. Hastings, Physical Review, 117 (1960) 929.
[22] J.P. Dismukes, W.M. Yim and V.S. Ban, Journal of Crystal Growth, 13–14 (1972) 365.
[23] G.F. Hardy and J.K. Hulm, Physical Review, 93 (1954) 1004.
[24] N. Heiman and N.S. Kazama, Journal of Applied Physics, 52 (1981) 3562.
[25] M. Mekata, H. Yoshimura and H. Takaki, Journal of the Physical Society of Japan, 33 (1972) 62.
[26] A. Neckel, P. Rastl, R. Eibler, P. Weinberger and K. Schwarz, Journal of Physics C: Solid State Physics, 9 (1975) 579.
[27] B. Eck, R. Dronskowski, M. Takahashi and S. Kikkawa, Journal of Materials Chemistry, 9 (1999) 1527.
[28] K. Suzuki, T. Kaneko, H. Yoshida, Y. Obi, H. Fujimori and H. Morita, Journal of Alloys and Compounds, 306 (2000) 66.
[29] A. Leineweber, R. Niewa, H. Jacobs and W. Kockelmann, Journal of Materials Chemistry, 10 (2000) 2827.
[30] H. Nakagawa, S. Nasu, H. Fujii, M. Takahashi and F. Kanamaru, Hyperfine Interact, 69 (1991).
[31] T. Hinomura and S. Nasu, Hyperfine Interact., 111 (1998) 221.
[32] K. Suzuki, H. Morita, T. Kaneko, H. Yoshida and H. Fujimori, Journal of Alloys and Compounds, 201 (1993) 11.
[33] L. Rissanen, M. Neubauer, K.P. Lieb and P. Schaaf, Journal of Alloys and Compounds, 274 (1998) 74.

[34] O. Schmitz-Dumont and N. Kron, Angewandte Chemie, 67 (1955) 231.
[35] T.B. Joyner and F.H. Verhoek, Journal of the American Chemical Society, 83 (1961) 1069.
[36] P. Blaha, K. Schwarz, G.K.H. Madsen, D. Kvasnicka and J. Luitz, WIEN2k, An Augmented Plane Wave Plus Local Orbitals Program for Calculating Crystal Properties, Vienna University of Technology, Austria, 2012.
[37] D.C. Young, Computational Chemistry, John Wiley & Sons, Inc., 2002.
[38] R.G. Parr and R.G.P.W. Yang, Density-Functional Theory of Atoms and Molecules, Oxford University Press, USA, 1989.
[39] R.M. Dreizler and E.K.U. Gross, Density Functional Theory, Springer-Verlag Berlin Heidelberg, 1990.
[40] W. Kohn and L.J. Sham, Physical Review, 140 (1965) A1133.
[41] U. Von Barth and L. Hedin, Journal of Physics C: Solid State Physics, 5 (1972) 1629.
[42] D. Wu, First-principles Study on Hard/soft Samarium-cobalt/cobalt-iron Nanocomposite Magnetic Materials, University of Texas at Arlington 2008.
[43] J.C. Slater, Physical Review, 51 (1937) 846.
[44] D.J. Singh and L. Nordstrom, Planewaves, Pseudopotentials, and the LAPW Method, Springer, 2006.
[45] O.K. Andersen, Physical Review B, 12 (1975) 3060.
[46] D.D. Koelling and G.O. Arbman, Journal of Physics F: Metal Physics, 5 (1975) 2041.
[47] E. Sjöstedt, Ph.D. thesis, Uppsala University, 2002.
[48] E. Sjöstedt, L. Nordström and D.J. Singh, Solid State Communications, 114 (2000) 15.
[49] G.K.H. Madsen, P. Blaha, K. Schwarz, E. Sjöstedt and L. Nordström, Physical Review B, 64 (2001) 195134.
[50] W.D. Callister, Materials Science and Engineering: An Introduction, Wiley, 2002.
[51] Magnetism, DISCovering Science. Gale Research, 1996.
[52] N.A. Spaldin, Magnetic Materials: Fundamentals and Applications, Cambridge University Press, 2010.
[53] L. Rednic, electronic structure and magnetic properties of metallic systems based on rare earths and *d* transition elemets PhD thesis, Babeș-Bolyai University, 2010.
[54] T. Moriya, Spin Fluctuations in Itinerant Electron Magnetism, Springer Berlin Heidelberg, 2012.
[55] P. Langevin, J. Phys. Theor. Appl., 4 (1905) 678.
[56] P. Weiss, J. Phys.Radium, 6 (1907).
[57] W. Heisenberg, Z. Phys., 49 (1928) 619.
[58] P.A.M. Dirac, Quantum Mechanics of Many-Electron Systems, 1929.
[59] J.H. Van Vlek, The Theory of Electric and Magnetic Susceptibilities, BiblioBazaar, 2011.
[60] M.A. Ruderman and C. Kittel, Physical Review, 96 (1954) 99.
[61] T. Kasuya, Progress of Theoretical Physics, 16 (1956) 58.
[62] K. Yosida, Physical Review, 106 (1957) 893.
[63] H.A. Kramers, Physica, 1 (1934) 825.
[64] F. Bloch, Z. Phys., 57 (1929).
[65] E. Wigner, Physical Review, 46 (1934) 1002.
[66] E.C. Stoner, Collective Electron Ferromagnetism, 1938.
[67] v. der, First-principles study of the exchange interactions and Curie temperature in Heusler alloys, PhD thesis, Mathematisch-Naturwissenschaftlich-Technischen Fakult¨at, der Martin-Luther-Universitat, 2006.
[68] T. Bjurstrom and H. Arnfeld, Z. Phys. Chem., B 4 (1929).
[69] T. Bjurstrom, Ark. Chem. Min. Geol. , A 11 (1933) 1.

[70] R. Kiessling, Acta Chem. Scand., 4 (1950) 209.
[71] R. Kiessling, Acta Chem. Scand., 4 (1950) 146.
[72] B. Aronson, Ark. Kemi 16 (1960) 379.
[73] L. Guangwei and W. Dingsheng, Journal of Physics: Condensed Matter, 1 (1989) 1799.
[74] G. Hagg and R. Kiesslieng, J. Inst. Metals, 81 (1952/53) 57.
[75] L.Y. Markovskii and E.T. Bezruk, Izv. Akad. Nauk SSSR, Set. Neorg. Mater., 3 (1967) 2165.
[76] K.I. Portnoi, V.M. Romashov, V.M. Chubarov, M.K. Levinskaya and S.E. Salibekov, Poroshkovaya Met., 2 (1967) 15.
[77] J.D. Schobel and H.B. Stadelmeier, Z. Metallk., 57 (1966) 323.
[78] K.I. Portnoi, M.K. Levinskaya and V.M. Romashov, Poroshkovaya Met., 8 (1969) 66
[79] L.Y. Markovskii and E.T. Bezruk, Zh. Prikl. Khim., 35 (1962) 491.
[80] M.-C. Cadeville and E. Daniel, J. Phys. (Paris), 27 (1966) 449.
[81] G. Fischer and A.J.P. Meyer, Compt. Rend. B, 265 (1967) 521.
[82] I.R. Shein, N.I. Medvedeva and A.L. Ivanovskii, Physica B: Condensed Matter, 371 (2006) 126.
[83] C.T. Zhou, J.D. Xing, B. Xiao, J. Feng, X.J. Xie and Y.H. Chen, Computational Materials Science, 44 (2009) 1056.
[84] W. Kohn, Reviews of Modern Physics, 71 (1999) 1253.
[85] E.M. Ann, A.S. Peter, P.D. Michael, R.M. Thomas and L. Kevin, Modelling and Simulation in Materials Science and Engineering, 13 (2005) R1.
[86] F.D. Murnaghan, Proc. Natl. Acad. Sci. USA, 30 (1944) 5390.
[87] B. Wang, X. Li, Y.X. Wang and Y.F. Tu, The Journal of Physical Chemistry C, 115 (2011) 21429.
[88] P.K. Liao and K.E. Spear, Bulletin of Alloy Phase Diagrams, 7 (1986) 543.
[89] S.B. Hendricks and P.R. Kosting, Z.Kristallogr. Kristallgeom. Kristallphys. Kristall-chem., 74 (1930) 511.
[90] R.M. Bozorth, Ferromagnetism, Van Nostrand, NewYork 1951.
[91] S. Kervan, J Supercond Nov Magn, 24 (2011) 815.
[92] D.M. Roy and D.G. Pettifor, Journal of Physics F: Metal Physics, 7 (1977) L183.
[93] J.F. Janak, Physical Review B, 16 (1977) 255.
[94] S. Chikazumi, Physics of Magnetism, Wiley, New York, 1964.
[95] T. Egami, B.V. Fine, D.J. Singh, D. Parshall, C. de la Cruz and P. Dai, Physica C: Superconductivity, 470 Supplement 1 (2010) S294.
[96] D. Armstrong, P. Perkins and E. Cetina V, Theoretica Chimica Acta, 64 (1983) 41.
[97] D.J. Joyner, O. Johnson and D.M. Hercules, Journal of the American Chemical Society, 102 (1980) 1910.
[98] A. Houari, S.F. Matar, M.A. Belkhir and M. Nakhl, Physical Review B, 75 (2007) 064420.
[99] R.W.G. Wyckoff, Crystal Structures, Wiley, New York, 1963.
[100] P. Mohn, Journal of Physics C: Solid State Physics, 21 (1988) 2841.
[101] M.C. Cadeville and A.J.P. Meyer, C. R. Acad. Sci. (Paris), 255 (1962) 3391.
[102] K.A. Murphy and N. Hershkowitz, Physical Review B, 7 (1973) 23.
[103] B. Xiao, J. Feng, C.T. Zhou, J.D. Xing, X.J. Xie, Y.H. Cheng and R. Zhou, Physica B: Condensed Matter, 405 (2010) 1274.
[104] E.E. Havinga, H. Damsma and P. Hokkeling, J. Less-Common Metals, 27 (1972) 169.
[105] K. Suzuki, Y. Yamaguchi, T. Kaneko, H. Yoshida, Y. Obi, H. Fujimori and H. Morita, Journal of the Physical Society of Japan, 70 (2001) 1084.

[106] H. Shimizu, M. Shirai and N. Suzuki, Journal of the Physical Society of Japan, 67 (1998) 922.
[107] A. Filippetti and W.E. Pickett, Physical Review B, 59 (1999) 8397.
[108] Y. Kong, Journal of Physics: Condensed Matter, 12 (2000) 4161.
[109] P. Lukashev and W.R.L. Lambrecht, Physical Review B, 70 (2004) 245205.
[110] W.R.L. Lambrecht, M.S. Miao and P. Lukashev, Journal of Applied Physics, 97 (2005) 10D306.
[111] M.S. Miao and W.R.L. Lambrecht, Physical Review B, 71 (2005) 214405.
[112] H.-B. Wang and D.-S. Xue, Chinese Physics Letters, 21 (2004) 1612.
[113] K. Suzuki, T. Kaneko, H. Yoshida, H. Morita and H. Fujimori, Journal of Alloys and Compounds, 224 (1995) 232.
[114] C.-B. Li, M.-K. Li, D. Yin, F.-Q. Liu and X.-J. Fan, Chinese Physics, 14 (2005) 2287.
[115] A. Houari, Ab Initio Approach On Magneto-Volume Versus Chemical Effects In Insertion Alloys: Transition Metal Nitrides, PhD thesis, University of Bejaia, Algeria, 2008.
[116] J. Häglund, G. Grimvall, T. Jarlborg and A.F. Guillermet, Physical Review B, 43 (1991) 14400.
[117] Z. Zhao, K. Bao, D. Duan, F. Tian, B. Liu and T. Cui, RSC Advances, 5 (2015) 31270.